Stony Brook University

Biomarker Sensing using Nanostructured Metal Oxide Sensors

A Dissertation Presented

by

Krithika Kalyanasundaram

to

The Graduate School

in Partial fulfillment of the

Requirements

for the Degree of

Doctor of Philosophy

in

Materials Science and Engineering

Stony Brook University

December 2007

Stony Brook University

The Graduate School

Krithika Kalyanasundaram

We, the dissertation committee for the above candidate for the

Doctor of Philosophy degree, hereby recommend

acceptance of this dissertation.

Prof. Pelagia I. Gouma - Dissertation Advisor

Associate Professor, Materials Science and Engineering

Prof. Devinder Mahajan

Professor, Materials Science and Engineering

Prof. Clive R. Clayton

Professor, Materials Science and Engineering

Dr. David J. Kubinski

Ford Research Laboratory

This dissertation is accepted by the Graduate School

Lawrence Martin
Dean of the Graduate School

Abstract of the Dissertation

Biomarker Sensing using Nanostructured Metal Oxide Sensors

by

Krithika Kalyanasundaram

Doctor of Philosophy

in

Materials Science and Engineering

Stony Brook University

2007

Resistive Chemical sensors are those gas sensitive materials, typically semiconducting metal oxides, that change their electrical properties in response to a change in the ambient. The key features of a chemosensor are sensitivity, selectivity, response time and sensor stability. The hypothesis of this work is that, since metal oxides are polymorphic compounds, the crystal structure of the specific polymorph determines the relative gas selectivity of the material; also that the morphology of the sensing element determines the gas sensitivity limit. This work focuses on the synthesis of nanostructured metal oxides for chemosensors used in selective 'biomarker' detection. Biomarkers are chemical compounds, products of human metabolism which act as specific disease markers. The biomarkers studied in this work include NO, isoprene, NH_3, ethanol and acetone which can all be found in exhaled human breath and which allow the non-invasive detection of a range of diseases.

Sensors based on three different metal oxides-MoO_3, WO_3, and TiO_2 were fabricated using sol-gel, electrospinning and spray pyrolysis techniques and tested both as single elements and in an array configuration (electronic nose). The effects of the processing method used, grain size and shape and crystal phase of the material produced, and temperature effects of postsynthesis processing and sensing have been evaluated. Structural characterization has been carried out using X-Ray Diffraction, Scanning and High Resolution Transmission Electron Microscopy, while spectroscopic measurements using XPS, Raman and In-situ FTIR provide valuable information about the surface-analyte interactions.

This work has shown that the use of monoclinic polymorph of WO_3 yields a selective response to NO, while the other phase of the same oxide give a non-selective chemical response. The orthorhombic phase of MoO_3 exhibits specificity to NH_3. An explanation for the variable sensing properties is given based on the gas interactions with the given polymorph involving adsorption/reaction processes. Another major finding of this work is that there was orders of magnitude increase in gas sensitivity when high aspect ratio nanowires as opposed to nanoparticles of the same diameter were used.

Dedicated to

My Family

Table of Contents

List of Figures……x

List of Tables……...xvi

List of Symbols……...xvii

List of Abbreviations……..xix

Preface……...xx

Acknowledgements……xxii

Vita……..xxv

Publications……...xxvi

1. Introduction……..……1

1.1 Sensor Definition and Classification……...2

1.2 Metal Oxides- Resistive Gas Sensing……..4

1.2.1 Principles of resistive Gas Sensing…….5

1.2.2 Surface States in Ionic Crystals like SnO_2.....6

1.2.3 Concept of Fermi Level Pinning and Unpinning……..11

1.2.4 n-p and p-n type transitions in semiconducting gas sensors…….15

1.3 Importance of 'nano' structure for gas sensing……..16

1.3.1 Fabrication of nanostructured metal oxides……..18

1.3.1.1 Conventional methods……...18

1.3.1.1.1 Sol-gel Method……19

1.3.1.1.2 Spray Pyrolysis……...20

1.3.1.2 Unconventional Methods……...21

1.4 Sensor Attributes……22

1.5 Tungsten trioxide……...24

1.5.1 Structure of Tungsten trioxide……..24

1.5.2 Orthorhombic and Monoclinic Tungsten Trioxide……...26

1.5.3 Hexagonal tungsten trioxide…….27

1.5.4 Nitrogen Oxides……29

1.5.4.1 Nitric Oxide in human breath……29

1.6 Molybdenum Oxide……...30

1.6.1 Ammonia……...31

1.7 Titanium Dioxide……...31

1.8 Statement of the Problem……...32

References……..35

2. **Experimental**……..46

2.1 Materials Synthesis……46

2.1.1 Sol-gel Method……..46

2.1.2 Spray Pyrolyis……...47

2.1.3 Electrospinning…….47

2.2 Sensor Processing……..49

2.3 Materials Characterization…….50

2.3.1 Differential Scanning Calorimetry……50

2.3.2 X-ray Diffraction……..50

2.3.2 Transmission Electron Microscopy……..51

2.3.3.1 High resolution Transmission Electron Microscopy…….51

2.3.4 Raman Spectroscopy…….51

2.3.5 Photoluminescence Measurements……...52

2.3.7 X-ray Photoelectron Spectroscopy……...52

2.4 Sensor Characterization…….52

References……..55

3. WO_3 Polymorphic Sensors……56

3.1 Structural Characterization……56

3.1.1 Differential Scanning Calorimetry……56

3.1.2 X-ray Diffraction……..57

3.1.3 Transmission Electron Microscopy……..59

3.1.4 High Resolution Transmission Electron Microscopy……...62

3.1.5 Raman Spectroscopy…….65

3.1.6 Photo Luminescence measurements…….68

3.1.7 X-Ray Photoelectron Spectroscopy……..69

3.2 Sensor Characterization…….73

3.2.1 Monoclinic and Orthorhombic WO_3 sensors……73

3.2.2 Ultra-low Concentration Sensing……..76

3.2.2.1 Monoclinic polymorph……...76

3.2.2.2 Orthorhombic Polymorph……..79

References……..82

4. MoO_3 nanowire Sensors……84

4.1 Materials Characterization……84

4.1.1. Differential Scanning Calorimetry……...84

4.1.2 Electron Microscopy……85

4.2 Sensor Characterization……91

References……..97

5. Sensor Arrays……98

5.1 Sensors……...99

5.2 Gases……..99

5.3 Data Analysis……...101

5.4 Sensor Array Responses……..101

5.4.1 Reducing Gases……...101

5.4.2 Oxidizing Gases……..104

References……107

6. Discussion……109

7. Conclusions and Future Work……128

8. Appendix……...136

List of Figures

Figure 1.1: Concept of a Sensor……..2

Figure 1.2: 'Flat Band' condition-No charge exchange between the surface states and the bulk……..7

Figure 1.3: Formation of a depletion layer in an n-type semiconductor…….9

Figure 1.4: Formation of an accumulation layer between the electropositive surface species and the negatively charged semiconductor……...10

Figure 1.5: Formation of an inversion layer in an n-type semiconductor…….11

Figure 1.6: Band bending after chemisorption of charged species (here ionosorption of oxygen on E_{SS} levels χ denotes the work function, μ the electrochemical potential, and φ_s is the electron affinity, and φ_o or qV_s the surface barrier)..……...13

Figure 1.7: Schematic illustrating the commonly used techniques for nanostructured thin film deposition……...18

Figure 1.8: Schematic of the sol-gel processing technique……..20

Figure 1.9: Idealized cubic perovskite ABO_3 like structure showing the corner sharing oxygen octahedra……...25

Figure 1.10: Structure of WO_3 based on the ReO_3 structure, showing the distorted WO_6 octahedra……....27

Figure 2.1: Schematic of the sensing and heating electrodes……...49

Figure 2.2: (a) Schematic of EOS 835 and the sensing chamber; (b) Schematic of the sensing substrate on the TO8 substrate……..53

Figure 2.3: Schematic of the gas sensing setup……54

Figure 3.1: DSC data for sol-gel WO_3……..56

Figure 3.2: X-ray diffraction profile of WO_3 sol-gel precursor annealed at 515°C…….58

Figure 3.3: X-ray diffraction profile of WO_3 sol-gel precursor heat treated at 400°C….58

Figure 3.4: General TEM view of the 515°C annealed sample……59

Figure 3.5: SAED pattern corresponding to WO_3 sample heat treated at 515°C…….60

Figure 3.6: General TEM view of the 400°C annealed sample……61

Figure 3.7: SAED pattern corresponding to the sample heat treated at 400°C…….61

Figure 3.8: Crystallographic shear planes in WO_3……...63

Figure 3.9: High resolution transmission electron microscopy image of a single grain in the sample heat treated at 515°C……64

Figure 3.10: IFFT of region 1 outlined in figure 3.8……64

Figure 3.11: IFFT of region 2 outlined in figure 3.8……65

Figure 3.12: Raman spectra of the WO_3 films annealed at 400 and 515°C……..66

Figure 3.13: PL spectra of the WO_3 polymorphs……..68

Figure 3.14: W4f core level spectra of the orthorhombic (B1) and monoclinic (A1) polymorph……..69

Figure 3.15: W4f core level resolved spectra of the orthorhombic (B1) and monoclinic (A1) polymorph…….70

Figure 3.16: Valence band and O 2s core level spectra of the monoclinic (A1) and the orthorhombic (B1) sample…….72

Figure 3.17: Response of the monoclinic sensor to (a) 10-200 ppm of NO_2 (b) 5-10 ppm acetone; (c) 5-10 ppm isoprene; (d) 50 ppm ethanol…….73

Figure 3.18: Response of the orthorhombic sensor to (a) 10-200 ppm of NO_2 (b) 5-10 ppm acetone; (c) 5-10 ppm isoprene; (d) 50 ppm ethanol…….74

Figure 3.19: Comparison of sensitivities of the monoclinic polymorph at 400°C……...75

Figure 3.20: Comparison of sensitivities of the monoclinic polymorph at 500°C……...76

Figure 3.21: Sensing response of monoclinic polymorph at 400°C to NO……..77

Figure 3.22: Sensing response of monoclinic polymorph at 400°C to NO_2…….77

Figure 3.23: Sensitivity variation of the monoclinic sensor with NO concentration at 400°C…….78

Figure 3.24: Sensitivity variation of the monoclinic sensor with NO_2 concentration at 400°C…….78

Figure 3.25: Sensing response of orthorhombic polymorph at 200°C to NO……..79

Figure 3.26: Sensing response of orthorhombic polymorph at 200°C to NO_2…….80

Figure 3.27: Comparison of sensitivities of the monoclinic polymorph at 400°C……...80

Figure 3.28: Comparison of sensitivities of the orthorhombic polymorph at 200°C…….81

Figure 4.1: DSC data for the MoO_3 sol-gel precursor…….84

Figure 4.2: Low magnification TEM image of the PVP-MoO_3 mat before calcination……..86

Figure 4.3: TEM micrograph of (a) the as spun PVP mat; and (b) the PVP-MoO_3 electrospun composite mat before calcination showing the aligned encapsulation of the sol-gel along the polymer fiber walls (indicated by arrows)(b) TEM of calcined composite mats……...86

Figure 4.4: HRTEM image of a MoO_3 nanowire on a Si_3N_4 grid; (inset) higher magnification image of the same nanowire……...88

Figure 4.5: High resolution transmission electron microscopy of MoO_3 nanowire showing the growth direction of the nanowires…….89

Figure 4.6: SEM images of the nanowire mat on an Al_2O_3 substrate after sensing; (inset) High magnification image of a single MoO_3 nanowire…….92

Figure 4.7: SEM images of the MoO_3 sol-gel on an Al_2O_3 substrate after sensing……92

Figure 4.8: Sensitivity of nanocrystalline MoO_3 sol-gel films to various concentrations of NH_3……94

Figure 4.9: Sensitivity of nanocrystalline MoO_3 nanowires to different concentrations of NH_3; (inset) Reproducibility of MoO_3 to 100ppm NH_3……95

Figure 4.10: Comparison of Sensitivity of MoO_3 nanowires vs sol-gel sensors……95

Figure 5.1: Sensing response of the five sensor array to 10 ppm acetone……..102

Figure 5.2: Response of the five sensor array to 10 ppm isoprene…….102

Figure 5.3: Response of the five sensor response 10 ppm methanol……..103

Figure 5.4: Response of the five sensor array to 10 ppm ethanol……...103

Figure 5.5: Response of the five sensor array to CO……..104

Figure 5.6: Response of the sensor array to 10 ppm NO……105

Figure 5.7: Response of the sensor array to 10 ppm NO_2……...105

Figure 6.1: Comparison of sensitivity of the orthorhombic polymorph at 515°C to NO and NO_2……112

Figure 6.2: Comparison of sensitivity of the monoclinic polymorph at 400°C to NO and NO_2……..113

Figure 6.3: Comparison of sensitivity of the orthorhombic and monoclinic polymorphs to NO and NO_2…….113

Figure 6.4: Role of CS planes in hydrocarbon oxidation; (a) an oxide that is unable to form CS planes has to oxidize the hydrocarbon by creating a new vacancy, while (b) an oxide that can form or has existing CS planes can oxidize the hydrocarbon at a much lower energy…….116

Figure 7.1: Flow-chart of the prototype schematic…….132

Figure 7.2: The electronic circuitry of the device. The sensor and interface circuitry and display are depicted. The microcontroller (μC) contains the Analog-to-Digital Converter (ADC), memory (SRAM), and an Arithmetic Logic Unit (ALU). V_{test}: Voltage proportional to the resistance of the sensor……..132

Figure A1.1: WO_6 octahedra in WO_3…….137

Figure A1.2: Arrangement of WO_6 octahedra in hexagonal WO_3…….138

Figure A1.3: XRD spectra of the h-WO_3 samples heat treated at (a) 400°C and (b) 515°C……...141

Figure A1.4: Low magnification SEM image of the sol-gel film heat treated at 400°C; (inset a) a single nanowire growing from a grain cluster; (inset b) a grain cluster on the film……...142

Figure A1.5: SEM image of heat treated films, (a) and (b) nanowires (c) nanoparticles and (d) nanosheet bundles……143

Figure A1.6: TEM images of (a) Nanowires (b) Nanoparticles and (c) Nanosheets……...144

Figure A1.7: (a) Perspective view illustrating $H_{0.24}WO_3$ with the H atoms in the interstitial spaces, precursor to, (b) h-WO_3……..147

List of Tables

Table 1.1: Classification of Sensor Materials…….3

Table 1.2: Bulk and surface parameters of influence for SnO_2 single crystals. n_b is the concentration of free charge carriers (electrons), μ_b is their Hall mobility, λ_D is the Debye length, and λ is the mean free path of free charge carriers……17

Table 1.3: Crystal structures, the unit cell parameters, the transformation temperatures of WO_3……....26

Table 2.1: Concentrations of gases used for sensing…….....54

Table 3.1: SAED pattern indexation corresponding to that shown in figure 3.5……..60

Table 3.2: Raman vibration modes found in the WO_3 samples annealed at 400°C and 515°C…….66

Table 4.1: Calculated sensitivity data for the nanowire and sol-gel sensors……96

Table 6.1: Existing literature on the gas sensing properties of WO_3 towards NO_x (A '*' next to an interfering gas means a positive interference while its absence indicates that there was no interference. 'NA' implies that no cross sensitivity studies have been made)……109

List of Symbols

E_C-Conduction band edge

E_V-Valence band edge

E_F or μ -Fermi energy level

E_A-Acceptor (surface state) energy level

E_D-Donor (surface state) energy level

E_{CO}-Conduction band edge before charge transfer from the surface states

E_{VO}-Valence band edge before charge transfer from the surface states

E_{FO}-Fermi energy level before charge transfer from the surface states

E_{CS}-Conduction band edge (band bending) after charge transfer from the surface states

E_{VS}-Valence band edge (band bending) after charge transfer from the surface states

E_{FS}-Fermi energy level after charge transfer from the surface states

χ- Work function (Energy required to move an electron from the inside of a semiconductor to a point just outside the surface)

φ_s- Electron affinity

φ_o- Surface barrier

ς- Chemical potential

φ- Electrostatic potential of an electron

σ- Semiconductor conductivity

n/p- Electron/Hole Concentration

n_s- Surface charge carrier concentration

μ_n/μ_p- Electron/Hole Mobility

q- Charge associated with holes and electrons

λ_D- Debye Length (Length of the space charge region or depletion layer in an n-type semiconductor)

k_B- Boltzmann constant (8.617E-5 eV/K)

λ- Mean free path of electrons

N_{NW}- Number of Nanowires

N_{NP}- Number of Nanoparticles

V- Total volume of material depostied

V_{NW}- Volume of Nanowires

V_{NP}- Volume of Nanoparticles

SA_{NW}- Surface Area of Nanowires

SA_{NP}- Surface Area of Nanoparticles

l- Length of the nanowires

r- Radius of the nanowire/nanoparticle

List of Abbreviations

DSC- Differential Scanning Calorimetry

TGA- Thermo Gravimetric Analysis

XRD- X-ray Diffraction

TEM- Transmission Electron Microscopy

SAD/SAED- Selected Area Diffraction/Selected Area Electron Diffraction

HRTEM- High Resolution Transmission Electron Microscopy

FFT- Fast Fourier Transform

IFFT- Inverse Fast Fourier Transform

XPS- X-ray Photoelectron Spectroscopy

BE- Binding Energy

FTIR- Fourier Transform Infrared Spectroscopy

PL- Photo Luminescence

JCPDS- Joint Committee on Powder Diffraction Standards

CS- Crystallographic Shear

VOC- Volatile Organic Compound

Preface

The work presented in this dissertation focuses on the development of resistive chemical sensors based on nanostructured metal oxides, for detecting specific biomarkers (metabolites in human breath), that can be used for non-invasive monitoring of diseases.

Chapter 1 gives a general overview of chemical sensors and in particular metal oxide based resistive sensors. Basic principles underlying the mechanism of gas sensing and the importance of nanostructure are stressed. The metal oxides used in this work, namely tungsten oxide (WO_3), molybdenum oxide (MoO_3), and titanium oxide (TiO_2) are introduced with a focus on their crystal structure. Finally, the problem addressed in this thesis is defined and a research plan is presented based on manipulating the crystal structure of metal oxides.

Chapter 2 cumulatively presents all the experimental techniques used in this work, for characterization and sensing.

Chapter 3 provides the results of characterization of the first class of metal oxides namely, nanostructured WO_3. The chapter is focused on two *isostructural polymorphic transformations* of WO_3, namely orthorhombic and monoclinic. Results of the gas sensing analysis carried out are also presented.

Chapter 4 introduces the second metal oxide investigated in this work, namely MoO_3. The effect of use of high aspect ratio nanostructures-nanowires of MoO_3 for gas sensing is presented in this chapter.

The use of *sensor arrays* for sensing is explored in Chapter 5, with the main focus on hydrocarbon sensing using rutile based hybrid sensors of MoO_3-TiO_2.

Chapter 6 discusses the results obtained for each metal oxide and attempts to provide an explanation for the sensing mechanism involved. Chapter 7 summarizes the major contributions of this dissertation and concludes it with several suggestions for future research directions.

Acknowledgements

I would like to extend my sincerest thanks to my thesis advisor Prof. P.I. Gouma. She has been a mentor, guide, role model and most important of all a friend. She has had the patience to hear out the wildest theories and offer constructive criticism. She has been a constant pillar of support and encouragement during times when I found my confidence wavering. A mere five lines here would not justify three and half year's worth of gratitude and debt. It would probably suffice to say that she has been what every advisor has to be and more.

I would like to thank Dr. Clive Clayton for his valuable insights during my preliminary examination that played a very important role in solidifying my research focus. I would also like to thank Dr. Devinder Mahajan for serving on my defense committee.

I am very grateful to Dr. David Kubinski, for being a very hospitable host during my visit to Ford Research Labs and for providing invaluable inputs for building and improving the sensing setup in our lab. I also thank him for taking time to be on my defense committee.

I gratefully acknowledge the support provided by the National Science Foundation through an NSF-NIRT grant (DMR-0304169).

I am deeply indebted to Dr. Hajime Haneda and Dr. Naoki Ohashi, at the Sensor Materials Center, National Institute of Materials Science, Tsukuba, Japan, for sponsoring my visit to their laboratory. My time at NIMS has been a wonderful research experience, and I take this opportunity to thank Dr. Masayuki Fujimoto, Dr. Takeo Ohsawa, Dr. Haruki Ryoken, for hours of enlightening discussion.

I would also like to thank Dr. Lihua Zhang, Dr. Eli Sutter and Dr. Yimei Zhu at the Center for Functional Nanomaterials, Brookhaven National Laboratory, for patiently training me on one of the best instruments I have used so far.

It would be mathematically correct to say that I have spent a better part of my life here in the United States in my lab. Rooms 201 and 203 in Old Engineering have been a second home to me and it could not have been so, if it were not for the people there. I would like to thank all my old and current lab members- Arun Prasad, Prashant Jha, Smita Gadre, Katarzyna Sawicka and Koushik Ramachandran for being wonderful labmates and great mentors. It would suffice to say that Aisha Bishop and Lisheng Wang have made me look forward to coming back to the lab everyday. I have learnt a lot from them and I hope the friendships struck over the past three years last for a long time to come.

Manisha, Rupa, Radhika, Suganya and Varna have offered me the ultimate support that one could have hoped for, in being always around when it mattered the most. Manisha has made me realize, perhaps one time too many what a serious business PhD was. I will always admire her for her steadfast dedication and relentless pursuit of excellence. Rupa, Radhika, Suganya and Varna have been and still are the most wonderful friends one could ask for.

Dr. Jim Quinn has been there every step of the way, helping me get trained on the instruments and providing valuable knowledge. Debby and Lynn have been the omnipresent and omniscient problem solvers. I have come to believe that there is nothing they can’t do.

And finally I would like to thank my wonderful family-my parents, my sister, my brother-in-law and my grandmother, for believing in me. They have been the most amazing support system and to them rightly this thesis is dedicated.

Vita

Krithika Kalyanasundaram

Born: August 30, 1982, Ambasamudram, India.

Education

B.E, (September 1999– May 2003), Metallurgical Engineering, Regional Engineering College, Tiruchirappalli, India.

Experience

Research Assistant (August 2004-till date), Dept. of Materials Science and Engineering, SUNY at Stony Brook, NY

International Research Assistant, (September 2006-December 2006), Sensor Chemistry Group, National Institute for Materials Science (NIMS), Tsukuba, Japan

Teaching Assistant (August 2004-July 2006), Dept. of Materials Science and Engineering, SUNY at Stony Brook, NY

Publications (Journal and Conference Proceedings)

1. **K. K. Iyer**, P. I. Gouma, "Nanostructured Metal oxides and their Hybrids for Gas sensing Applications"- Chapter to appear in "*Science and Technology of Gas Sensors: Chemiresistors*" D. K. Aswal and S. K. Gupta (eds.), Nova Publishers, expected in Spring 2005
2. **K. Kalyanasundaram**, P. I. Gouma, "Processing and Characterization of nanostructured metal oxides for Gas Sensing applications", *IEEJ Trans. SM* **126**, p. 560-567, 2006. [*Invited article*]
3. P.I. Gouma, **K. Kalyanasundaram,** A. Bishop, "Electrospun single-crystal MoO_3 nanowires for biochemistry sensing probes", *J. Mat. Res.* **21**, p. 2904-2910, 2006.
4. Teleki, S. E. Pratsinis, **K. Kalyanasundaram**, P. I. Gouma, "Sensing of Organic vapors by flame made TiO_2 nanoparticles", *Sens. and Actuators B* **119**, p. 683-690, 2006.
5. P. I. Gouma, A. Bishop, **K. K. Iyer**, "Single Crystal Metal Oxide Nanowires as Bio-Chem Sensing Probes", 6th East Asia Conference on Chemical Sensors, to be published in *Rare Metal Materials and Engineering*, **35**, p. 295-298, 2006.
6. P. I. Gouma, A. K. Prasad, **K. K. Iyer**, " Selective nanoprobes for Signalling gases", *Nanotechnology* **17**, pp. S48-S53, 2006
7. Cs.Balázsi, **K.Kalyanasundaram**, E. Ozkan Zayim, J. Pfeifer, A. L. Tóth, P.I. Gouma, "Tungsten oxide nanocrystals for electrochromic and sensing applications", in *Proceedings of the 1st International Congress on Ceramics* edited by S. Freiman (Wiley, Toronto, 2006), p.1-6.

8. **K.K. Iyer**, A. K. Prasad, P.I. Gouma, "A smart medical diagnostic tool using Resistive Sensor technology" in *Materials and Devices for Smart Systems II*, edited by Y. Furuya, J. Su, I. Takeuchi, V.K. Varadan, J. Ulicny (Mater. Res. Soc. Symp. Proc. 888, Warrendale, PA, 2005), 0888-V10-10.
9. P. I. Gouma, **K. K. Iyer**, P.K. Jha, "Novel Biocomposites for Biosensors based on resistive changes" in (IEEE Sensors 2005 Proceedings, Irvine, CA, 2005), 500.

CHAPTER 1

Introduction

Resistive gas sensors have been known nearly four decades now and their applications ranging from chemical hazard detectors to automotive sensors, from food quality monitors to the cosmetic industry. The idea of using gas sensors for detecting specific metabolites in breath is new and with the development of novel nanomaterials and nanostructures, highly sensitive sensors may be realized for ultra-low concentration detection of some gases in the human breath, but the real challenge is achieving the required level of selectivity (ability to detect a specific gas in the presence of other interfering gases). The work presented in this thesis involves the combination of nanotechnology and materials science to develop highly selective sensors for detection of specific analytes in human breath. But before starting on the experimental details and the choice of materials for sensing, there is a need to understand the science behind resistive gas sensing and the choice to use nanostructured materials for this application.

The purpose of this chapter is to introduce the concepts of chemical sensing- in particular resistive gas sensing. Beginning with a general definition of a 'sensor', a general classification of sensing technologies will be given. The second part introduces concept of resistive chemical gas sensing and the different sensing matrices used in resistive gas sensing with reasoning for using metal oxide transducing matrices instead of the others. The significance of using nanostructured sensing matrices is also outlined in

this section. The third part talks about the common methods of synthesizing metal oxides and also the operating parameters of a sensor.

1.1 Sensor-Definition and Classification

The word 'sensor' is derived from the Latin word '*sentire*', which means "to perceive" [1]. A sensor can thus be defined as a device that receives a stimulus – physical/chemical and transforms it in to a measurable output [1-2]. Thus a sensor can detect an input signal and convert it in to an appropriate output signal. In many instances it is difficult to classify the input signal as either purely physical/chemical (as in the case of chemisorption on metal oxide sensors). It may be considered a mixture of physical and chemical stimuli. A sensor thus can be seen as a combination of a chemically active receptor that reacts with the incoming stimulus (physical/chemical) and a transducer that converts the results of the above reaction to a measurable form.

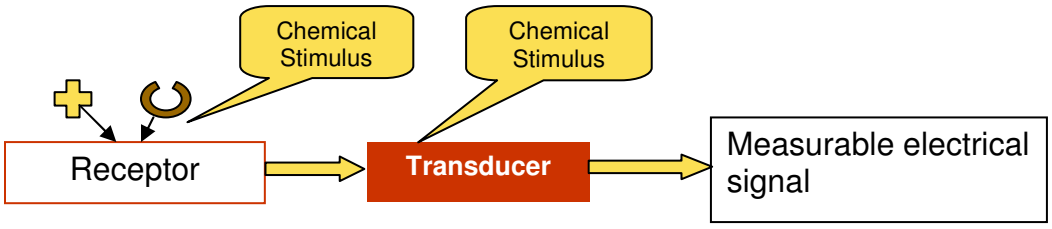

Figure 1.1: Concept of a Sensor

A chemical sensor is defined as one whose input is a chemical/environmental variation. The chemical signal can manifest itself in to several forms such as

-chemisorbed gaseous species that exchange electrons with the sensor

-A biological activity that translates either to gas species adsorption or a direct electrical input

-A pH change leading to a change in the modification of the electrical properties and so forth.

It will also be valuable to know from a materials scientist's point of view the materials used for constructing the sensing matrices. Though this list is not exhaustive, it attempts to present the most widely used class of materials.

Table 1.1: Classification of Sensor Materials

Type of Material	Employed widely as
Silicon- Probably the most widely used semiconductor, in sensors.	Piezoresitive sensors, SAW
Ceramics – Includes metal oxide, carbides, nitrides.	Metal Oxides- MOSFETs, Resistive Chemical sensors Metal nitride (ex. AlN), Metal Carbides (SiC)- SAW sensors
Metals	
Polymers – Conducting Polymers, Biologically functionalized polymers	Resistive Chemical Sensors, Bio sensors
Carbon – In the form of carbon black embedded in polymer matrices, carbon nanotubes with or without metals/metal oxides	Resistive Chemical Sensors

Dyes – Metallorganic, Organic	Optical Sensors, Resistive Gas Sensors

1.2 Metal Oxides- Resistive Gas Sensing

Metal oxides have been used nearly for four decades for gas sensing applications. The basic principle behind the gas sensing mechanism by metal oxides is the change in their electrical resistance on exposure to a gas, due to electronic exchange. The discoveries by Seiyama et al [3], in 1962 that ZnO thin films exhibit changes in their electrical conductivity with small amounts of reducing gases and the same year by Taguchi [4] et al that SnO_2 partially sintered pellets respond similarly were the beginning for what has been a rapid gas sensor developmental phase. Since 1968 Taguchi sensors have been mass produced and with the establishment of Figaro Engineering Inc. in 1969 the SnO_2 sensors have been commercially available [5]. What started with thick films and pressed pellet bulk sensors has now evolved in to novel nanoarchitectures for gas sensing applications that have sensitivities down to ppb levels.

Although conducting polymers also offer the feasibility of their use for gas sensing, metal oxides are more attractive, because of their ease of fabrication, advantage of easy integration with circuits and MEMS devices, better structural and chemical control, responses down to ppb levels of gases and relative inexpensiveness. On the other hand they currently offer only limited selectivity, are affected by humidity, and consume lots of power.

Before starting to stress the importance of the metal oxide in question, namely WO_3, it is imperative to understand the basic mechanism behind the gas sensing behavior of semiconducting metal oxides. Once the mechanism is established and understood, the

significance of the role played by metal oxides both commercially and scientifically will be elaborated.

Resistive gas sensing in very simple terms can be defined as the change in resistance of the sensor in response to a change in the gas atmosphere (gas, concentration of gas etc.). Metal oxide gas sensors are semiconductors at the operating temperature of the sensor, which implies that they have an excess of majority carriers arising from donor impurities (intrinsic such as oxygen vacancies or extrinsic such as dopants). Modulation of the number of charge carriers in response to a changing gaseous environment is the basic mechanism behind the operating principle of these sensors.

1.2.1 Principles of Resistive Gas Sensing

The most quoted model to explain the resistance change in a metal oxide semiconductor sensor is that, in air, oxygen adsorbs on the surface, dissociates to form O^-, where the electron on the oxygen, is extracted from the semiconductor. This electron extraction tends to increase the resistance (assuming an n-type semiconductor (whose majority charge carriers are electrons)). In the presence of a combustible gas, like say H_2, the hydrogen reacts with the adsorbed O^-, to form water and the electron is re-injected in to the semiconductor, tending to decrease the resistance. A competition results between the oxygen removing the electrons and the combustible gas restoring these electrons. So, the steady state value of resistance of the metal oxide depends on the concentration of the combustible gas. This could be illustrated in the following way, by considering the competing reactions:

$$O_2 + 2e^- \rightarrow 2O^- \qquad (1)$$

$$H_2 + O \rightarrow H_2O + e^- \quad (2)$$

The more the H_2 present the lower the density of O^-, the higher the electron density in the semiconductor, and thus lower the resistance.

Another model that may exist or co-exist is that the combustible gas, if chemically active, extracts a lattice-oxygen from the metal oxide, leaving vacancies that act as donors. The oxygen from the air tends to re-oxidize the metal oxide, removing the donor vacancies. Thus, there is a competition between the oxygen removing the vacancies and the combustible gas producing donor vacancies. The density of donor vacancies (and therefore the resistance) depends only on the concentration of combustible gas because the oxygen partial pressure is constant (as when operating in air) [6-7].

1.2.2 Surface States in Ionic crystals like SnO_2

There is always a lower level coordination at the surface where the crystal terminates. For example in the case of ionic crystals like SnO_2, the Sn ions have lesser than the bulk value of oxygen ions This makes the tin ions more attractive towards electrons, and their conduction bands can actually be at a lower energy level, thus enabling them to capture electrons from the bulk. They can also share an electron with a basic molecule such as OH^-. Similarly the oxygen ions that need more positively charged ions, will attract holes from the bulk, by shifting their valence orbitals to an energy level higher than the valence band edge. They can also give up their electron to a positive ion such as H^+. Thus the surface of most metal oxides is covered with dissociated water (H^+

and OH^-). As the temperature increases these water molecules evaporate, leaving sites open for gaseous reactions.

These new energy levels in the band gap that arise due to the electronic interaction of the metal oxide surface with the environment are termed as 'surface states' and play an important role in the process of gas sensing. These states are involved in electron exchange with the bulk. In the ideal case, if there was no electron exchange between the surface states and the bulk, it would result in a 'flat' band condition, as indicated in figure 1.1, where the electron concentration is uniform throughout. On the other hand if the states interact electronically with the bulk, it would lead to a double layer voltage at the surface and eventually to 'band bending'.

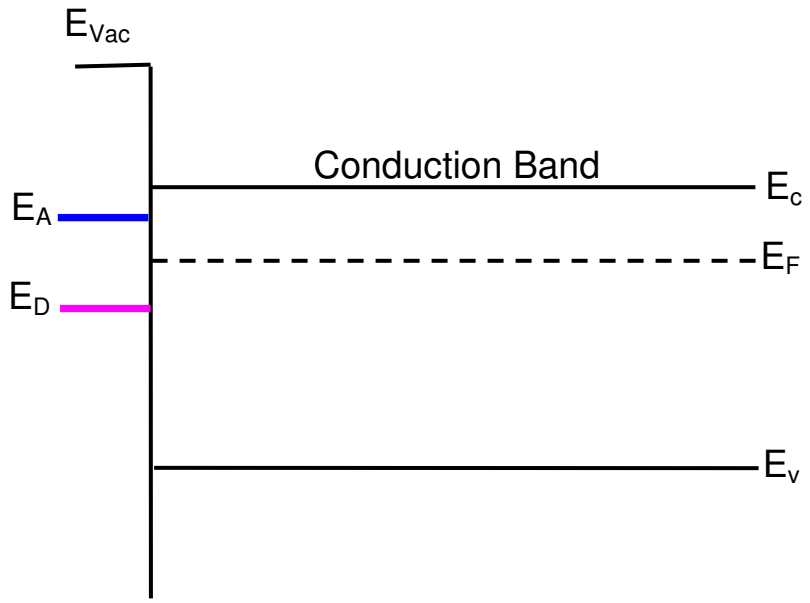

Figure 1.2: 'Flat Band' condition-No charge exchange between the surface states and the bulk.

This double layer can manifest itself in three forms, depending on the nature of the electronic interaction.

1) Depletion or Space Charge layer- forms when electrons are extracted from the conduction band of a n-type semiconductor. Similarly when electrons are injected or holes are extracted from a p-type semiconductor, it leads to the formation of a depletion layer (as depicted in figure 1.3).
2) Accumulation layer-forms when electrons are injected into an n-type semiconductor surface. For example when an acidic molecule such as H^+ donates an electron or accepts a hole from the surface state, this would lead to an accumulation of positive charges at the surface, that forms a double layer with the negatively charged semiconductor (as depicted in figure 1.4)
3) Inversion layer- forms due to a local inversion of the surface from n to p or vice-versa, in the presence of a strong oxidizing agent (figure 1.5)

The most important type of layer for gas sensing is the depletion layer. It was said earlier that the depletion layer forms in an 'n-type' semiconductor when electrons are extracted from it. Similarly in a p-type semiconductor this type of layer will form when holes are extracted from it. In an n-type semiconductor the double layer forms between the negatively charged surface states and the positively charged donor (immobile) ions in the bulk of the semiconductor. In a p-type semiconductor the double layer forms between the positively charged surface states and the negatively charged acceptor ions in the bulk. Thus a depletion layer is a 'space charge layer', which has been depleted of its majority carriers.

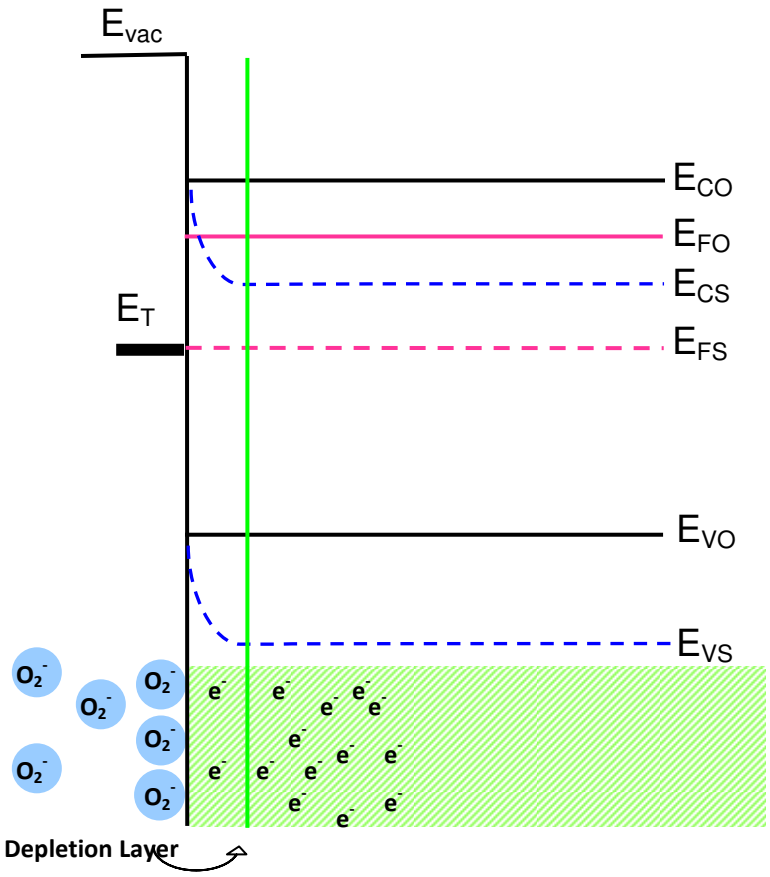

Figure 1.3: Formation of a depletion layer in an n-type semiconductor

An accumulation layer forms when majority carriers are injected in to the semiconductor surface. The double layer that builds up has a shape as shown in figure. 1.4.

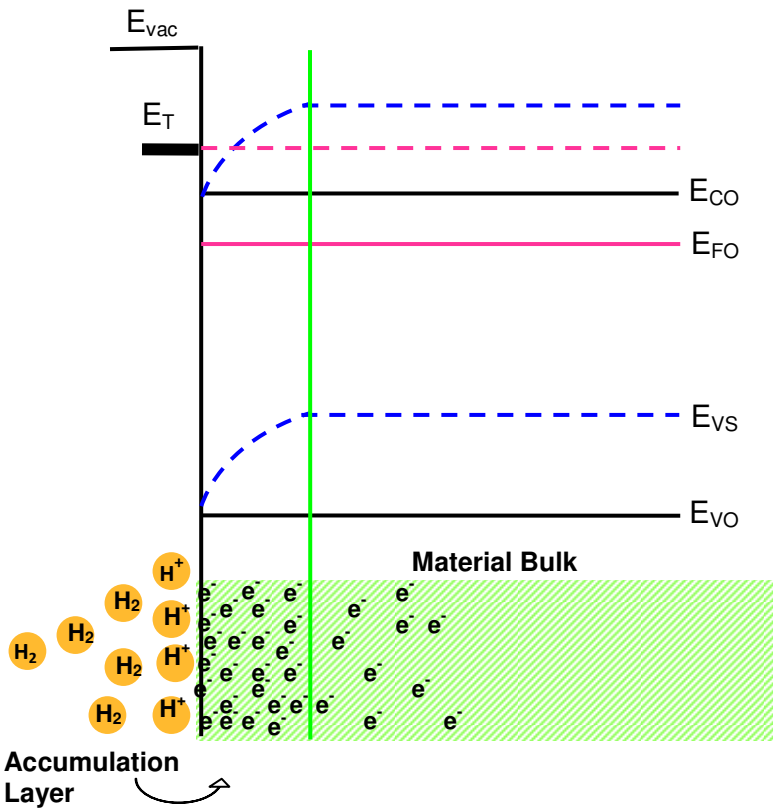

Figure 1.4: Formation of an accumulation layer between the electropositive surface species and the negatively charged semiconductor

An inversion layer (figure 1.5) forms when there is a local transition of conduction type on the semiconductor surface. For instance, an n-type semiconductor, in the presence of a very strong oxidizing agent such as fluorine can transform over a specific distance to p-type. Surface p-n or n-p transitions are crucial for some gas sensing applications and are discussed in more detail in the later section

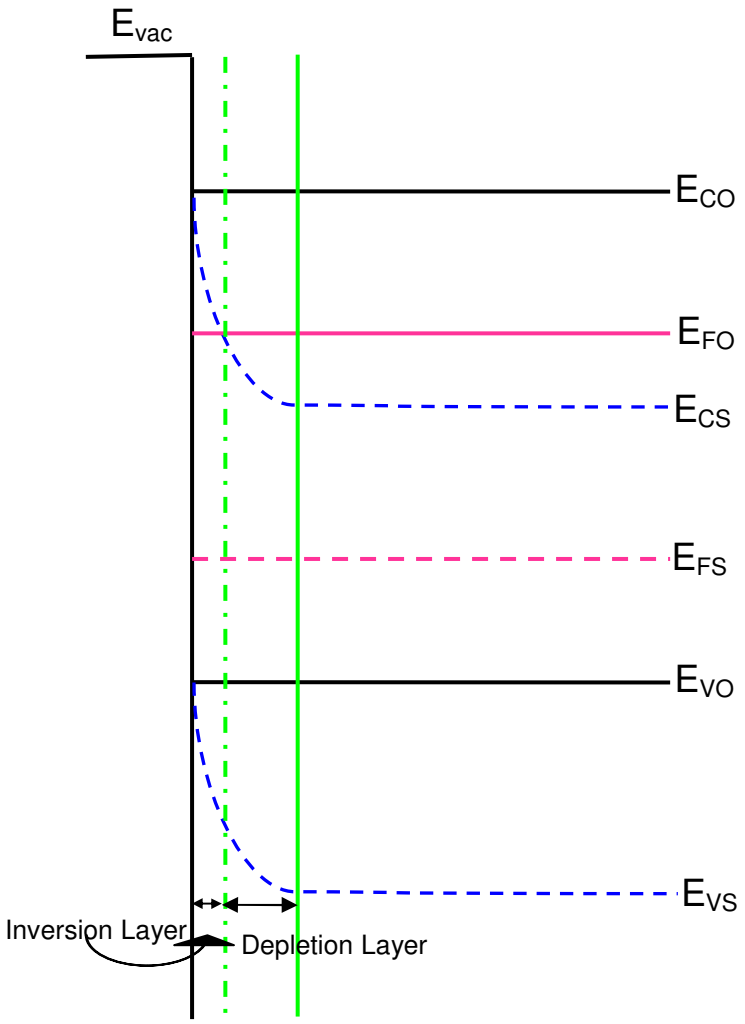

Figure1.5: Formation of an inversion layer in an n-type semiconductor

1.2.3 Concept of Fermi Level Pinning/Unpinning

The Fermi level energy (E_F) in a semiconductor represents the electrochemical potential of electrons in a semiconductor and is a thermodynamic entity such that the probability of finding an electron in an electronic energy level well above E_F is less that

½ and the probability of finding an electron well below E_F is close to unity. This can be defined by the fractional occupancy term *f* as follows

$$f = 1 \Big/ \left[1 + \exp(E - E_F)/kT\right] \tag{4}$$

The work function (χ, energy required to remove an electron from the inside of a semiconductor to a point just outside the surface), is given by

$$\chi = \varphi_s + \varphi_o + \varsigma \tag{5}$$

where, φ_s, is the electron affinity, φ_o, is the surface barrier and ς is the chemical potential and is defined as (μ-φ), where μ is the Fermi energy and φ=qΦ is the electrostatic potential of an electron. The work function term is strongly dependent upon the chemical species chemisorbed from the environment. Therefore its variation strongly defines the interaction of the semiconductor with the ambient [7-9]. These may be represented on the band diagram as depicted in figure 1.6

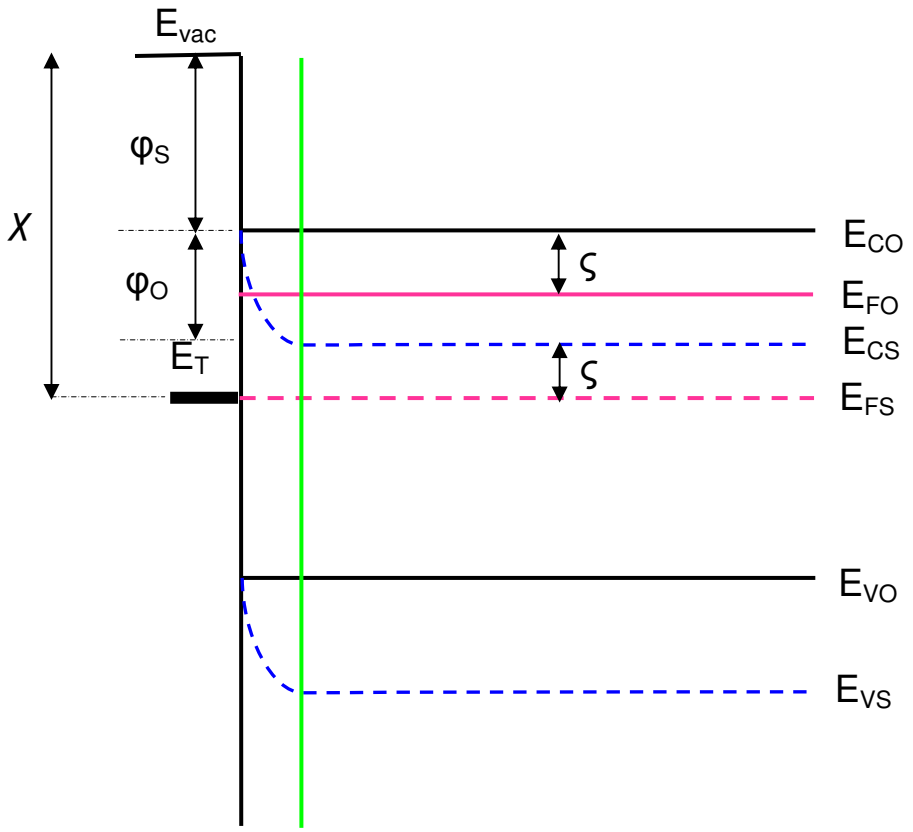

Figure 1.6: Band bending after chemisorption of charged species (here ionosorption of oxygen on E_{SS} levels χ denotes the work function, μ the electrochemical potential, and φ_s is the electron affinity, and φ_o or qV_s the surface barrier

It has been shown that in situations where the density of states (DOS) is very high, then the expression for surface barrier takes this form,

$$\varphi_o = \varepsilon_o - \varsigma \tag{6}$$

where, ε_o is the energy level of the surface states, and substitution in eq. (6) yields the limiting value for work function when DOS is very high, and is given by

$$\chi = \varphi_s + \varepsilon_o \tag{7}$$

It is evident from eq. (7) that the work function is independent of the Fermi energy, which is now pinned at the level of the surface state energy ε_o. On the other extreme when the DOS is vanishingly small, or in other words for a neutral surface, when φ_o is close to zero, the work function tends to be

$$\chi = \varphi_s - \varsigma \tag{8}$$

and in this case, the work function is indeed dependent on the Fermi energy. In conclusion it can be said that the presence of surface states on the surface of a semiconductor leads to the formation of a double layer and a space charge region in the semiconductor. If the DOS is large then it makes the work function independent of the Fermi energy (and so independent of the impurity content) and any variation in the work function can be compensated by the variation of electron affinity. Only when the density of surface states becomes small enough, then the variation of work function χ due to chemisorption will result in a variation of the surface barrier φ_o value.

It has also been recently established [10] that when the material is nanostructured (here nanostructured is defined as a material whose grain radius R is of the order of the width of depletion layer λ), unpinning effects become prominent, that is for nanostructured materials, the DOS has been found to be less than not nanostructured material, this making them more sensitive to changes in the atmosphere.

1.2.4 n-p type and p-n type transitions in semiconductor gas sensors

Semiconductor type transitions can occur during sensing. The exact mechanisms of transition are not exactly known though there are two possible explanations for it. The first one is a inversion layer formation on the surface that locally causes a transition from an n-p type or p-n type transition depending on the adsorbate. An inversion layer forms on the surface of an n-type semiconductor in the presence of a strong oxidizing agent which results in the formation of an acceptor surface state. If the surface state energy level is close to the valence band edge then to bring the Fermi level close to the surface state, the surface Fermi energy must be close to the valence band. In such a situation the acceptor surface state is so low in the band diagram that it extracts electrons from the valence band leaving a substantial hole concentration. This results in a local n-p type transition.

In the other case, the common mechanism that has been suggested is the formation of oxygen vacancies due to a loss of local stoichiometry [11]. In general, the conductivity of a semiconductor is given as,

$$\sigma = -qn\mu_n + qp\mu_p \tag{9}$$

where n and p, in Eq. (9) are the electron and hole concentrations respectively, q is the associated charge and μ is the associated charge mobility. When the concentration of either of the charge carriers becomes larger than the other, there is a shift in the type from p to n or n-to p. It has been found that the values of n and p depend on the

generation of inter-band traps due to the formation of vacancies or impurity substitution. It has been found in MoO_3 that there is a p-n type transition [12]. This might be due to the formation of oxygen vacancies that leads to excess electrons or incorporation of oxygen atoms in to these vacancies that leads to excess holes. When either of these values exceeds a threshold level there is a transition from one type of conduction to other.

1.3 Importance of 'nano' structure for gas sensing

Calculations for the results below have been originally carried out in [14] and have been derived from [13]. For grains/ crystallites large enough to have a bulk region unaffected by the surface phenomena i.e. when the grain diameter d >> Debye length λ_D the surface charge carrier density n_s, is given by Eq. 10.

$$n_s = n_b \exp(-qV_s / k_B T) \tag{10}$$

For the limiting case when the crystallite size d is $\leq \lambda_D$, the activation energy related to the Debye length as given in Eq. 11

$$\Delta E \sim k_B \,.\, T.\, \{R/2\lambda_D) \tag{11}$$

where, R is the radius of the cylindrical filament produced by sintering small grains. If the value of ΔE is comparable to thermal activation, then we have a homogeneous electron distribution in the filament and flat band conditions.

Some of these parameters like the concentration of free charge carriers (electrons), the Hall mobility μ, the Debye length λ_D, and the mean free path of the free charge carriers λ have been calculated for single crystal SnO_2 surfaces for various temperatures [13].

Table 1.2: Bulk and surface parameters of influence for SnO_2 single crystals. n_b is the concentration of free charge carriers (electrons), μ_b is their Hall mobility, λ_D is the Debye length, and λ is the mean free path of free charge carriers.

T (K)	400	500	600	700
n_b	1	11	58	260
μ_b (10^4 m^2/ (V_s))	178	87	49	31
λ_D (nm)	129	43	21	11
λ (nm)	1.96	1.07	0.66	0.45
$\Delta E/(k_B T)$ | (R=50 nm)	0.34	0.77	1.08	1.49

If ΔE is comparable to the thermal energy then a homogeneous electron concentration is attained in the grain and leads to the flat band case. For grain sizes lower than 50 nm, it has been shown that complete depletion of charge carriers occurs inside the grain and a flat band condition results for almost all temperatures except a few.

1.3.1 Fabrication of Nanostructured Metal Oxides

This section will try to provide a brief outline of the methods commonly used for the fabrication of nanostructured metal oxides. Conventional methods such as sol-gel and spray pyrolysis that are used in this work have been discussed in detail, while figure 1.7 provides a general idea about the other routes that are available for processing nanostructured metal oxides. Unconventional methods such as molecular self-assembly, thermal evaporation have been outlined as well.

1.3.1.1 Conventional Methods

The conventional methods are outlined in the schematic below. A brief overview of each of these techniques would also be provided.

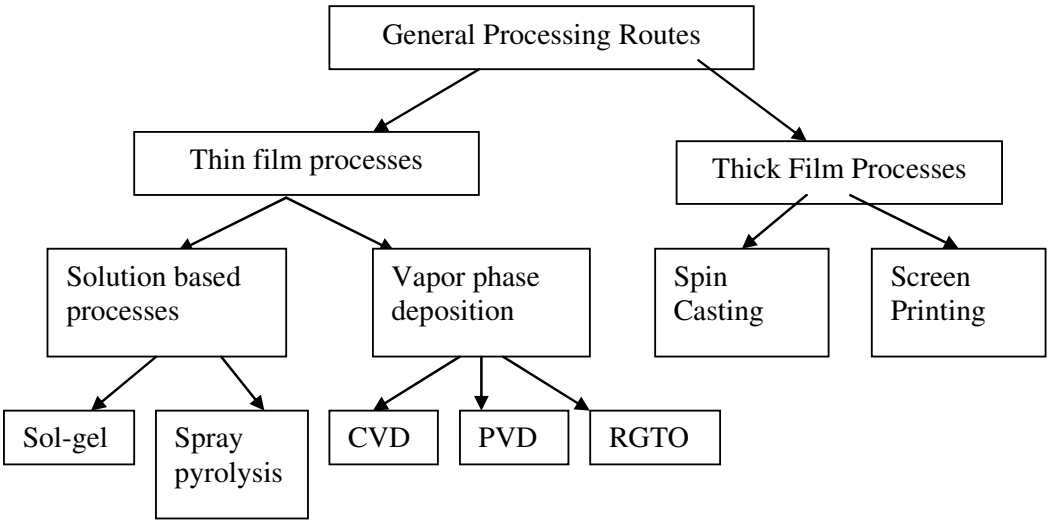

Figure 1.7: Schematic illustrating the commonly used techniques for nanostructured thin film deposition

1.3.1.1.1 Sol-gel Method: Sol-gel method, as schematically shown in figure 1.8, has been used for a long time for the production of nanomaterials. This is a room or slightly elevated temperature process. The process involves the hydrolysis of a metal organic compound such as a metal alkoxide [15],[16] (usually, or can be hexachlorides as well), or inorganic salts such as chlorides [17],[18] to produce a colloidal sol. The hydrolysis can take place with the help of alcohol, acid or base. The sol is then allowed to age and settle. This is referred to as the gelation step.

The versatility of the process lies the in the flexibility available for the form of the end product such as

- The sol can be coated on the substrate by either spin/dip coating to form a 'xerogel' film
- The solvent from the sol can be evaporated to precipitate particles of uniform size and then these can be screen printed
- The sol can be allowed to gel completely to obtain either a xerogel or an aerogel.
- The sol can be spun cast to form ceramic fibers

Sol-gel processing also allows one to introduce second phase particles producing doped metal oxides or mixed metal oxides [19] hence helping to improve the gas sensitivity and selectivity of the gas sensing matrix.

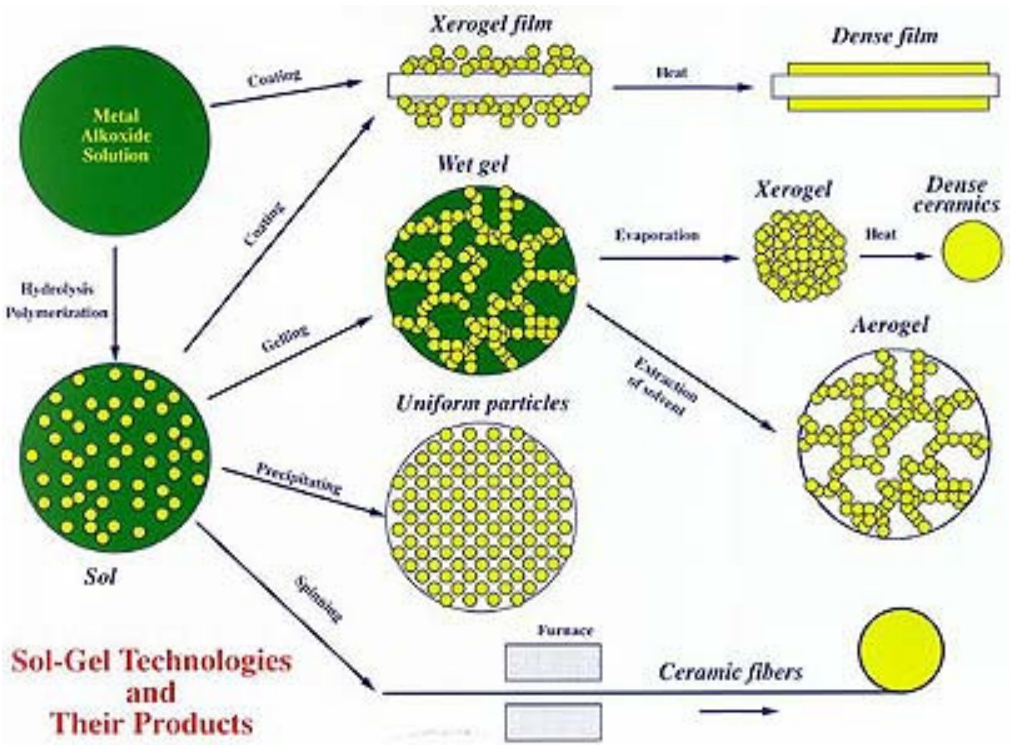

Figure 1.8 Schematic of the sol-gel processing technique (www.chemat.com).

1.3.1.1.2 Spray Pyrolysis: This process involves the atomization of a liquid precursor through a series of reactors, where the aerosol droplets undergo evaporation, solute condensation within the droplet, drying, thermolysis of the precipitate particle at higher temperature to form a microporous particle which then gets sintered to give a dense particle [20].

The advantages of using a spray pyrolysis are as follows:

- The process makes use of the wide variety of available solution chemistries compartmentalizing the solution in to unique droplets, thereby retaining very good stoichiometry on the particle surface. This is particularly useful for the synthesis of single and mixed metal oxides [20]
- A variety of particle morphologies can be obtained such as core-shell morphologies, porous particles for catalyst support, fibers, nanocomposites, quantum dots and hollow nanoparticles, to mention a few [20].

There are a variety of spray pyrolysis processes, and a few of them are aerosol thermolysis, flame spray pyrolysis, aerosol decomposition, spray roasting, and aerosol decomposition.

1.3.1.2 Unconventional Methods

Recently there have been a lot of reports of synthesis of 2D and 1D nanostructures such as nanowires, nanobelts, nanorods, nanodiskettes of metal oxides, with a large surface area to volume ratio. These novel nanoassemblies are expected to possess unique properties such as very high sensitivities to single molecules or few ppbs of gases, quantum confinement.

Ref. [21] outlines the strategies for achieving one dimensional growth. It has been generally accepted that there must exist a reversible pathway between the building blocks on the solid surface and the fluid phase (liquid, vapor, gas). The building blocks also need to be supplied at a controlled rate in order to achieve uniform composition and

morphology. The general strategies for achieving 1D growth can be summarized as follows:

- Use of intrinsically anisotropic crystal structure
- Introduction of a solid-liquid interface to reduce the symmetry of the seed
- Use of templates to achieve directional growth
- Use of supersaturation control to modify the habit of the seed
- Use of capping agents to control the growth of various crystal facets
- Self-assembly of 0D nanostructures
- Size reduction of 1D nanostructures

1.4 Sensor Attributes

For optimizing and standardizing the performance of any device, it is necessary to define a set of operating parameters. Hence this section will be devoted to defining and understanding the basic operating parameters of a sensing device, namely

- Sensitivity
- Selectivity
- Stability

Sensitivity very roughly can be defined as the magnitude of response of a sensor to a particular target analyte. Mathematically, several definitions exist, and the usage primarily depends on the application. The three most widely used are given below.

$$S = \Delta R / R_0 \tag{12}$$

where S = sensitivity

$\Delta R = R_g - R_o$

R_g = Resistance of the sensor in the target gas

R_o = Resistance of the sensor in air, also referred to as the 'baseline' resistance.

Two other definitions that give a normalized view of sensitivity are given in eq. (13) and eq. (14)

$$S_O = R_g / R_o \tag{13}$$

$$S_R = R_o / R_g \tag{14}$$

where S_O = Sensitivity of the sensor in oxidizing gas atmosphere and,

S_R = Sensitivity of the sensor in reducing gas atmosphere

Selectivity, the second parameter may be defined as the sensor response to a particular gas in a mixture of interfering gases. This parameter defines the specific response of the sensor and is one of the primary motivators for this research.

Sensor stability refers to the long term operation of a sensor without any change in the above operating parameters. Gradual changes in the properties of the sensing matrix that commonly accompany the prolonged use of a sensor in changing gas

environments at elevated temperatures is referred to as 'drift' and it is desirable to minimize the drift as much as possible.

Response time is defined as the time taken by the sensor to reach 90% of the final response value and recovery time is defined the time taken by the sensor to come to 90% value of the original baseline.

1.5 Tungsten Trioxide

The first class of material to be analyzed here belongs to the modified cubic perovskite structure, namely tungsten oxide-WO_3. Tungsten trioxide is a wide band gap semiconductor with a bulk bad gap values variedly quoted from 1.6eV for the hypothetical perovskite structure to 2.4eV in the full monoclinic structure and the accuracy of the calculations in the literature is still debatable owing to the tremendous amount of approximations involved [22-23]. The maximum value of the band gap quoted in the literature is 3.25eV [24]. It has been widely used in photocatalytic [25], electro/photochromic [26-27] applications prior to its use as a gas sensor. Its potential use as a gas sensor for H_2S and NO/NO_2 was discovered fifteen years earlier [28]. Further the research on nanostructured WO_3 based sensors started a decade earlier [29]. From the onset itself WO_3 was known for its good sensitivity towards NO_x, H_2S [30-49] and NH_3 [30,39,45,50-63].

1.5.1. Structure of Tungsten Trioxide:

Tungsten trioxide belongs to the family of metal oxides that derive their crystal structures based on ReO_3- a perovskite. Structure of cubic ReO_3 is given in Fig 1.9.

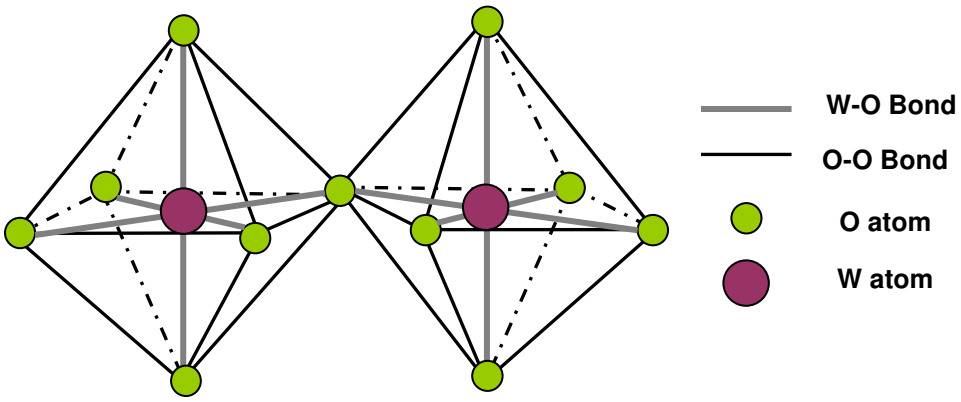

Figure 1.9: Idealized cubic perovskite ABO_3 like structure showing the corner sharing oxygen octahedra.

In the idealized cubic ReO_3 unit cell (one atom per unit cell), which is composed of corner sharing oxygen octahedra, the Re atom occupies the center of the octahedron. The WO_3 structure is a distortion of the cubic ReO_3 structure with the W atoms occupying the cube corners and the oxygen atoms along the cube edges. Each W atom thus is surrounded by an octahedron of oxygen atoms. The octahedra are slightly distorted and this leads to the lower symmetry compared to the cubic ReO_3 structure. It has been found that the displacement of the tungsten atom inside the octahedra is stabilized by an increase in the covalence between the tungsten and oxygen atoms [64] and the cubic form is thermodynamically unstable and rearranges itself in to the monoclinic form upon heating to 1000°C.

Table 1.3: Crystal structures, the unit cell parameters, the transformation temperatures of WO_3

Crystal Structure	a (Å)	b (Å)	c (Å)	α (°)	β (°)	γ (°)	Stability regime	Reference
Triclinic	7.31	7.52	7.69	88.8	90.9	90.9	<17	65
Monoclinic	7.30	7.54	7.69	90	90.9	90	17-320	65
Orthorhombic	7.34	7.57	7.75	90	90	90	330-740	66,67, 68
	7.38	7.51	3.85	90	90	90		
Hexagonal	7.298	7.298	7.798	90	90	120	-	69,
Tetragonal	5.191 5.25	5.191 5.25	3.858 3.91	90 90	90 90	90 90	>740	67,70
Cubic	7.521	7.521	7.521	90	90	90	-	70

1.5.2 Orthorhombic and Monoclinic WO_3:

The orthorhombic crystal structure which is more relevant to this report is explained in little detail below. In the orthorhombic form also WO_3 exhibits perovskite like distortion (although lesser than the triclinic and monoclinic structures). A schematic of the ReO_3 based WO_3 structure is depicted in Fig 1.10.

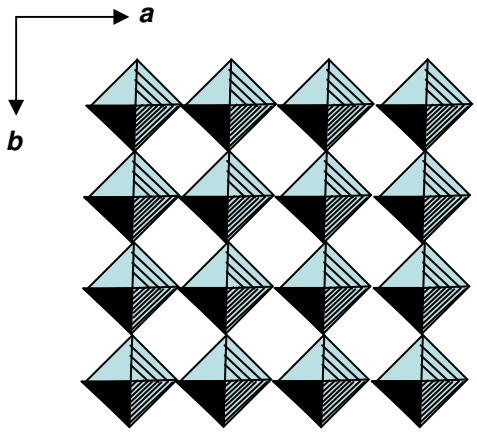

Figure 1.10: Structure of WO_3 based on the ReO_3 structure, showing the distorted WO_6 octahedra [adapted from 71]

It is also considered to be an ordered version of the room temperature monoclinic structure [66]. Monoclinic and orthorhombic unit cells are isostructural with differing amounts of distortion. The mechanism of transformation from monoclinic to orthorhombic WO_3 has been explored and is characterized by a decrease in the W-O displacement along the [001] direction and this is possible by shifting the W atoms by tilting the octahedra [73].

1.5.3 Hexagonal WO_3

As listed earlier, there are two metastable forms of WO_3-cubic and hexagonal. Hexagonal WO_3 (h-WO_3) is of interest to the study here because it belongs to the third class of oxides with a loosely bound layered structure. The crystal structure is unique in that the lattice is made up of corner sharing octahedra with long hexagonal and triangular prism channels parallel to the c-axis. This makes the material very open, allowing easy

movement of gas molecules and ions into and out of the material. Tungsten bronzes frequently crystallize in a hexagonal lattice, when the hexagonal tunnels are interpolated with specific cations [74]. But recently there have been reports of synthesis of pure h-WO_3 obtained by dehydration of an orthorhombic WO_3.1/3 H_2O precursor. Since then, there has been a lot of interest in synthesizing h-WO_3 as a matrix for intercalating metal ions for rechargeable batteries (Li^+ [75]) and electrodes. Lithium ion batteries are vital for advancing the field of portable electronics. They operate by reversibly inserting Li^+ ions from the electrolyte into the electrodes and in the process generating electricity. Reversible intercalation of Li^+ ions in to the host matrix is crucial for battery operation and can be accomplished by having electrode materials that have relatively open crystal structures [76]. Thermodynamically stable crystal structures are typically close-packed, whereas metastable oxide phases have open lattices that promote very high diffusion rates for intercalating ions.

In the area of resistive gas sensing, the attraction of hexagonal WO_3 lies in the structural similarity it shares with the orthorhombic form of MoO_3. Both these crystal structures have layered oxygen octahedra, in other words an open lattice structure, that provides long paths for small, diffusing gas molecules and facilitates easy removal of oxygen ions from the lattice. It is evident from our earlier research that the crystal structure plays a key role in determining selectivity of the sensing matrix [77]. Orthorhombic MoO_3 has been shown to be selective to ammonia in the presence of other gases. MoO_3 with its low sublimation temperature is not a suitable candidate for prolonged use at elevated temperatures. WO_3 on the other hand has higher structural integrity than MoO_3 and hence ideal for high temperature sensor applications. Also the

high aspect ratio of the nanowires will serve to improve the energy density of the batteries without increasing the effective volume of the battery.

1.5.4 Nitrogen oxides

Nitrogen oxides are a mixture of gases that are composed of nitrogen and oxygen. Two of the most toxicologically significant nitrogen oxides are nitric oxide and nitrogen dioxide; both are nonflammable and colorless to brown at room temperature. Nitric oxide is a sharp sweet-smelling gas at room temperature, whereas nitrogen dioxide has a strong, harsh odor and is a liquid at room temperature, becoming a reddish-brown gas above 70°F. Nitrogen oxides are released to the air from the exhaust of motor vehicles, the burning of coal, oil, or natural gas, and during processes such as arc welding, electroplating, engraving, and dynamite blasting. They are also produced commercially by reacting nitric acid with metals or cellulose. Nitrogen oxides are used in the production of nitric acid, lacquers, dyes, and other chemicals. Nitrogen oxides are also used in rocket fuels, nitration of organic chemicals, and the manufacture of explosives [78].

1.5.4.1. Nitric Oxide in human breath:

Nitric oxide is a well known free radical in the realm of respiratory medicine with particular significance to oxidative stress. It is also a highly diffusible gas and direct measurements of NO in human blood has been complicated due to the fact that it reacts with hemoglobin or other Fe^{2+} containing proteins. Currently methods such as measurement of nitrites and nitrates allow indirect measurement of NO content in blood.

NO in low concentrations is stable in gas phase. It is excreted in human airways, and is detectable in exhaled air [79-80]. The method currently used to measure exhaled NO is chemiluminescence. The NO contained in a sample reacts with an excess of ozone to produce NO_2 with an electron in an excited state (NO_2*). NO_2* reverts back to ground state (NO_2), while releasing electromagnetic radiation in the wavelength of 600-3000 nm range. The chemiluminescence is detected by a photomultiplier tube that converts the luminescence in to a readable electrical signal. The technique is highly sensitive, offering sensitivities down to a concentration of 1 ppb. Other techniques that can also be used are mass spectrometry and gas chromatography-mass spectrometry (GC-MS).

Although it is now well established that tungsten oxide is a good sensor for NO_x, the sensing mechanism and technique for achieving selectivity has not been explored fully and the purpose of this study is to resolve the issues of selective gas sensing in WO_3.

1.6 Molybdenum Oxide

Molybdenum oxide contains a family of oxides that form in various crystal structures such as orthorhombic, monoclinic, hexagonal, tetragonal etc. and also incorporate the well-known 'Magneli' (MoO_{3-x}) phases. Among these, molybdenum trioxide is an n-type semiconductor wherein the conductivity is a function of lattice oxygen deficiencies and has a band gap of 3.2eV. Molybdenum trioxide is an interesting oxide in the fact that it has a modified cubic ReO_3 structure and the orthorhombic form of MoO_3 has a unique layered morphology with distorted edge-sharing octahedra. Octahedral layers share edges along the a-axis [100] and corners along the c-axis [001].

This layered morphology of orthorhombic MoO_3 makes it selective towards nitrogen containing gases-amines such as NH_3 [81] as evidenced from the earlier work in our lab. The work done in this thesis involves the synthesis of one dimensional nanostructures of MoO_3 in order to examine the effect of reducing dimensionality on the sensitivity of the sensor.

1.6.1 Ammonia

Ammonia is a toxic, colorless gas with a pungent smell. It is environmentally significant as many chemical processes involving nitrogen containing compounds produce ammonia [82]. Ammonia is also a very important biomarker for diseases such as renal failure, and H. Pylori infection [83]. Elevated levels of ammonia can be found in the breath of patients with these conditions and hence it can serve as valuable marker for non-invasive diagnosis.

1.7 Titanium Dioxide

Titanium dioxide (TiO_2) or Titania as it is commonly referred to occurs in two crystal structure modifications anatase and rutile [84]. Ti^{4+} ions are in an octahedral coordination with the surrounding O^{2-} ions. The rutile structure has a higher symmetry compared to the anatase. Anatase is a metastable phase transforming to rutile at higher temperatures. The transformation temperature primarily depends on the initial anatase grain size [85]. TiO_2 has been used extensively for sensing CO [86-87], H_2 [88], ethanol [89-90].

1.8 Statement of the Problem

Human breath is composed of nearly 250 gases, some of them in concentrations of the order of parts per trillion (ppt). Nearly 70% of breath is CO_2. It has been known from medical literature for quite some time that products of certain metabolic activities end up being part of human breath and thereby can provide very valuable information about the human body in a non-invasive manner. For instance in people with elevated levels of cholesterol a higher concentration of isoprene, a product of the breakdown of cholesterol, is found and in patients with renal diseases ammonia may be sensed in breath. Acetone has been known for a long time to be associated with patients with diabetes. The real benefit of using resistive gas sensors is that they offer a means for non-invasive diagnostics; they can be portable and give instant results.

Although there are sensors that are very sensitive to the above gases the real challenge is in making a sensor that is selective, i.e., a sensor that can detect a particular gas in a mixture of interfering gases. Now, one may argue that this is impossible since there are hundreds of these gases in human breath as explained earlier, but we need worry only about those that are present in significant concentrations (and they will be, in patients with certain medical conditions), compared to others.

Metal oxides can be made selective or partially selective using some techniques or combination of techniques, such as using catalysts or promoters, using a specific crystal structure in the metal oxide sensing matrix and temperature modulation (reactivity of the gases vary depending on the temperature). Catalysts are a very attractive choice because they provide a ready-made solution, but the problem lies in the fact that over prolonged

periods of use at elevated temperatures, they undergo unpredictable phase transformations that is detrimental to the operation of the sensor. Using a pure metal oxide is the best choice in order not to compromise the integrity of the sensor. They have known and predictable crystal orientations. The chemical interaction of the gas that leads to electrical property change in the metal oxide is ultimately dependent on how the gas interacts with the exposed crystal planes and directions. Each atomic plane has a unique surface structure and hence unique activation energy for a particular gaseous reaction. By utilizing the polymorphic transformations of the metal oxide and by exercising a strict control on the crystal structure, the crystal surfaces exposed to the gases may be controlled. The table given below shows a working hypothesis of the principle behind selectivity in gas sensors.

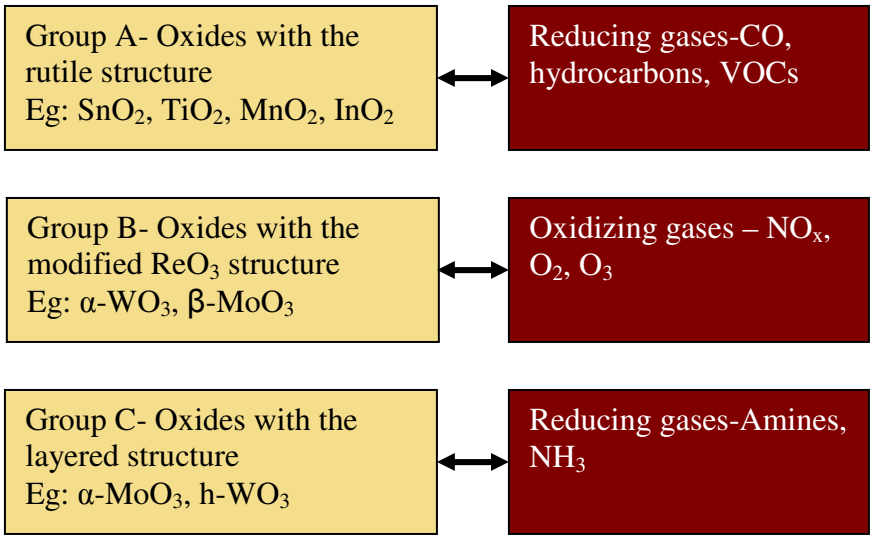

By choosing a sensor from the appropriate group and by using a group of sensors with known selectivity, an array can be built the response of which can be conditioned to a particular gas or class of gases.

References:

1. S.M. Sze, Semiconductor Sensors, Edited by. S.M. Sze., (John Wiley & Sons Inc., New York, 1994), p. 1.
2. A. Hulanicki, S. Glab, F. Ingman, "Chemical Sensors Definitions and Classification", Pure & Appl. Chem. **63**, (1991), p. 1247-1250.
3. T. Seiyama, A. Kato, K. Fujishi and M. Nagatani, *Analytical Chemistry* **34(11)**, (1962), p. 1502.
4. N. Taguchi, Japanese Patent Application, 1962.
5. www.figaro.co.jp/en.company3.html
6. S. M. Sze, Semiconductor Sensors, 1st edition, (John Wiley & Sons Inc.)
7. S.R. Morrison, The Chemical Physics of Surfaces, (Plenum, New York, 1977).
8. J. Bardeen, "Surface states and rectification at a metal semiconductor contact", *Phys. Rev*.**71,** (1947), p. 717-727.
9. C. Malagù, M.C. Carotta, E. Comini, G. Faglia, A. Giberti, V. Guidi, T.G.G. Maffeis, G. Martinelli, G. Sberveglieri and S.P. Wilks, "Photo induced unpinning of Fermi level in WO_3", *Sensors* **5**, (2005), p. 594-603.
10. C. Malagù, V. Guidi, M.C. Carotta and G. Maritnelli, "Unpinning of Fermi Level in nanocrystalline semiconductors", *Appl. Phys. Lett.* **84**, (2004), p. 4158-4160.
11. O.J.Gregory, Q. Luo, J.M.Bienkiewicz, B.M.Erwin and E.E.Crisman, "An apparent n to p transition in reactively sputtered indium–tin–oxide high temperature strain gages", *Thin Solid Films* **405**, (2002), p. 263-269.

12. A.K. Prasad, D.J. Kubinski and P.I. Gouma, "Comparison of Sol-gel and Ion beam deposited MoO_3 thin films for selective ammonia detection", *Sensors and Actuators B* **93**, (2003), p.25-30.

13. N. Barsan and U. Weimar, *J. of Electroceramics* **7**, (2001), p.167.

14. N. Barsan, *Sensors and Actuators B* **17**, (1994), p. 249

15. Galatsis, K.; Li, Y.X.; Wlodarski, W.; Kalantar-zadeh, K. *Sens. Actuators, B* 2001, 77, 478-483.

16. Kaciulis, S.; Pandolfi, L.; Viticoli, S.; Sberveglieri, G.; Zampiceni, E.; Wlodarski, W.; Galatsis, K.; X. Li, Y. *Surf. Interface Anal.* 2002, 34, 672-676.

17. Shieh, J.; Feng, H.M.; Hong M.H.; Juang, H.Y. *Sens. Actuators, B* 2002, 86, 75-80.

18. Gu, F.; Wang, S.F.; Song, C.F.; Lü, M.K.; Qi, Y.X.; Zhou, G.J.; Xu D.; Yuan, D.R. *Chem. Phys. Lett.* 2003, 372, 451-454.

19. Garzella, C.; Bontempi, E.; Depero, L.E.; Vomiero, A.; Della Mea G.; Sberveglieri, G. *Sens. Actuators, B* 2003, 93, 495-502.

20. Messing, G. L.; Zhang S-C.; Jayanthi, G.V. *J. Am. Ceram. Soc.* 1993, 76, 2707-2726.

21. Y. Xia, P. Yang, Y. Sun, Y. Wu, B. Mayers, B.Gates, Y. Yin, F. Kim, H. Yan, *Adv. Mater.* 2003, 15, 353-389.

22. D.W. Bullett, "Bulk and surface electrons states in WO_3 and tungsten bronzes", *J. Phys. C: Solid. State Phys.* **16**, (1983), p. 2197-2207.

23. G.A. de Wijs, P.K. de Boer and R.A. de Groot, “Anomalous behavior of the semiconducting gap in WO_3 from first- principle calculations”, *Phys. Rev. B.* **59**, (1999), p. 2684-2693.

24. C. Bechinger, E. Wirth and P. Leiderer, “Photochromic coloration of WO_3 with visible light”, *Appl. Phys. Lett.* **68**, (1996), p. 2834-2836.

25. L. Lietti, J. L. Alemany, P. Forzatti, G. Busca, G. Ramis, E. Giamello and F. Bregani, “Reactivity of V_2O_5-WO_3/TiO_2 catalysts in the selective catalytic reduction of nitric oxide by ammonia”, Catal. Today. **29**, 1996, p. 143-148.

26. C.G. Granqvist, Handbook of Inorganic Electrochromic materials, Elsevier, Amsterdam, 1995.

27. J. Livage and G. Guzman, “Aqueous precursors for electrochromic tungsten oxide hydrates”, Solid State Ionics **84**, 1996, p. 205-211.

28. E.P.S. Barrett, G.C. Georgiades and P.A. Sermon, “The mechanism of operation of WO_3 based H_2S sensors”, *Sens. Actuators B.* **1**, (1990), p.116-120

29. H. M. Lin, C. M. Hsu, H. Y. Yang, P. Y. Leeb, and C. C. Yang, “Nanocrystalline WO_3 based H_2S sensors”, *Sens. Actuators B.* **22**, (1994), p.63-68.

30. M. Stankova, X. Vilanova, J. Calderer, E. Llobet, J. Brezmes, I. Gràcia, C. Cané and X. Correig, “Sensitivity and selectivity improvement of rf sputtered WO_3 microhotplate gas sensors”, *Sens. Actuators B.***113**, (2006), p. 241-248.

31. M. Stankova, X. Vilanova, J. Calderer, I. Gracia, C. Cane and X. Correig, “Nanograin WO_3 thin films as active layer for resistive type gas sensors”, *J. Optoelectron Adv Mater*, **7**, (2005), p. 1237-1242.

32. A. Hoel, L.R.Reyes, S. Saukko, P. Heszler, V. Lantto and C.G. Granqvist, "Gas sensing with films of nanocrystalline WO_3 and Pd made by advanced reactive gas deposition", *Sens. Actuators B* **105**, (2005), p.283-289.

33. R. Ionescu, A. Hoel, C.G. Granqvist, E. Llobet and P. Heszler, "Ethanol and H_2S gas detection in air and in reducing and oxidising ambience: application of pattern recognition to analyse the output from temperature-modulated nanoparticulate WO_3 gas sensors", *Sens. Actuators B* **104**, (2005), p. 124-131.

34. R. Ionescu, A. Hoel, C.G. Granqvist, E. Llobet and P. Heszler, "Low-level detection of ethanol and H_2S with temperature-modulated WO_3 nanoparticle gas sensors", *Sens. Actuator B-Chem*. **104,** (2005), p. 132-139.

35. A. Hoel, L.F. Reyes, P. Heszler, V. Lantto and C.G. Granqvist, "Nanomaterials for environmental applications: novel WO_3-based gas sensors made by advanced gas deposition", *Curr. Appl. Phys.* **4,** (2004), p. 547-553.

36. O. Berger, W. J. Fischer and V. Melev, "Tungsten-oxide thin films as novel materials with high sensitivity and selectivity to NO_2, O_3 and H_2S - Part I: Preparation and microstructural characterization of the tungsten-oxide thin films" *J. Mater. Sci.-Mater. Electron*, **15,** (2004), p. 463-482.

37. O. Berger, T. Hoffmann, W.J. Fischer and V. Melev, "Tungsten-oxide thin films as novel materials with high sensitivity and selectivity to NO_2, O_3, and H_2S - Part II: Application as gas sensors", *J. Mater. Sci.-Mater. Electron*. **15**, (2004), p. 483-493.

38. I. Jimenez, J. Arbiol, G. Dezanneau, A. Cornet, and J.R. Morante, "Crystalline structure, defects and gas sensor response to NO_2 and H_2S of tungsten trioxide nanopowders", *Sens. Actuator B-Chem.* **93**, (2003), p. 475-485.

39. S.D. Han, I. Singh, H.S. Kim, S.T. Kim, Y.H. Jung and B.K. Kim, "H_2S gas sensing characteristics of WO3 thick-films", *Indian J. Chem. Sect A-Inorg. Bio-Inorg. Phys. Theor. Anal. Chem.* **41**, (2002), p. 1832-1836.

40. M. Penza, G. Cassano, and F. Tortorella, "Gas recognition by activated WO_3 thin-film sensors array", *Sens. Actuator B-Chem.***81**, (2001), p. 115-121.

41. J.L. Solis, S. Saukko, L. Kish, C.G. Granqvist and V. Lantto, "Semiconductor gas sensors based on nanostructured tungsten oxide", *Thin Solid Films*, **391**, (2001), p. 255-260.

42. J.L. Solis, S. Saukko, L. Kish, C.G. Granqvist and V. Lantto, "Nanocrystalline tungsten oxide thick-films with high sensitivity to H_2S at room temperature", *Sens. Actuator B-Chem.***77**, (2001), p. 316-321.

43. S.C. Moulzolf, S.A. Ding, and R.J. Lad, "Stoichiometry and microstructure effects on tungsten oxide chemiresistive films", *Sens. Actuator B-Chem.* **77**, (2001), p. 375-382.

44. J.L. Solis, A. Heel, L.B. Kish, C.G. Granqvist, S. Saukko and V. Lantto, "Gas-sensing properties of nanocrystalline WO_3 films made by advanced reactive gas deposition", *J. Am. Ceram. Soc.* **84**, (2001), p. 1504-1508.

45. S. Ehrmann, J. Jungst, J. Goschnick, and D. Everhard, "Application of a gas sensor microarray to human breath analysis", *Sens. Actuator B-Chem.* **65**, (2000), p. 247-249.

46. H.M. Lin, C.M Hsu, H.Y. Yang, P.Y. Leeb and C.C. Yang, "Nanocrystalline WO_3 based H_2S sensors", *Sens. Actuator B-Chem* .**22**, (1994), p. 63-68.

47. M. Ando, S. Suto, T. Suzuki, T. Tsuchida, C. Nakayama, N. Miura and N. Yamazoe, "H_2S and CH_3SH sensing using a thick film of gold loaded tungsten-oxide", *Chem. Lett.* (2), (1994), p. 335-338.

48. D.J. Smith, J.F. Vetelino, R.S. Falconer and E.L. Wittman, "Statbility, sensitivity and selectivity of tungsten trioxide films for sensing applications", *Sens. Actuator B-Chem*. **13**, (1993), p. 264-268.

49. D.J. Dwyer, "Surface chemistry of gas sensors-H_2S on WO_3 films", *Sens. Actuator B-Chem*. **5**, (1991), p.155-159.

50. M. Sriyudthsak and S. Supothina, "Humidity-insensitive and low oxygen dependence tungsten oxide gas sensors", *Sens. Actuator B-Chem*. **113**, (2006), p. 265-271.

51. V. Khatko, J. Calderer, E. Llobet and X. Correig, "New technology of metal oxide thin film preparation for chemical sensor application", *Sens. Actuator B-Chem.* **109**, (2005), p. 128-134.

52. I. Jimenez, A.M. Vila, A.C. Calveras and J.R. Morante, "Gas-sensing properties of catalytically modified WO_3 with copper and vanadium for NH_3 detection", *IEEE Sens. J*. **5**, (2005), p. 385-391.

53. A. Stankova, X. Vilanova, E. Llobet, J. Calderer, C. Bittencourt, J.J. Pireaux and X. Correig, "Influence of the annealing and operating temperatures on the gas-sensing properties of rf sputtered WO_3 thin-film sensors", *Sens. Actuator B-Chem*. **105**, (2005), p. 271-277.

54. I. Jimenez, M.A. Centeno, R. Scotti, F. Morazzoni, J. Arbiol, A. Cornet and J.R. Morante, "NH_3 interaction with chromium-doped WO_3 nanocrystalline powders for gas sensing applications", *J. Mater. Chem.* **14,** (2004), p. 2412-2420.

55. P. Ivanov, J. Hubalek, K. Malysz, J. Prasek, X.Vilanova, E. Llobet and X. Correig, "A route toward more selective and less humidity sensitive screen-printed SnO2 and WO3 gas sensitive layers", *Sens. Actuator B-Chem.***100**, (2004), p. 221-227.

56. A.A. Tomchenko, G.P. Harmer, B.T. Marquis and J.W. Allen, "Semiconducting metal oxide sensor array for the selective detection of combustion gases", *Sens. Actuator B-Chem*. **93**, 2003, p. 126-134.

57. J. Wollenstein, J.A. Plaza, C. Cane, Y. Min, H. Bottner and H.L. Tuller, "A novel single chip thin film metal oxide array", *Sens. Actuator B-Chem.* **93**, (2003), p. 350-355.

58. I. Jimenez, M.A. Centeno, R. Scotti, F. Morazzoni, A. Cornet and J.R. Morante, "NH_3 interaction with catalytically modified nano-WO_3 powders for gas sensing applications", *J. Electrochem. Soc.* **150**, (2003), p. H72-H80.

59. B.T. Marquis and J.F.Vetelino, "A semiconducting metal oxide sensor array for the detection of NO_x and NH_3", *Sens. Actuator B-Chem*. **77**, (2002), p. 100-110.

60. X.S. Wang, N. Miura and N. Yamazoe, "Study of WO_3-based sensing materials for NH_3 and NO detection", *Sens. Actuator B-Chem*. **66**, (2000), p. 74-76.

61. C.N. Xu, N. Miura, Y. Ishida, K. Matsuda and N. Yamazoe, "Selective detection of NH_3 over NO in combustion exhausts by using Au and MoO_3 doubly promoted WO_3 element", *Sens. Actuator B-Chem.* **65**, (2000), p. 163-165.

62. E. Llobet, G. Molas, P. Molinas, J. Calderer, X. Vilanova, J. Brezmes, J.E. Sueiras and X. Correig, "Fabrication of highly selective tungsten oxide ammonia sensors", *J. Electrochem. Soc*. **147**, (2000), p. 776-779.

63. M. Ando, T. Tsuchida, S. Suto, T. Suzuki, C. Nakayama, N. Miura and N. Yamazoe, "Ammonia gas sensor using thick film of Au-loaded tungsten trioxide", *J. Ceram. Soc. Jpn*. **104**, (1996), p. 1112-1116.

64. F. Cora, A. Patel, N.M. Harrison, R. Dovesi and C.R.A. Catlow, "An *ab-initio* Hartfree-Fock study of the cubic and tetragonal phases of bulk tungsten trioxide", *J. Am. Chem. Soc.* **118**, (1996), p. 12174-12182.

65. P.M. Woodward, A.W. Sleight and T. Vogt, "Structure refinement of triclinic tungsten trioxide", *J. Phys. Chem. Solids*. **56**, (1995), p. 1305-1315.

66. E. Salje, "The orthorhombic phase of WO_3", *Acta Cryst* **B33**, (1977), p. 574-577.

67. E. Salje and K. Viswanathan, "Physical properties and phase transitions in WO_3", *Acta Cryst*. **A31**, (1975), p. 356-359.

68. R.S. Roth, J.L. Waring, "Phase equilibria as related to crystal structure in the system niobium pentoxide-tungsten trioxide", *J. Res. Nat. Bur. Stand. Sect.* **A70**, (1966), p. 281-303.

69. B. Gerand, G. Nowogrocki, J. Guenot and M. Figlarz, "Structural study of a new hexagonal form of tungsten trioxide", *J. Solid State Chem.* **29**, (1979), p. 429-434.

70. W.L. Kehl, R.G. Hay and D. Wahl, "The structure of tetragonal tungsten trioxide", *J. Appl. Phys.* **23**, (1952), p. 212-215.

71. A.R. Siedle, T.E. Wood, M.L. Brostrom, D.C. Koskenmaki, B. Montez and E. Oldfield, "Solid-state polymerization of molecular metal oxide clusters: Aluminum 12-tungstophosphate", *J. Am. Chem. Soc.* **111**, (1989), p. 1665-1669.

72. L.J. LeGore, R.J. Lad, S.C. Moulzolf, J.F. Vetelino, B.G. Frederick and E.A. Kenik, "Defects and morphologies of tungsten trioxide thin films", *Thin Solid Films* **406**, (2002), p. 79-86.

73. C.V. Ramana, S. Utsunomiya, R.C. Ewing, C.M. Julien and U. Becker, "Electron microscopy investigation of structural transformations in tungsten oxide (WO_3) thin films", *Phys.Stat.Sol.* **202**, (2005), p. R108-R110.

74. Tilley, R.J.D. The crystal chemistry of the higher tungsten oxides. *Int. J. of Refractory Metals & Hard Materials*. **1995**, *13*, 93-109.

75. Slade, R.C.T.; West, B.C.; Hall, G.P. Chemical and electrochemical mixed alkali metal insertion chemistry of the hexagonal tungsten trioxide framework. *Solid State Ionics* **1989**, *32-33*, 154-161.

76. Whittingham, M.S.; Guo, J.D.; Chen, R.; Chirayil, T.; Janauer, G.; Zavalij, P. Hydrothermal synthesis of new oxide materials. *Solid State Ionics*, **1995**, *75*, 257-268.

77. Gouma, P.I.; Prasad, A.K.; Iyer, K.K. Selective nanoprobes for 'signaling gases'. *Nanotechnology* **2006**, *17*, S48-S53.

78. *Agency for toxic substances and disease registry,* USA, www.atsdr.cdc.gov

79. S. Archer, "Measurement of nitric oxide in biological models", *FASEB J* **7**, (1993), p.349-360.

80. J.O.N. Lundberg, E. Weitzberg, J.M. Lundberg and K. Alving, "Nitric oxide in exhaled air", *Eur. Respir J.* **9**, (1996), p. 2671-2680.

81. A.K. Prasad, D. J. Kubinski, P.I. Gouma, "Comparison of sol-gel and ion beam deposited MoO_3 thin film gas sensors for selective ammonia detection", *Sens. Actuators B, Chem.* **93**, (2003), 25-30.

82. N. Guernion, R.J. Ewen, K. Pihlainen, N.M. Ratcliffe, and G.C. Teare, *The fabrication and characterisation of a highly sensitive polypyrrole sensor and its electrical responses to amines of differing basicity at high humidities.* Synthetic Metals, 2002. **126**(2-3): p. 301-310.

83. Kearney, D. J., Hubbard, T., and Putnam, D. Breath ammonia measurement in Helicobacter pylori infection. Dig Dis Sci, *47:* 2523-2530, 2002.

84. A.L. Linsebigler, G. Lu, J.T. Yates Jr. *Chem. ReV*. **95,** (1995), 735.

85. P.I. Gouma, M.J. Mills, "Anatase to rutile transformation in titania powders", *J. Am. Ceram. Soc.* **84**, (2001), 619-622.

86. P.I. Gouma, M.J. Mills, K.H. Sandhage, "Fabrication of free-standing titania-based gas sensors by the oxidation of metallic titanium foils", *J. Am. Ceram. Soc*. **83** (2000), 1007–1009.

87. S.A. Akbar, L.B. Younkman, “Sensing mechanism of a carbon monoxidesensor based on anatase titania”, *J. Electrochem. Soc.* **144** (1997) 1750–1753.

88. L.A. Harris, “A titanium-dioxide hydrogen detector”, *J. Electrochem. Soc.* **127** (1980), 2657–2662

89. N. Savage, B. Chwieroth, A. Ginwalla, B.R. Patton, S.A. Akbar, P.K. Dutta, “Composite n–p semiconducting titanium oxides as gas sensors”, *Sens. Actuators B, Chem.* **79** (2001) 17–27.

90. E. Comini, G. Sberveglieri, M. Ferroni, V. Guidi, G. Martinelli, “Response to ethanol of thin films based on Mo and Ti oxides deposited by sputtering”, *Sens. Actuators B, Chem.* **93** (2003) 409–415.

CHAPTER 2

EXPERIMENTAL

2.1 Material synthesis

2.1.1 Sol-Gel Method

Sol-gel synthesis is a popular and inexpensive method used for producing 3-d networks of nanoparticles. Sol-gel processing is the process of preparing a sol, gelation of a sol, and removal of the solvent [1]. A sol may be defined as a colloidal suspension of solid particles in a liquid. Usually the particle size is in the range of 1-1000nm. A gel is a substance that contains a continuous solid phase enclosing a continuous liquid phase. The continuity of the solid phase gives elasticity to the gel.

The starting materials used in the preparation of a sol are usually inorganic metal salts or metal organic compounds such as metal alkoxides. The sol obtained can be processed in different ways depending on the final application requirements and the versatility of the process lies in the flexibility available for obtaining the desired end product. For instance, the sol can be spin coated and dried to give thin films. The sol instead may be allowed to gel, and the liquid phase in the gel may be removed by supercritical drying, leaving behind a highly porous and low density network of metal oxide particles called the ‘aerogel’. Instead of extracting the solvent, if the solvent is evaporated, a product known as ‘xerogel’ results [2].

Metal alkoxides have a ligand attached to the metal/metalloid atom and they react readily with water as follows:

$$M(OR)_z + H_2O \rightarrow HO\text{-}M(OR)_{z-1} + ROH \quad (1)$$

Where R is the alkyl group,

z is dependant on valency of metal M.

In the preparation of tungsten oxides, an alkoxide reaction with alcohol is used to adjust the rate of gelation due to alcohol interchange as follows.

Tungsten (VI) Isopropoxide + 1-Butanol → Precursor (0.1M) (2)

2.1.2 Spray Pyrolysis:

TiO_2 nanoparticles were produced in a flame spray pyrolysis (FSP) reactor described in detail elsewhere [3-4]. Precursor solutions (0.5 or 0.67 M) were prepared from titanium-tetraisopropoxide (TTIP, Aldrich, purity > 97%) diluted in an 11:5 (v/v) mixture of xylene (Fluka, >98.5%) and acetonitrile (Fluka, >99.5%) and fed at 5 ml/min through the inner reactor capillary. Through the surrounding annulus, 5 l/min of oxygen (Pan Gas, purity > 99%) were fed dispersing the precursor solution into a combustible spray. The pressure drop at the nozzle tip was maintained at 1.5 bar. The methane and oxygen flow rates in the FSP-supporting premixed flame [4] were 1.5 and 3.2 l/min, respectively. The spray flame could be sheathed with 40 l/min of oxygen gas and enclosed by a 40 cm long glass tube resulting in higher temperatures.

2.1.3 Electrospinning

Electrospinning was patented by Formhals in 1934 primarily for textile weaving [5]. The electrospinning setup consists of a syringe pump, a needle, a grounded collector and a high voltage power supply. The precursor solution to be spun is filled in to the

syringe pump and a high potential is applied to the tip of the needle as shown in the figure. The liquid droplet is first drawn out into the shape of a cone, the droplet being held together by the surface tension forces. If the viscosity is not high enough then the droplet is sprayed on to the collector. On the other hand if the viscosity is just right, then the droplet is whipped in to a continuous jet of fibers towards the collector, where they form a mat. There are several process parameters that play a critical role in the process and they are tabulated below.

The protocol for electrospinning metal oxide nanowires is as follows. A sol-gel of the metal oxide that is to be spun is prepared as explained in section 3.1. The precursor polymer, in this case PVP (Polyvinylpyrrolidone- MW 1,300,000;Sigma-Aldrich, Milwaukee, WI)), a high molecular weight polymer, is dissolved in ethanol to form a 0.1mM solution and is mixed with the sol-gel in 4:1 ratio. The solutions were electrospun in air using a DC voltage power supply (Model ES 30P-6W; Gamma High Voltage Research, Ormond Beach, FL) at 20 kV, a programmable syringe pump (model 200; KD Scientific, Holliston, MA) operated at a flow rate of 20 l /min, and an aluminum collector plate. The needle-to-collector distance was approximately 100 mm. Calcination of the MoO_3/polymer hybrid matrix was carried out from room temperature to 500 °C for 2 h and then stabilized at 500 °C for 8 h with a cool down cycle of 2 h. Differential scanning calorimetry studies carried out previously (Ref. 25) show that the stable polymorph of MoO_3 appears above 480 °C. Thus, the samples are heat treated to 500 °C for 8 h to ensure phase stability.

2.2 Sensor Processing

Thin films of WO_3 were prepared by spin coating and drop coating the prepared sol on to sensing substrates. The sensing substrates (3mm x 3mm) were made of Al_2O_3 and were patterned with interdigitated Pt electrodes. Substrate heating was achieved by Pt heater electrodes embedded on the rear of the sensor. A schematic of the sensor substrates used is given in fig 2.1.

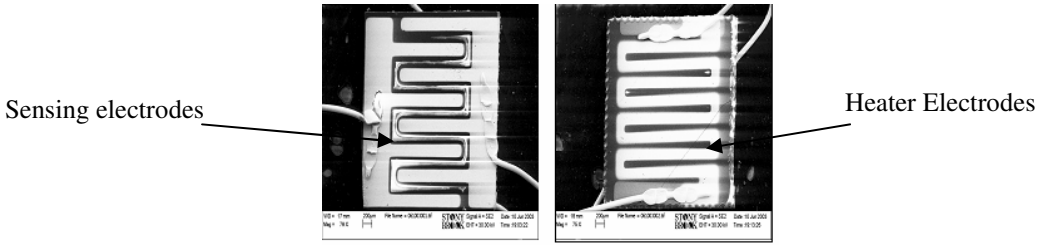

Figure 2.1: Schematic of the sensing and heating electrodes

Subsequent to thin film deposition, the films are amorphous and have to be calcined at higher temperatures to achieve the desired polymorphic form. (In this case differential scanning calorimetry (DSC) was carried out to assess the phase transformation temperatures). Based on the results of DSC, the sensors were heat treated at 400°C for 6 hrs and 515°C for 8hrs.

2.3 Materials Characterization

2.3.1 Differential Scanning Calorimetry (DSC)/ Thermogravimetric Analysis (TGA)

In order to characterize the phase transformation regimes of the metal oxide precusors DSC/TGA were performed using a Netzsch STA449C in the temperature range between ambient and 700°C for WO_3 and ambient and 500°C for MoO_3 precursors. The heating rate used was 2°C/min and the background gas was N_2.

2.3.2 X –Ray Diffraction Analysis

Philips X-Ray Diffractometer PW 1729 was used to characterize the films deposited on sensor substrates and to confirm the phases present in the stabilized sensors. The diffractometer operates at 40kV and 30mA. X-rays are irradiated over an area of 2×1.5 cm^2 region and has a 2θ range from 20º to 80º. The Philips computer generates a file of 2θ versus I from which d values can be calculated from the relation

$$d = \lambda / (2 \sin \theta) \qquad (3)$$

where λ is the wavelength of Cu Kα radiation which is 1.54184 Å. The d values are then compared with standard JCPDS powder diffraction data for the material under test and possible phases are identified.

2.3.3 Transmission Electron Microscopy

In order to determine the grain sizes and the phases present in the films deposited by sol-gel processes, TEM characterization was performed. The transmission electron microscope used for this purpose is the Philips CM12 with LaB_6 cathode. The incident energy of electrons under which this was carried out is 120 keV.

The heat treated metal oxides from the sensor substrate were collected and made in to a suspension in ethanol. The suspension was then ultrasonically agitated for about an hour to break up any aggregates. After agitation, the suspension was dropped on to formvar coated copper TEM grids. The grid was allowed to dry well, before observation in the electron microscope.

2.3.3.1 High resolution transmission electron microscopy (HRTEM)

In order to characterize defect structures in tungsten trioxide HRTEM was performed on a JEOL4000EX microscope at the Center for Functional Nanomaterials in Brookhaven National Lab at an accelerating voltage of 400kV. Samples were prepared the same way as were done for low resolution electron microscopy.

2.3.4 Raman Spectroscopy

The Raman spectra were collected on a Brucker FRA106, equipped with a neodymium:yttrium aluminium garnet (Nd:YAG) laser that is frequency doubled to 532 nm. The spectra were recorded in the air atmosphere at room temperature using the laser power of 20mW.

2.3.5 Photo Luminescence Measurements (PL):

Photo luminescence measurements were carried out using a He-Cd LASER with an excitement wavelength of λ=325 nm (10 mW) on an RPM-2000 spectrometer (Accent Optical Technologies, OR, USA), in order to assess the luminescence properties and defect structure of the WO_3 polymorphs. The measurements were carried out at room temperature.

2.3.6. X-ray Photo Electron Spectroscopy (XPS):

XPS measurements were carried out at the ESCA facility operated by the Laboratory for Surface Modification at Rutgers University, using a Kratos XSAM 800 spectrometer using unmonochromatized AlKα radiation, and a hemispherical electron energy analyzer equipped with a multichannel detection system. The samples were annealed at 100°C to eliminate the influence from the background and the measurements were carried out at room temperature.

2.4 Sensor Characterization

Sensing experiments were carried out in a modified electronic olfactory system EOS 835 (SACMI IMOLA, Italy). The sensing chamber in EOS 835 can accommodate up to six 3mm x 3mm sensors at the same time. It is a commercial device that comes along with six SnO_2 based sensors that are non-selective. These have been replaced with selective WO_3 based sensors.

The sensing chamber is made of stainless steel to avoid adsorption/desorption of gases while sensing. The olfactory system has a small pump inside that controls the inlet

gas flow. Gas flow was controlled externally by a series of mass flow controllers (MKS 1479A), and the flow was manipulated so that it would match the modified internal flow of EOS 835. A schematic of the sensor on a TO8 substrate, the sensing chamber of EOS 385 and the gas sensing set up are given in fig 2.2 and 2.3.

The gases that were used and their concentrations are given in Table VI. UHP N_2 and UHP O_2 were used in the ratio of 80-20 as the background carrier gas.

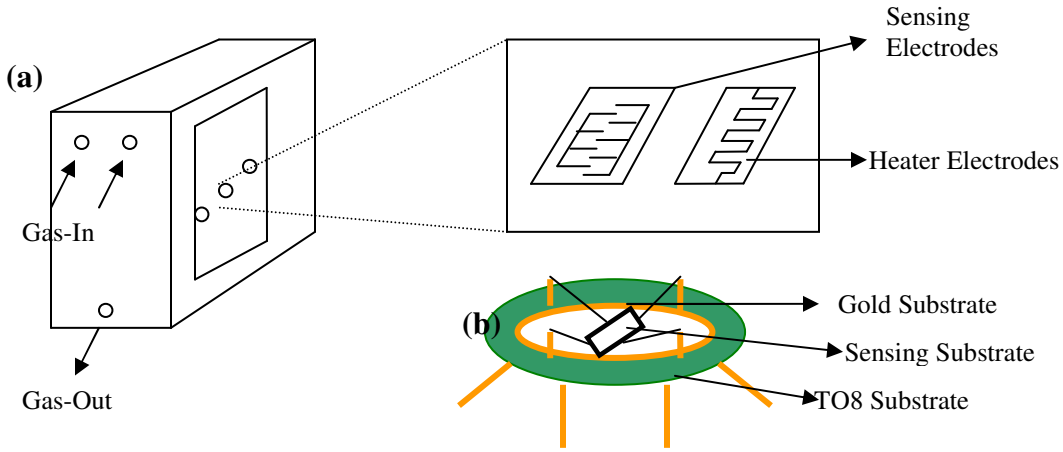

Figure 2.2: (a) Schematic of EOS 835 and the sensing chamber; (b) Schematic of the sensing substrate on the TO8 substrate

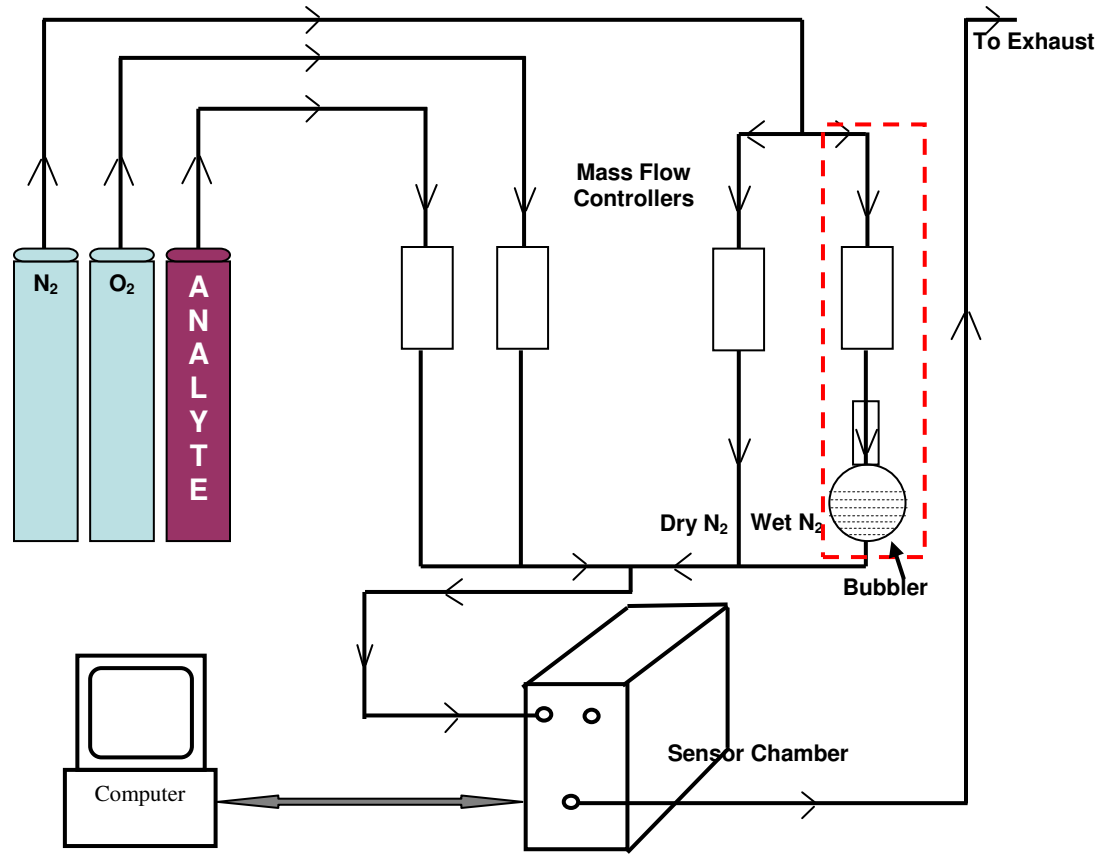

Figure 2.3: Schematic of the gas sensing setup

Table 2.1: Concentrations of gases used for sensing

Gas	NO	NO_2	Isoprene	Ethanol	Acetone	Methanol
Concentration	300ppb-10ppm	300ppb-300ppm	10ppm	300ppb-100ppm	300ppb-10ppm	10ppm

References:

1. C.J. Brinker and G.W. Scherer, *Sol-Gel Science: The Physics and Chemistry of Sol-Gel Processing*. 1990, San Diego: Academic Press, Inc.
2. CHEMAT technology Inc. USA, www.chemat.com
3. L. Madler, W.J. Stark, S.E. Pratsinis, "Simultaneous deposition of Au nanoparticles during flame synthesis of TiO_2 and SiO_2", *J. Mater. Res.* **18** (2003), 115–120.
4. H. Schulz, L. Madler, R. Strobel, R. Jossen, S.E. Pratsinis, T. Johannessen, "Independent control of metal cluster and ceramic particle characteristics during one-step synthesis of Pt/TiO2", *J. Mater. Res.* **20** (2005), 2568–2577.
5. A. Formhals: U.S. Patent No. 1,975,504 (1934).

CHAPTER 3

WO_3 Polymorphic Sensors

This chapter focuses on the gas sensing behavior of the two polymorphs of WO_3 that are isostructural – orthorhombic and monoclinic. DSC, XRD, TEM, HRTEM, XPS have been carried out to assess the gas sensing nature.

3.1 Structural Characterization:

3.1.1 Differential Scanning Calorimetry

Figure 3.1 shows the weight loss vs temperature graph for as received sol-gel sample of tungsten trioxide.

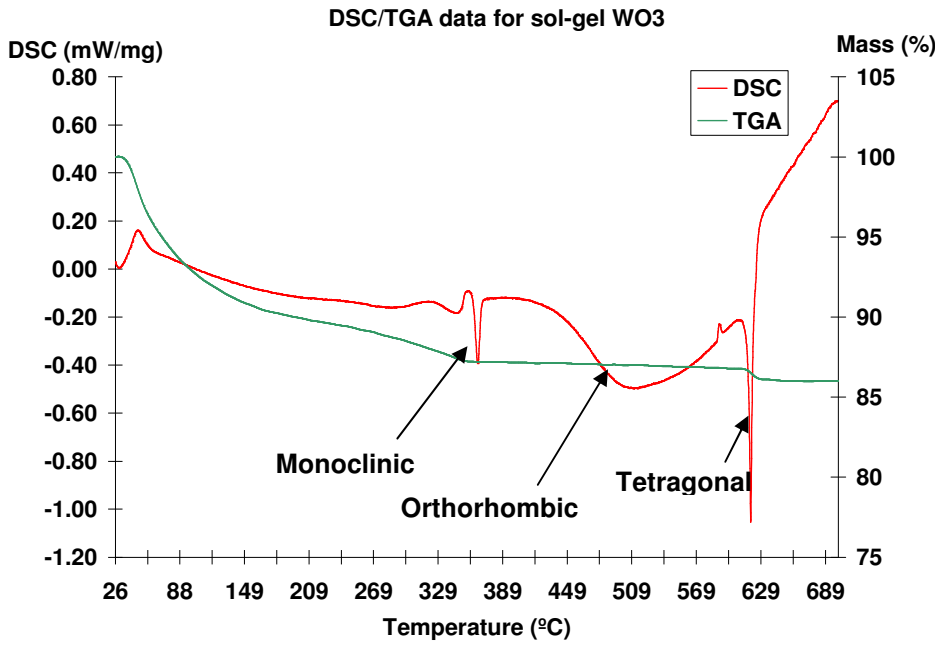

Figure 3.1: DSC data for sol-gel WO_3

The graph shows three distinct weight loss regions. The one at around 320-350°C corresponds to the monoclinic transformation as shown in table 1.3 in chapter 1. The second phase transformation corresponding to the monoclinic-orthorhombic transition occurs over a broad range of temperatures as can be seen from the slope of the curve from 350-500°C but is complete at around 500°C. The third and the final polymorphic transformation leading to the crystal structure with the highest symmetry occurs at around 630°C corresponding to the tetragonal phase.

This serves as the basis for choosing the heat treatment temperatures for the sol-gel samples in order to obtain the desired phase in the sensing matrix.

3.1.2 X-ray Diffraction:

Figures 3.2 and 3.3 illustrate the x-ray diffraction profiles of the sol-gel WO_3 heat treated at 515°C and 400°C. In both the spectra the most prominent higher order peaks are indexed. The main peaks in the sample heat treated at 515°C can be indexed to the JCPDS card number 20-1324 [1] while the sample heat treated at 400°Cis monoclinic and be indexed to the JCPDS card number 36-0102 [2]

These results are consistent with the DSC data as explained in the previous section where the monoclinic phase is stable up to a temperature of 400°C and transforms to the orthorhombic phases on heating to 515°C.

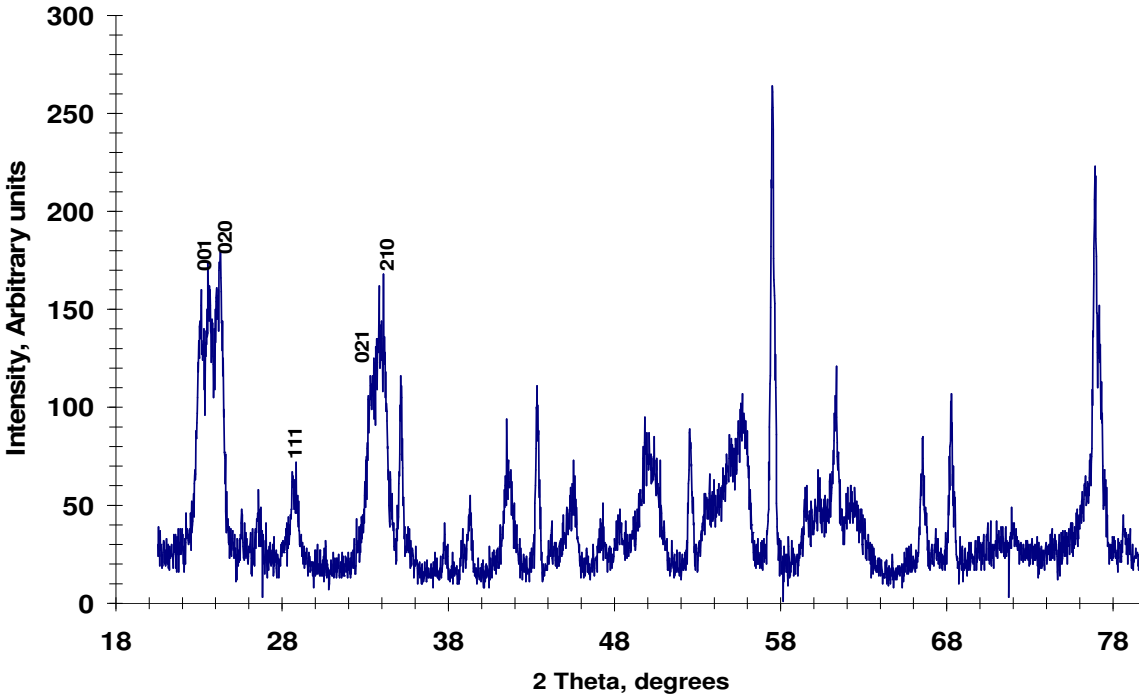

Figure 3.2: X-ray diffraction profile of WO_3 sol-gel precursor annealed at 515°C

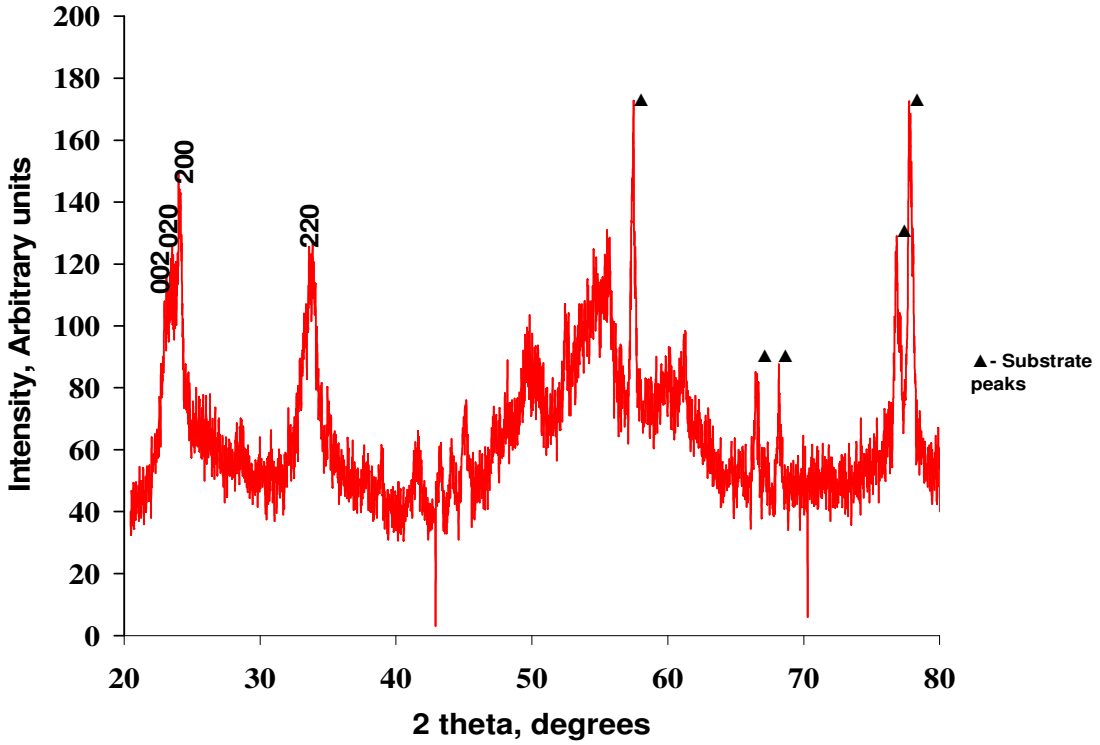

Figure 3.3: X-ray diffraction profile of WO_3 sol-gel precursor heat treated at 400°C

3.1.3 Transmission Electron Microscopy:

TEM analysis was carried out for both the samples for analyzing both the grain size and crystallographic orientation. Figures 3.4 and 3.5 illustrate the low magnification TEM image and selected area diffraction pattern of the WO_3 sample heat treated at 515°C. The ring diameters, the interplanar spacings and the *(hkl)* denominations are given in table 3.1.

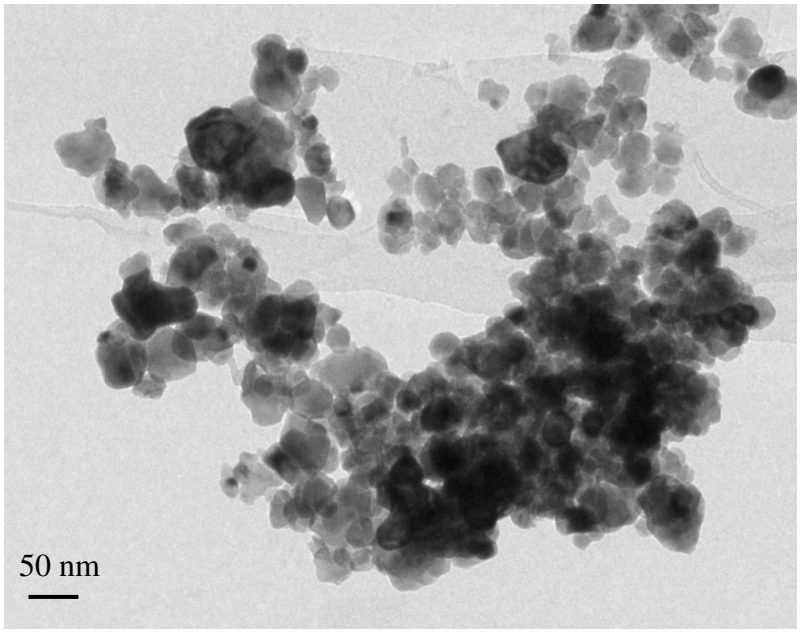

Figure 3.4: General TEM view of the 515°C annealed sample

As can be inferred from figure 3.4 the grain size ranges from 10-50nm. The agglomeration of the particles is quite typical of sol-gel samples. It can also be seen that the particles form a three-dimensional network, with interconnected porosity. This is again another unique feature of samples prepared by the sol-gel route.

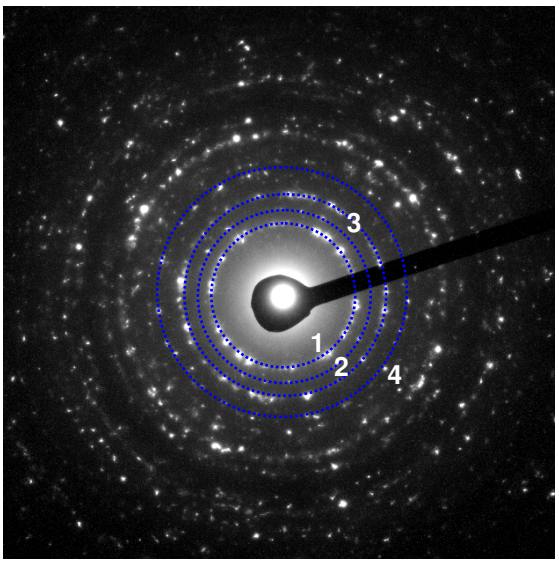

Figure 3.5: SAED pattern corresponding to WO_3 sample heat treated at 515°C.

Table 3.1: SAED pattern indexation corresponding to that shown in figure 3.5

# Ring	Spacing	Phase	Planes
1	3.74	WO_3	020
2	3.2	WO_3	111
3	2.63	WO_3	220
4	2.173	WO_3	221

The interplanar spacings and the planes indexes correspond to those of orthorhombic WO_3 (JCPDS card number 20-1324) as shown in figure 3.1. Although not observed in the low magnification TEM image, the sample annealed at 515°C possesses many crystalline stacking defects known as 'crystallographic shear plane' or 'Magneli' phases. These are planes of oxygen deficient WO_6 octahedra and are visible only under high resolution transmission electron microscopy. The following section discusses about

the HRTEM experiments on the samples heat treated at 515°C in order to characterize the bulk defects that play an important role in altering the electrical properties of the sensor.

The sample annealed at 400°C is highly nanocrystalline (as evidenced by the peak broadening in the XRD spectrum in figure 3.2) and hence the SAD rings are broadened as seen in figure 3.6.

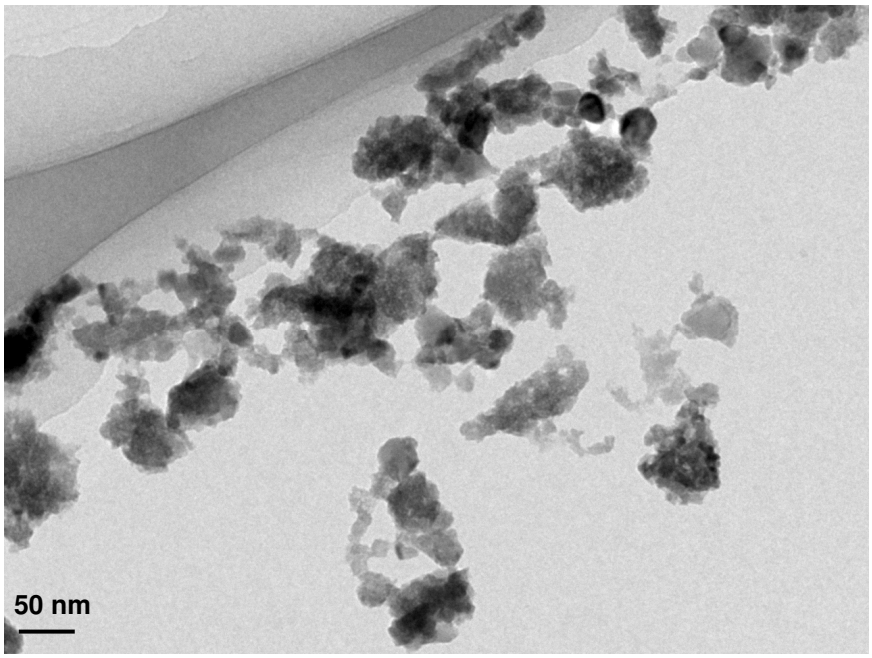

Figure 3.6: General TEM view of the 400°C annealed sample

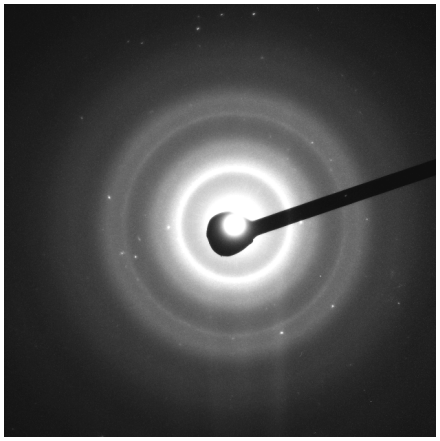

Figure 3.7: SAED pattern corresponding to the sample heat treated at 400°C

The average grain size is around 10-20 nm which is smaller compared to the sample heat treated at 515°C, which is to be expected because the higher temperature annealing leads to some grain growth as well.

3.1.4 High Resolution Transmission Electron Microscopy:

It has been previously found that there exist sub-stoichiometric i.e., oxygen-deficient regions in MoO_3 called the Magneli phases. These are ordered planar defects formed by the removal of anions from the transition metal oxide. These consist of slabs of perfect ReO_3 type structure joined together along planes of discontinuity called "Crystallographic Shear" (CS) planes. Thus in a normal cubic ReO_3 structure the MoO_6 octahedra are linked by shared corners. In these non-stoichiometric regions the ReO_3 block type structures are joined along shear planes where groups of four octahedra share edges [3]. These bulk defects affect the electrical transport properties such as carrier concentration and carrier mobility [4]. :

Similarly in WO_3 it is possible to shear the structure in such a way that the oxygen vacancies are eliminated. This results in the formation of CS planes along which the WO_6 octahedra share edges instead of corners as shown in figure 3.8. Tungsten atoms are more closely spaced along these planes and the charge changes to W^{5+} in order to compensate for the charge left behind by the oxygen vacancies.

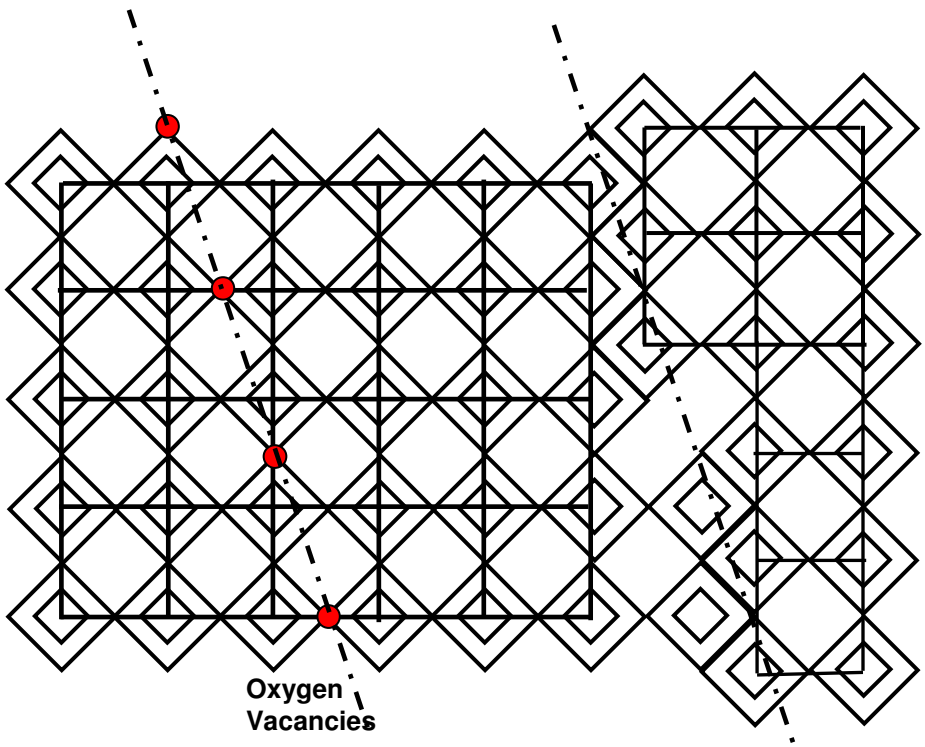

Figure 3.8: Crystallographic shear planes in WO_3

Such CS planes were found in the orthorhombic polymorph as compared to the monoclinic polymorph. Though the material is not non-stoichiometric there are localized regions where the crystal is non-stoichiomteric.

Figure 3.9 shows a high resolution transmission electron micrograph of a single orthorhombic nanocrystal with the CS planes outlined. Figure 3.10 and 3.11 are the inverse fast Fourier transform images of the CS planes showing the increased plane spacing. These planes usually occur along the $\{1\ 0\ \mathrm{k}\}_R$ directions.

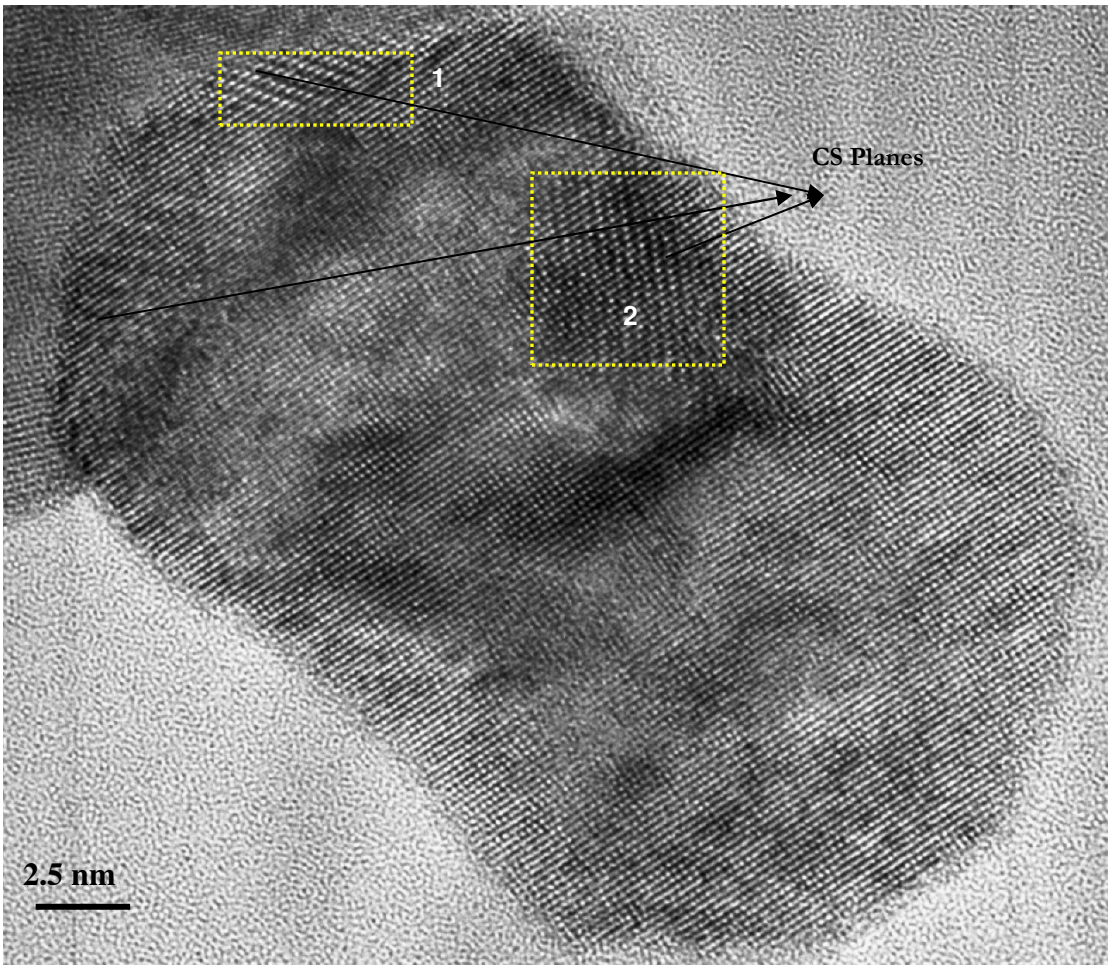

Figure 3.9: High resolution transmission electron microscopy image of a single grain in the sample heat treated at 515°C

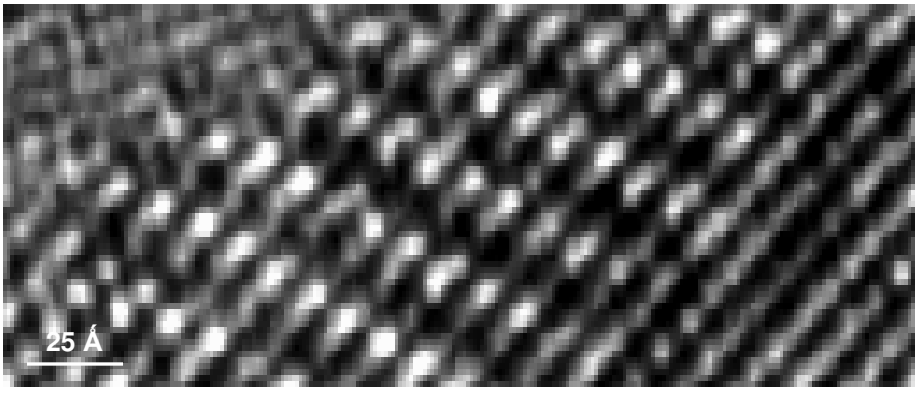

Figure 3.10: IFFT of region 1 outlined in figure 3.8

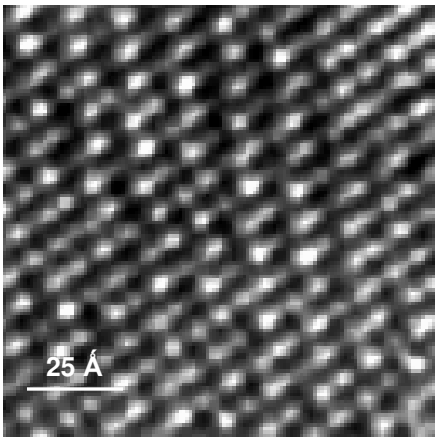

Figure 3.11: IFFT of region 2 outlined in figure 3.8

3.1.5 Raman Spectroscopy:

Figure 3.12 shows the Raman spectra of the WO_3 thin films annealed at 400 and 515°C. It can be seen that the annealed samples present the typical structure of crystalline WO_3 with three main regions at 900-600, 400-200 and below 200 cm^{-1}.

These belong to the stretching, bending and lattice modes of the crystal structure [5-8]. The monoclinic to orthorhombic phase transitions can be observed only at very low wave numbers [9]. The higher wave numbers are the same for both the monoclinic and orthorhombic phases. This study was limited by the capabilities of the instrument for measuring the spectra in the lower wave number regime. Table 3.2 lists the observed vibrations and the vibration modes for both the samples.

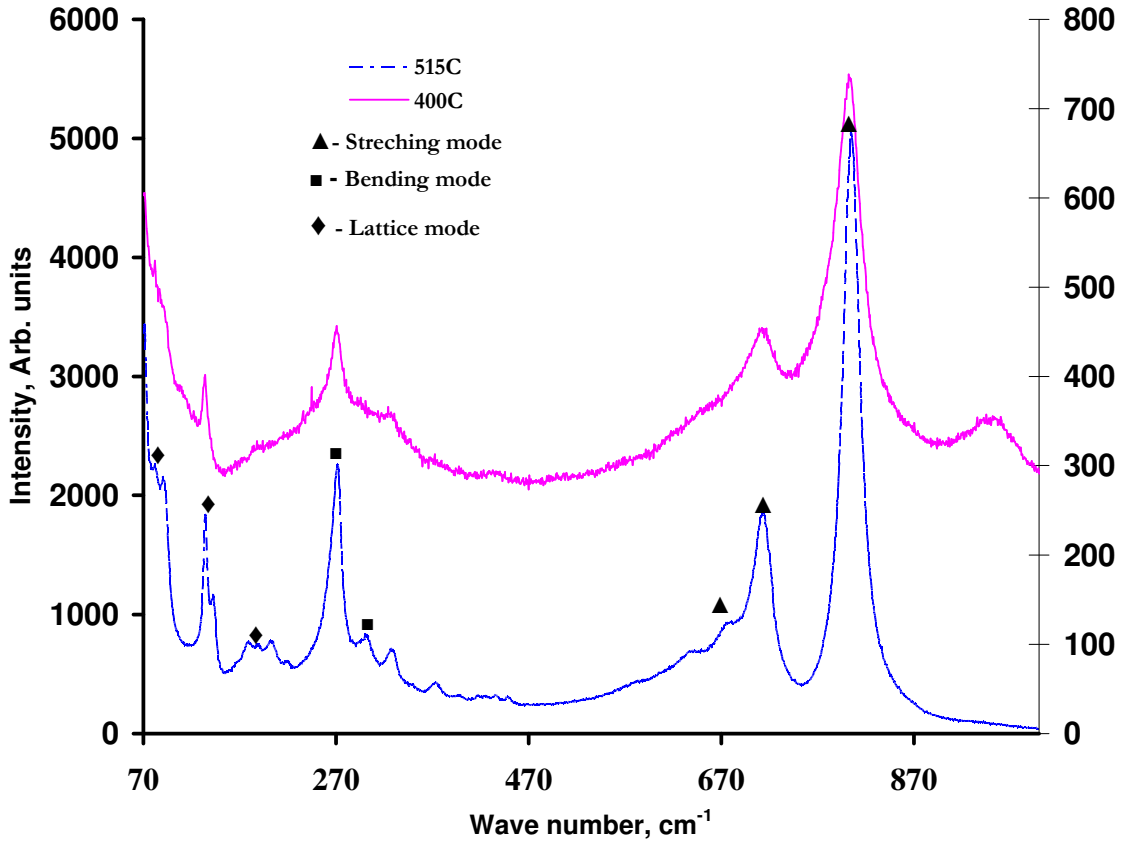

Figure 3.12: Raman spectra of the WO_3 films annealed at 400 and 515°C.

Table 3.2: Raman vibration modes found in the WO_3 samples annealed at 400 and 515°C

WO_3-400°C	WO_3-515°C	Vibration Mode
954	-	ν (W=O)
804 716 440	809 713 680 642 452	ν (O-W-O)

	440 421 403	
328	376 329	δ (O-W-O)
298 272 239	222	ν (W-O-W)
191 134	182 142 134 92 82	Lattice Modes

There is also a small shoulder at 954cm^{-1} which is attributed to W=O, stretching [5,8]. As the XRD did not reveal any hydrates in the sample, this can be attributed to surface moisture. It is known from the literature that peak broadening in Raman spectra occurs due to reduction in grain size. Peak broadening occurs due to three dimensional phonon confinements when crystallite sizes become nanocrystalline [10-11]. Similar effects due to phonon confinement have been observed in nanowires of Si [10] and naocrystals of rutile TiO_2 [11].

3.1.6 Photoluminescence measurements

Figure 3.13 shows the photoluminescence (PL) emission spectra of the two WO_3 polymorphs. Both of them show a broad emission peak centered around 750nm with a sharp but smaller peak at 680nm.

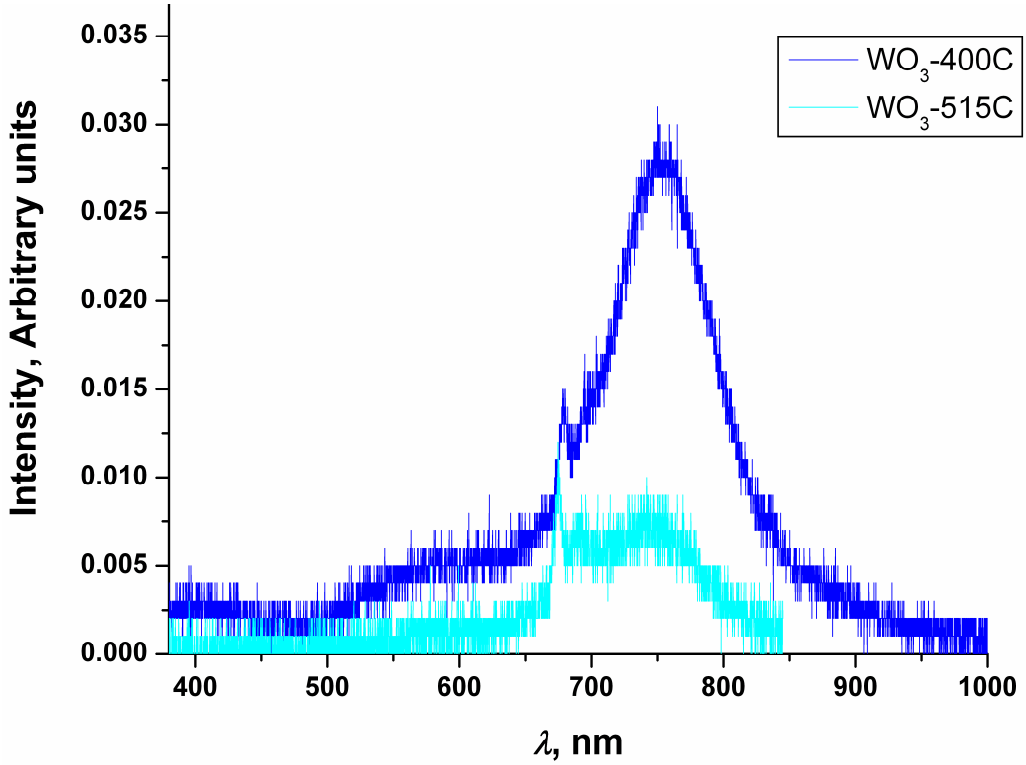

Figure 3.13: PL spectra of the WO_3 polymorphs.

All the literature on photoluminescence in WO_3 talks about near band edge emission. As can be inferred from the graph no higher energy near-band gap emissions were observed in either sample. Instead both the polymorphs show a deep, low energy broad emission peak. It is known that such peaks are indicative of the presence of surface states/traps in the material that reduce the intensity of emission. From the peak intensities

it is clear that the orthorhombic polymorph has a higher density of surface states as compared to the monoclinic polymorph.

3.1.7 X-ray Photoelectron Spectroscopy:

Figures 3.14 to 3.16 represent the x-ray photoelectron spectra of the WO_3 polymorphs. The sample denoted B1 is orthorhombic WO_3 while the sample denoted A1 is monoclinic.

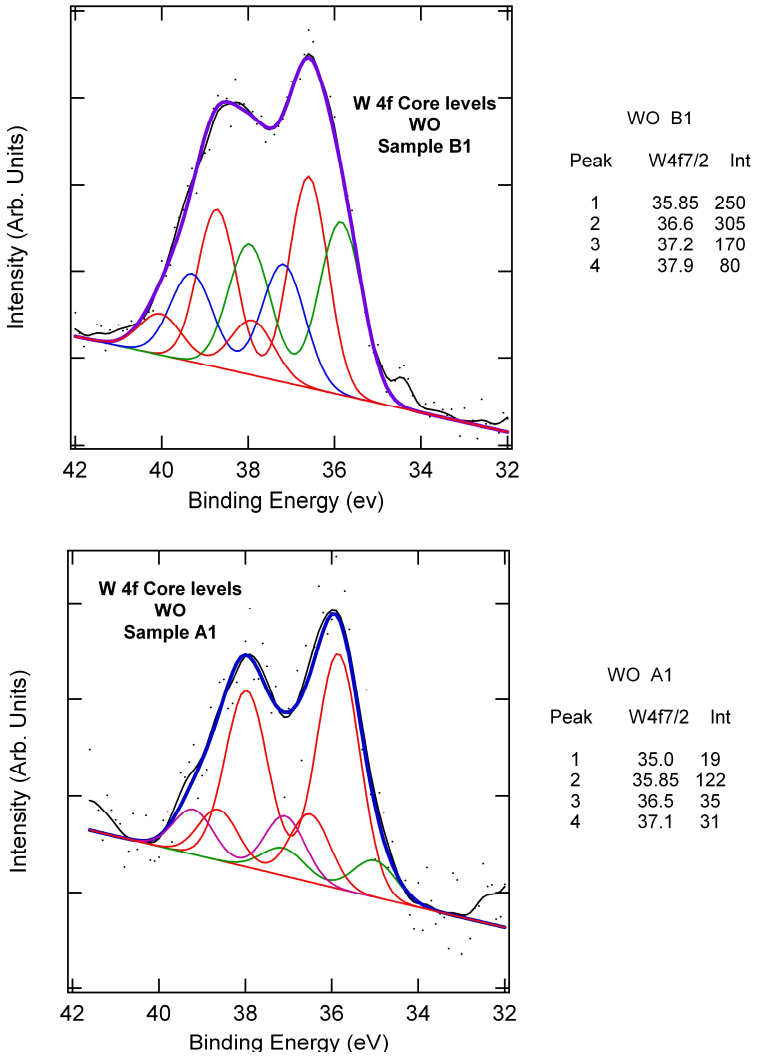

Figure 3.14: W4f core level spectra of the orthorhombic (B1) and monoclinic (A1) polymorph

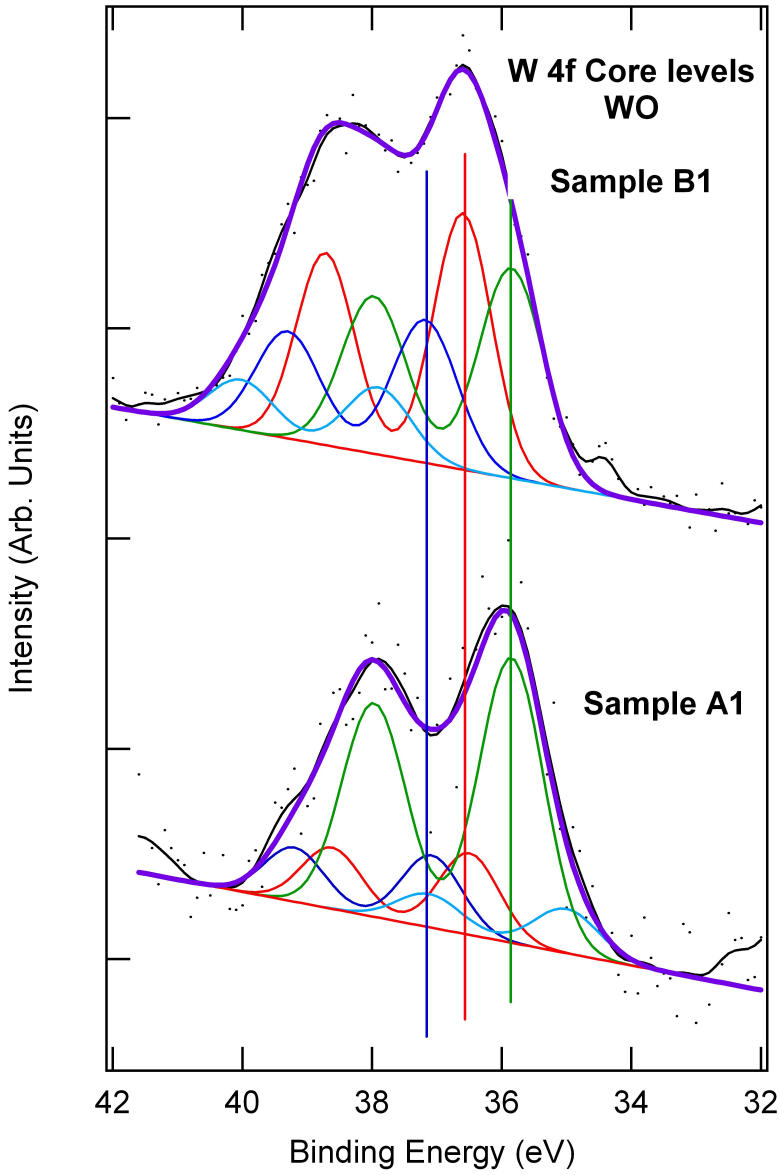

Figure 3.15: W4f core level resolved spectra of the orthorhombic (B1) and monoclinic (A1) polymorph

The line shapes from both samples are well described by four identical line shapes accounting for the W $4f_{7/2}$ and $4f_{5/2}$ doublet, shifted by different amounts. The energies of the W $4f_{7/2}$ feature are given in the tables in the figure. The $4f_{5/2}$ was assumed to be at

2.12 eV higher binding energy (spin-orbit splitting from literature), and the 7/2:5/2 ratio was taken to be the statistical ratio 8:6 (that is, 2j+1). All peaks are Gaussian of 1 eV width.

The lines from both samples are fit by 4 peaks. Three of the features appear to be common (to within 0.1 eV) for both samples. These are at 35.85, 36.5, and 37.1 eV. The A sample has an additional line at 35 eV and the B sample has a line at 37.9 eV. The literature value for the W $4f_{7/2}$ level of single crystal WO_3 (that is, W^{+6} oxidation state) is 36.0 eV [12-14]. Values quoted for W^{+5} are in the 33 - 34 eV range. Therefore, it appears that both samples are in a WO_3 phase, but there are inhomogeneities that give rise to different peak energies. Clearly the A-sample is "cleaner" in the sense that it is dominated by the ~ 36 eV peak. The other contributions may be from regions near the surface of the particles, or from the possibility that particles of different sizes have different local structures.

The VB line shapes are consistent with WO_3 data in the literature. One important thing to notice, however, is that the two samples have a slightly different shape at the Fermi energy (Binding Energy = 0). This indicates that there are more defects in the orthorhombic sample that leads to these states in the band gap. For the monoclinic sample the intensity appears to go to zero at about BE = 0.25 eV which is similar to what is found in the literature.

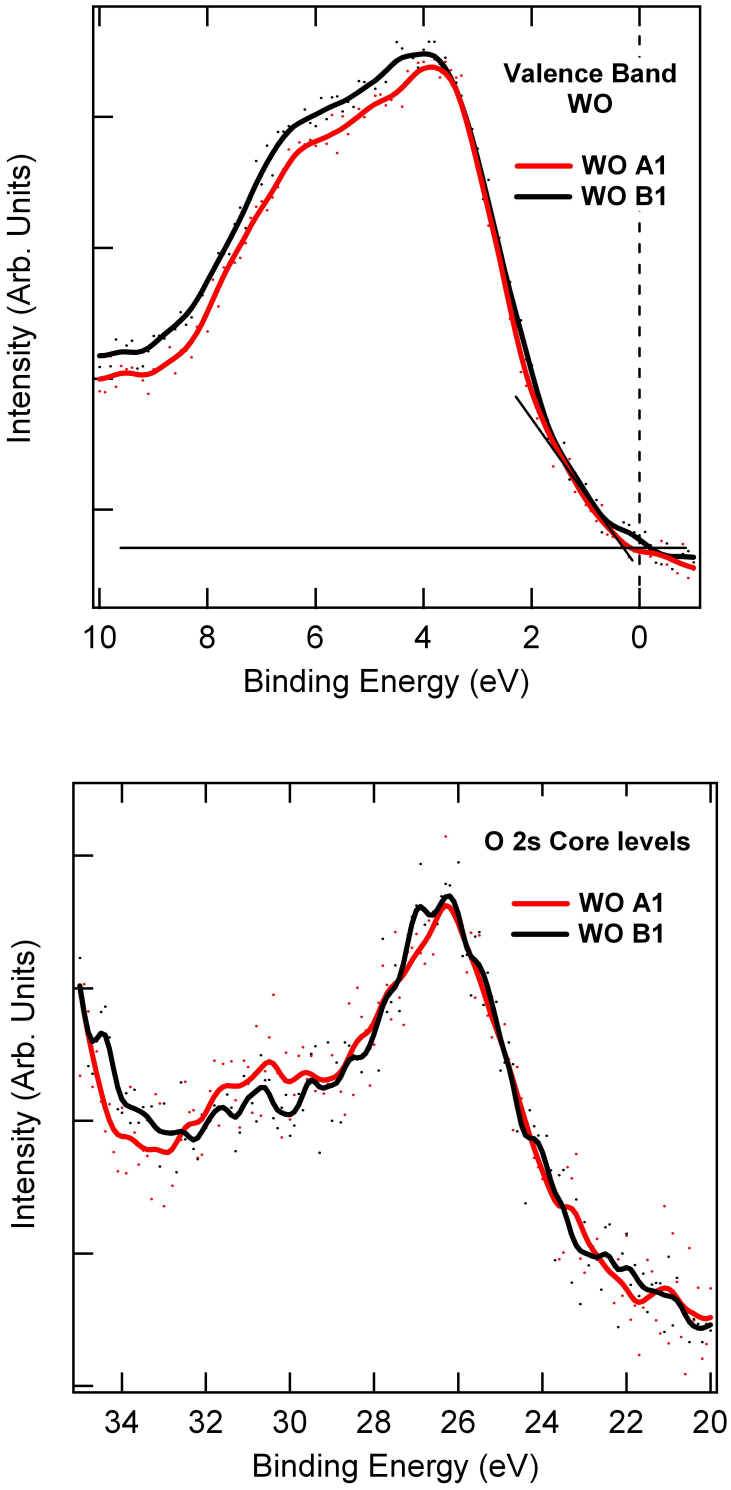

Figure 3.16: Valence band and O 2s core level spectra of the monoclinic (A1) and the orthorhombic (B1) sample

3.2 Sensor Characterization:

3.2.1 Monoclinic and Orthorhombic WO_3 sensors:

Figure 3.17 shows the dynamic gas sensing response of the monoclinic polymorph to different gases namely NO_2, NO, acetone, ethanol and methanol at 400°C.

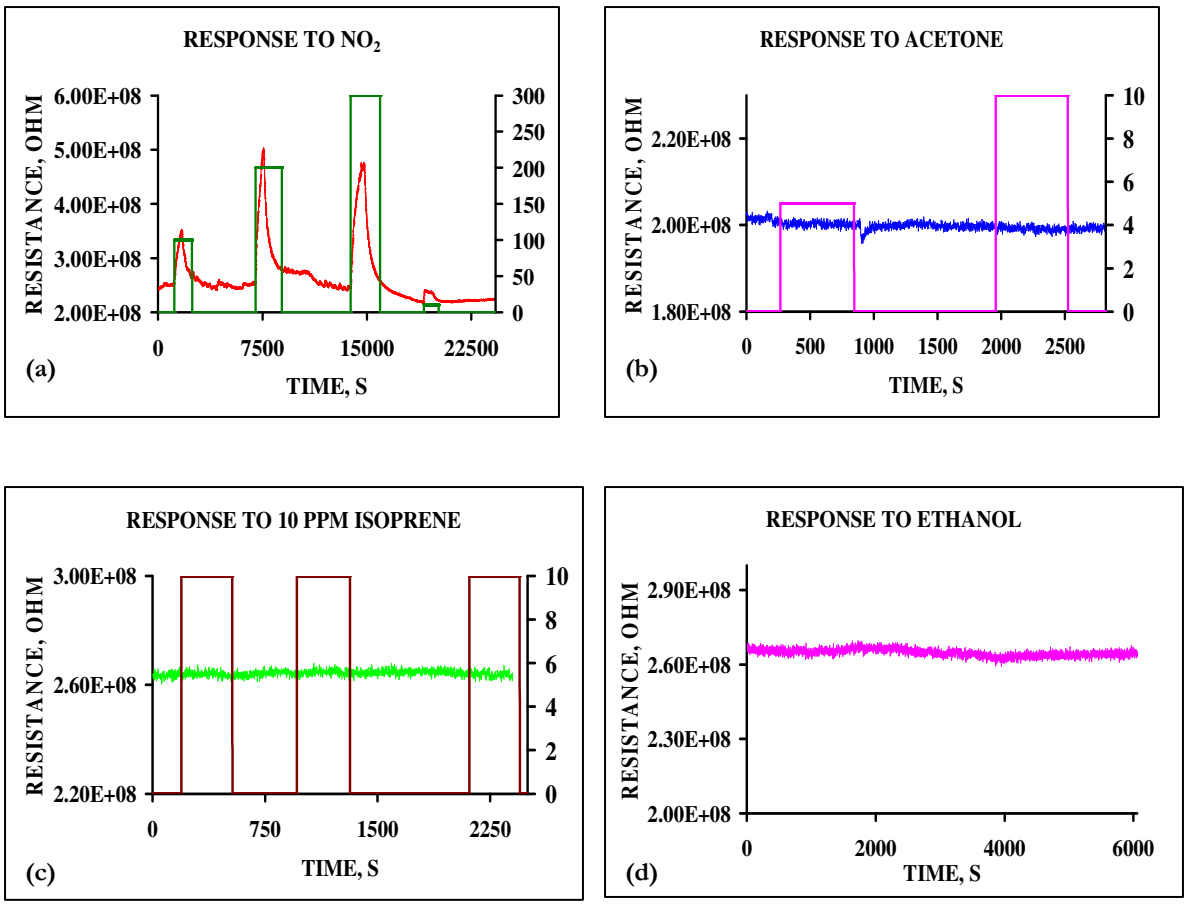

Figure 3.17: Response of the monoclinic sensor to (a) 10-200 ppm of NO_2 (b) 5-10 ppm acetone; (c) 5-10 ppm isoprene; (d) 50 ppm ethanol

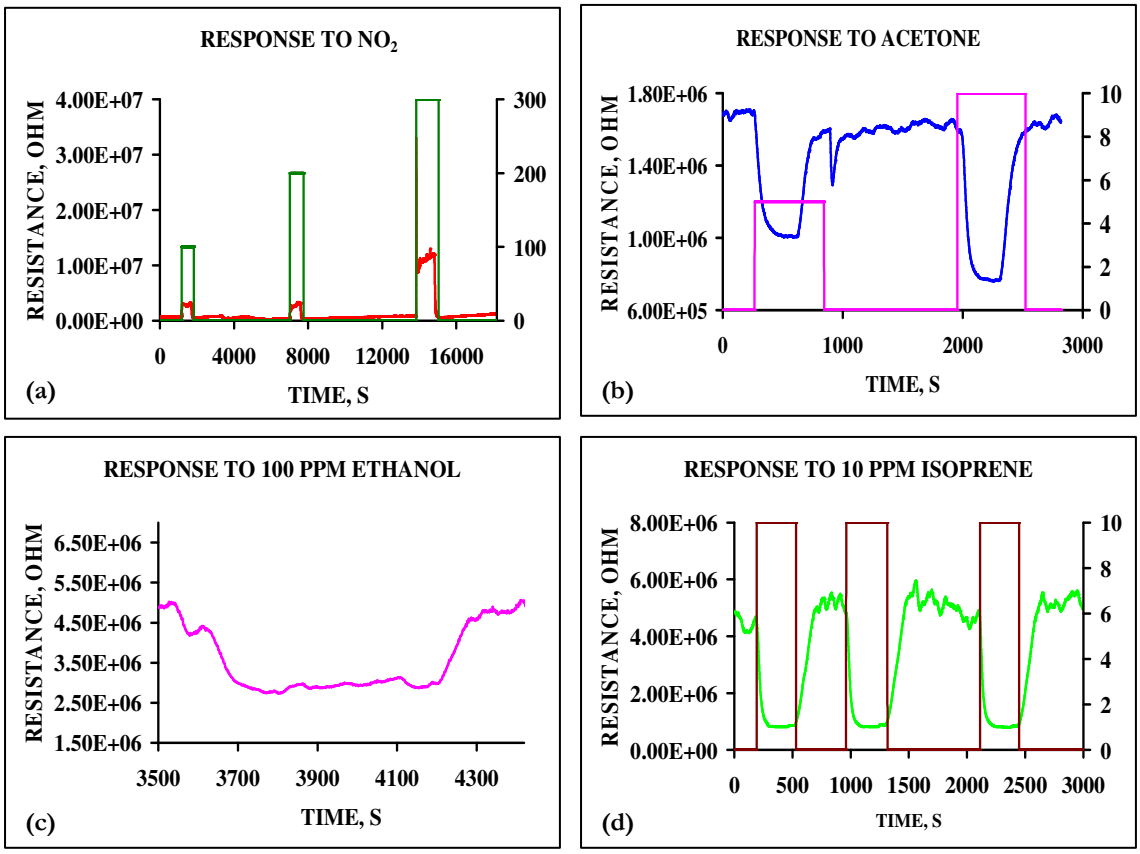

Figure 3.18: Response of the orthorhombic sensor to (a) 10-200 ppm of NO_2 (b) 5-10 ppm acetone; (c) 50 ppm ethanol; (d) 5-10 ppm isoprene

Figures 3.17 to 3.18 show the sensing response of the monoclinic and orthorhombic sensors to oxidizing and reducing analytes at varying concentrations. The sensing temperature for the monoclinic sensor was 400°C and the orthorhombic sensor in this experiment was 500°C.

The sensitivity ($S=R_g/R_a$) of the monoclinic polymorph to NO_2 at 200 ppm the highest concentration 2.0 while the cross-sensitivity to reducing gases is zero. The orthorhombic polymorph on the other hand has a sensitivity of 8.5 for a concentration of

200 ppm, while its sensitivity towards 10 ppm of acetone is 0.6, 10 ppm ethanol is 0.5 and 10 ppm of isoprene is 0.18

A radar plot shown below compares the cross-sensitivities of the monoclinic and orthorhombic WO_3 towards NO_2 and other reducing gases.

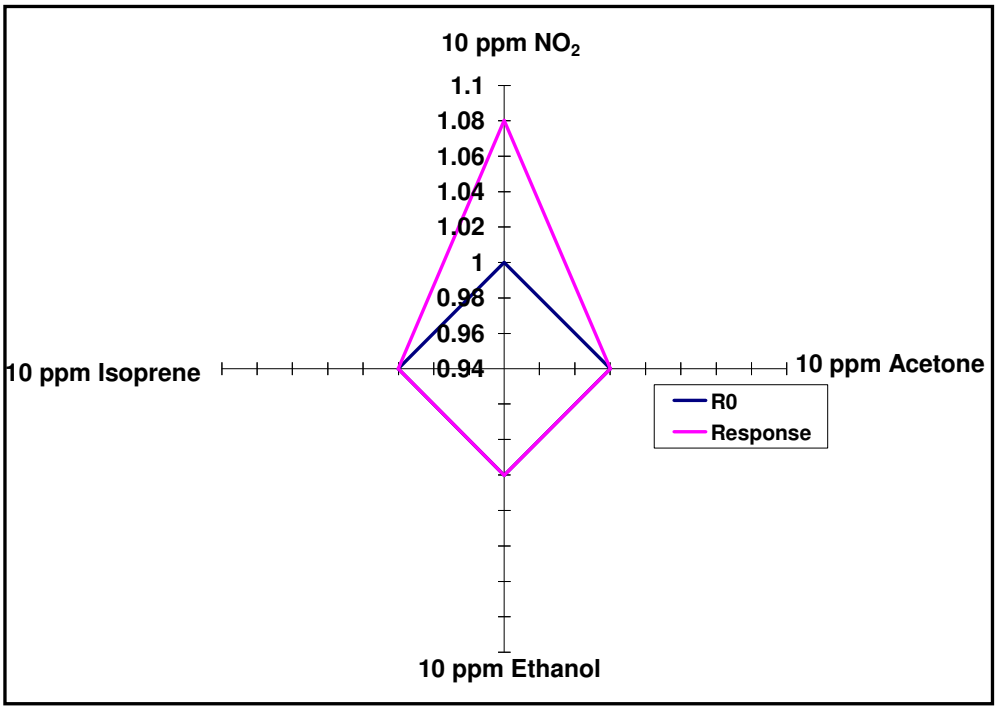

Figure 3.19: Comparison of sensitivities of the monoclinic polymorph at 400°C

The monoclinic polymorph shows no cross-sensitivity toward reducing gases like hydrocarbons and volatile organic compounds, while the orthorhombic polymorph although has a higher sensitivity for a similar concentration of NO_2, has cross-sensitivity towards reducing gases.

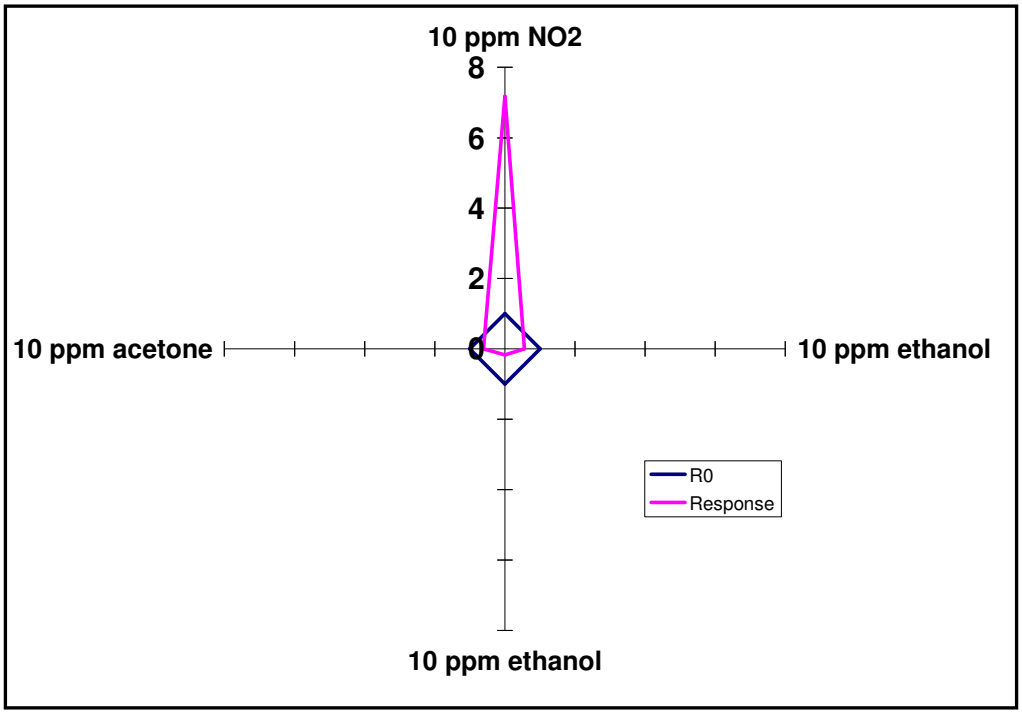

Figure 3.20: Comparison of sensitivities of the orthorhombic polymorph at 500°C

3.2.2 Ultra low Concentration Sensing of NO and NO_2:

The significance of NO_x was explained in chapter 1 and it is essential to be able to sense low concentrations of nitric oxide and nitrogen dioxide in order to be able to use these sensors in breath analysis. This section will present the sensing results using the monoclinic and orthorhombic polymorph for ppb level sensing of NO and NO_2. The lowest concentration analyzed was 300 ppb. Owing to the limitations with the concentrations of the starting gas, concentrations lower than 300 ppb could not be achieved with sufficient accuracy.

3.2.2.1 Monoclinic Polymorph:

The NO_2 and NO sensing response of the monoclinic polymorph is shown in figure 3.21 and 3.22 and the corresponding sensitivity variations are shown in figures 3.23 and figure 3.24.

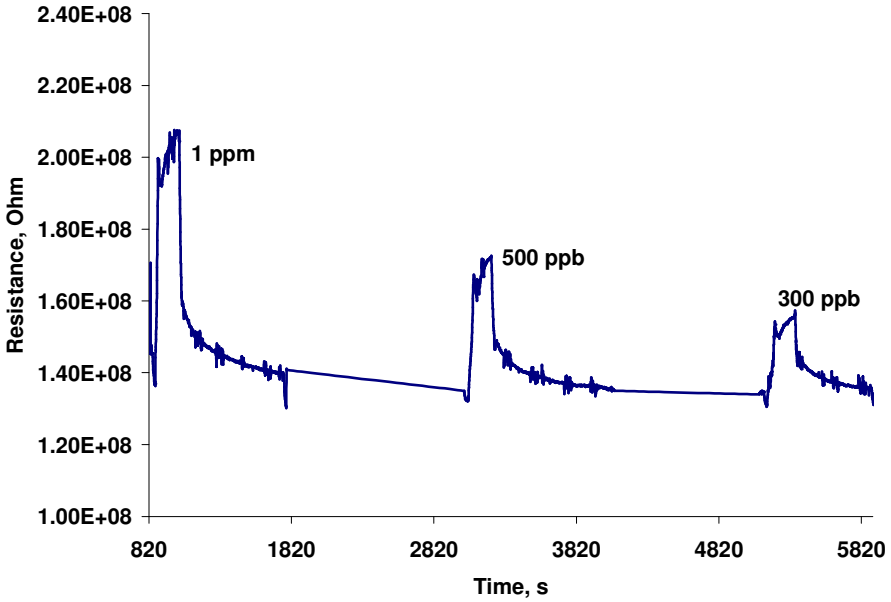

Figure 3.21: Sensing response of monoclinic polymorph at 400°C to NO

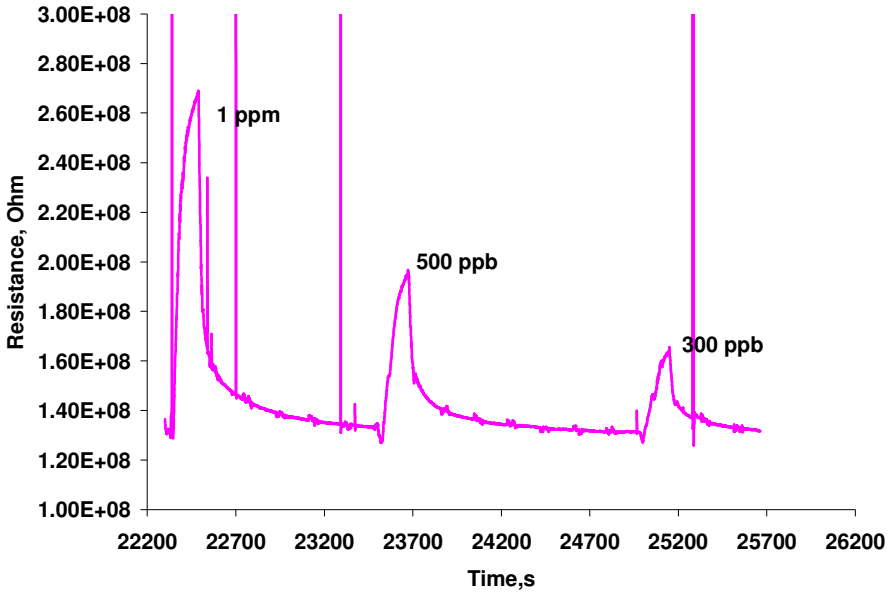

Figure 3.22: Sensing response of monoclinic polymorph at 400°C to NO_2

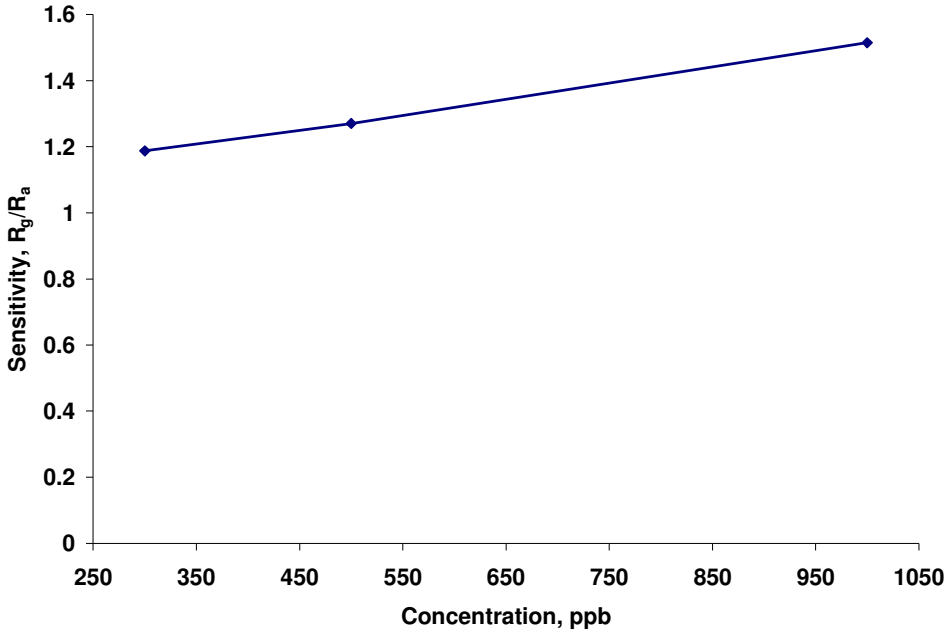

Figure 3.23: Sensitivity variation of the monoclinic sensor with NO concentration at 400°C

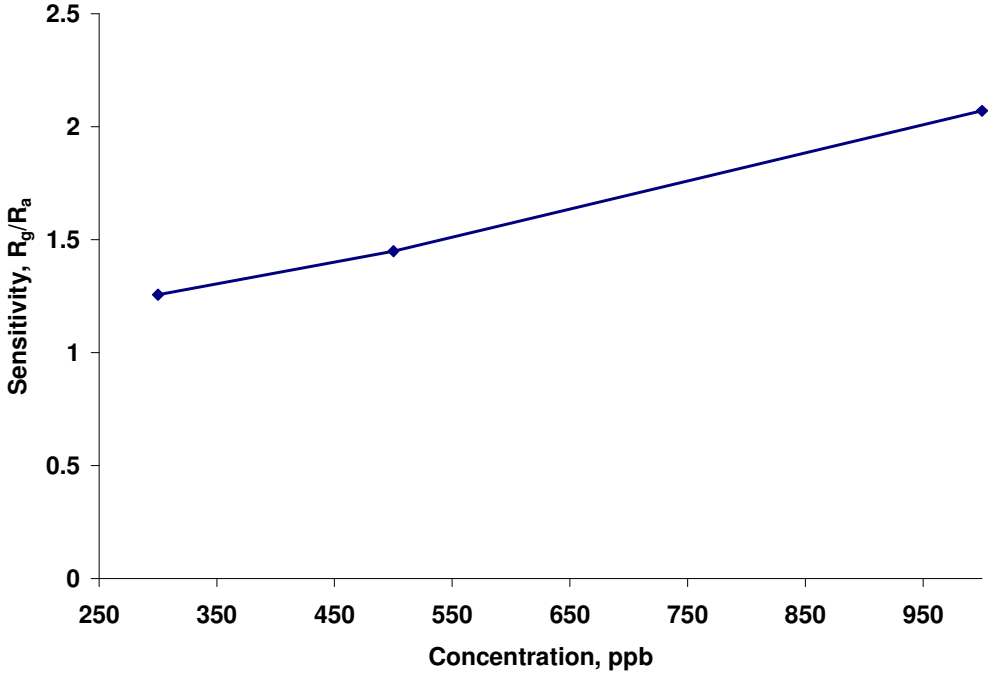

Figure 3.24: Sensitivity variation of the monoclinic sensor with NO_2 concentration at 400°C

The sensitivity of the monoclinic polymorph for the same concentration is greater for NO than NO_2, although the sensing behavior is very similar.

3.2.2.2 Orthorhombic polymorph:

It is known from previous work [15] that the highest sensitivity towards NO_2 in orthorhombic polymorph is attained between 200-300°C. The sensing temperature for ppb level analysis was chosen to be 200°C. Figures 3.25 and 3.26 show the NO and NO_2 sensing responses of the orthorhombic polymorph. The lowest concentration measured for the orthorhombic polymorph is 500 ppb.

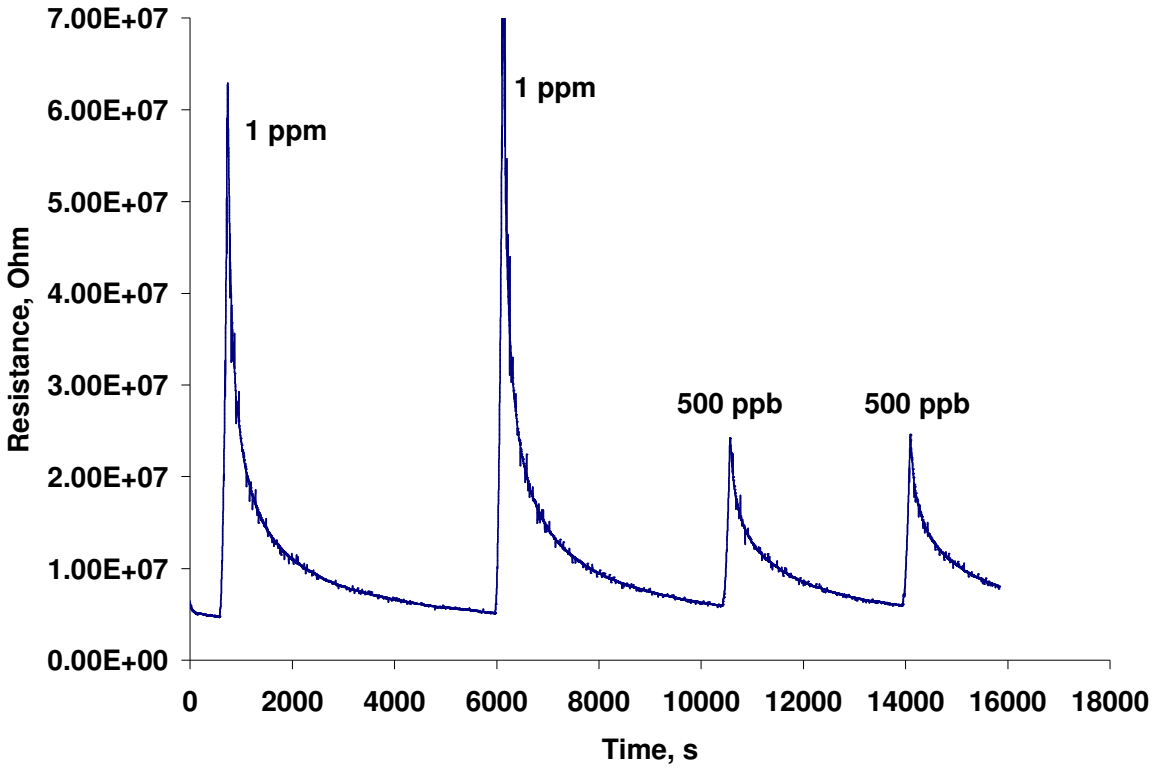

Figure 3.25: Sensing response of orthorhombic polymorph at 200°C to NO

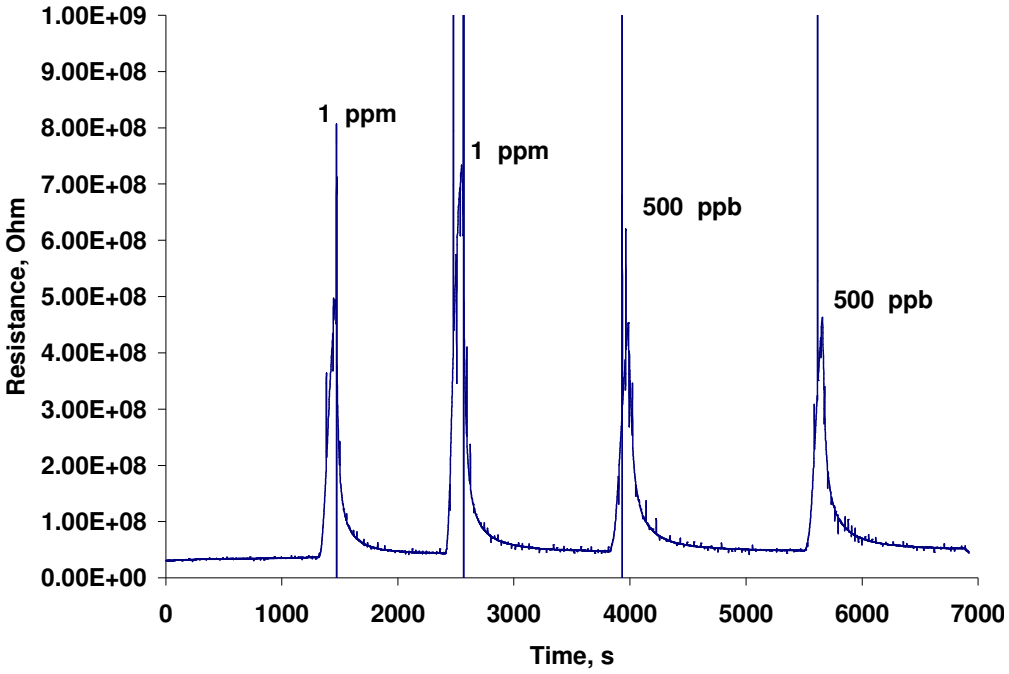

Figure 3.26: Sensing response of orthorhombic polymorph at 200°C to NO_2

Figures 3.26 and 3.27 show the radar plots of comparing the NO and NO_2 response of the monoclinic and orthorhombic sensors to same concentration of reducing gases as in section 3.2.1.

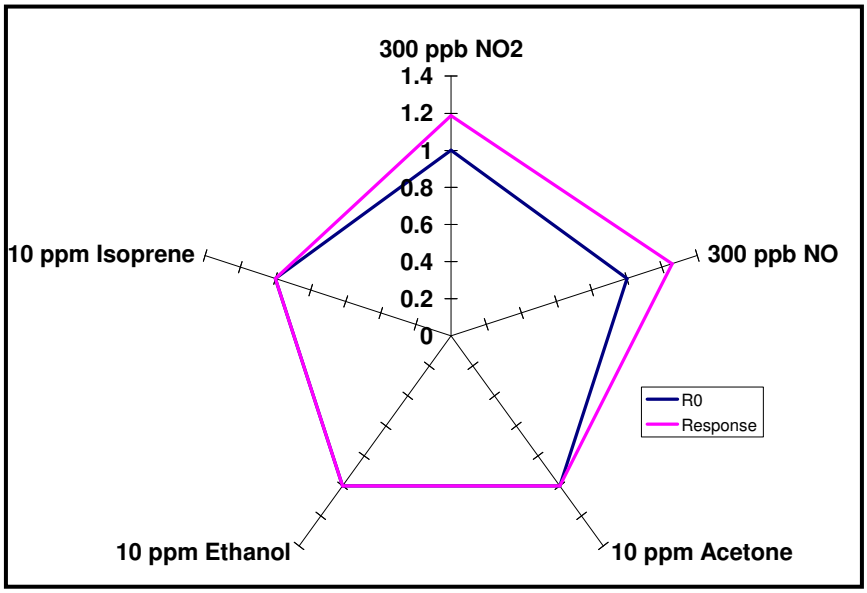

Figure 3.27: Comparison of sensitivities of the monoclinic polymorph at 400°C

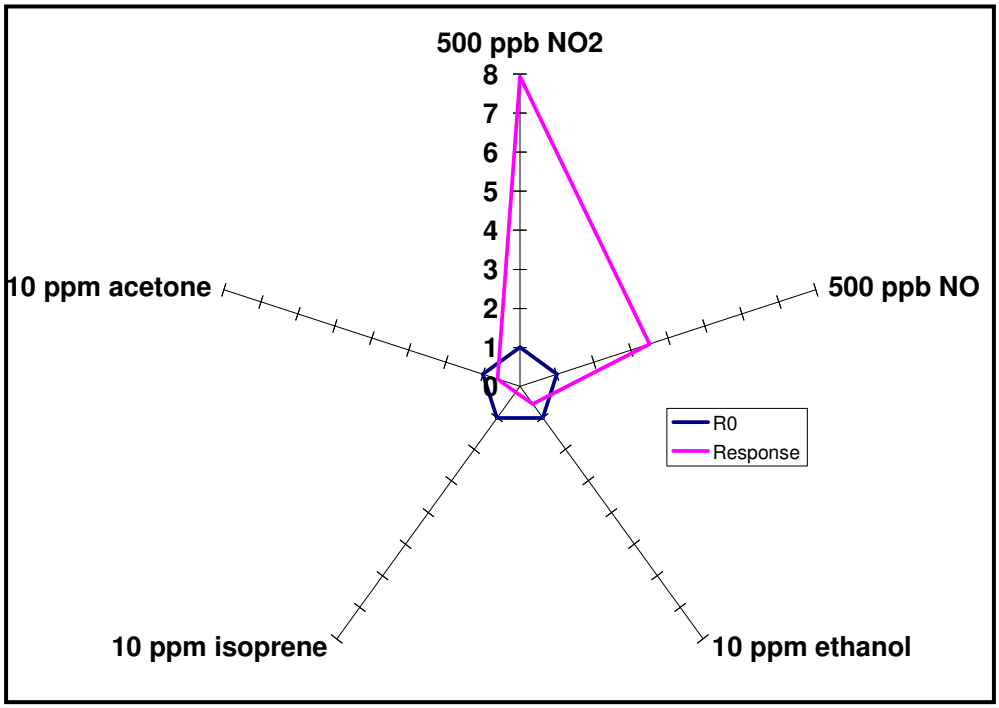

Figure 3.28: Comparison of sensitivities of the orthorhombic polymorph at 200°C

References:

1. JCPDS CAS-No. 20-1324, *JCPDS-International Centre for Diffraction Data.* Ref: Roth and Waring: *Anal. Chem.***10**, (1938), 457.
2. JCPDS CAS-No.36-0102, *JCPDS-International Centre for Diffraction Data.* Ref: Booth et al: *J. Solid State Chem.***41**, (1982), 293.
3. Bursill L.A., Proceedings of the Royal Society A, 311 (1969) p267.
4. J.G. Allpress, R.J.D. Tilley, M.J. Sienko, Examination of substoichiometric WO3_x crystals by electron microscopy, J. Solid State Chem. 3 (1971) 440–451.
5. M.F. Daniel, B. Desbat , J.C. Lassegues, B. Gerand, M. Figlarz, "Infrared and Raman strudy of WO_3 tungsten trioxides and $WO_3.xH_2O$ tungsten trioxide hydrates", *J. Solid. State. Chem.* **67**, (1987), 235-247.
6. M.F. Daniel, B. Desbat , J.C. Lassegues, R. Garie, "Infrared and Raman spectroscopies of rf sputtered tungsten oxide films", *J. Solid. State. Chem.* **73**, (1988), 127-139.
7. K. Nonaka, A. Takase, K. Miyakawa, "Rmana spectra of sol-gel derived tungsten oxides", *J. Mater. Sci. Lett.* **12**, (1993), 274-277.
8. A. Takase, K. Miyakawa, "Raman study on sol-gel derived tungsten oxides from tungsten ethoxide", *Jpn. J. Appl. Phys.* **30**, (1991), L1508-L1511.
9. E. Cazanelli, C. Vinegoni, G. Mariotto, A. Kuzmin, J. Purans, "Raman study of the phase trnasition sequence in pure WO_3 at high temperature and in H_xWO_3 with variable hydrogen content", *Solid. State Ionics* **123**, (1999), 67-74.

10. S. Piscanec, A.C Ferrari, M. Cantoro, S. Hoffmann, J.A. Zapien, Y. Lifshitz, S.T. Lee, J. Robertson, "Raman spectrum of silicon nanowires", *Mat.Sci.Eng.C.* **23**, (2003), 931-934.
11. V. Swamy, B.C. Muddle, Q. Dai, "Size-dependent modifications of the Raman spectrum of rutile TiO_2", *Appl. Phys. Lett.* **89**, (2006), 163118-1-163118-3.
12. R. D. Bringans, H. Höchst, H. R. Shanks, "Defect states in WO_3 studied with photoelectron spectroscopy", *Phys. Rev. B* **24,** (1981), 3481.
13. S. Santucci, C. Cantalini, M. Crivellari, L. Lozzi, L. Ottaviano, M. Passacantando, "X-ray photoemission spectroscopy and scanning tunnelling spectroscopy study on the thermal stability of WO_3 thin films", *J. Vac. Sci. Technol. A* **18,** (2000) 1077-1082.
14. S. Santucci, L. Lozzi, E. Maccallini, M. Passacantando, L. Ottaviano, "Oxygen loss and recovering induced by ultrahigh vacuum and oxygen annealing on WO_3 thin film surfaces: influences on the gas response properties", *J. Vac. Sci. Technol. A* **18,** (2000) 1077-1082
15. Arun Kapaleeswaran Prasad, "Study of gas specificity in MoO_3/WO_3 thin film sensors and their arrays", Ph.D. Thesis, SUNY Stony Brook, NY, (2005).

CHAPTER 4

MoO_3 Nanowires

4.1 Material Characterization

4.1.1 Differential Scanning Calorimetry:

Differential scanning calorimetry was carried out on the as received sol-gel sample of molybdenum oxide to ascertain the phase transformation temperature fields. The percent weight loss versus temperature graph is shown in figure 4.1.

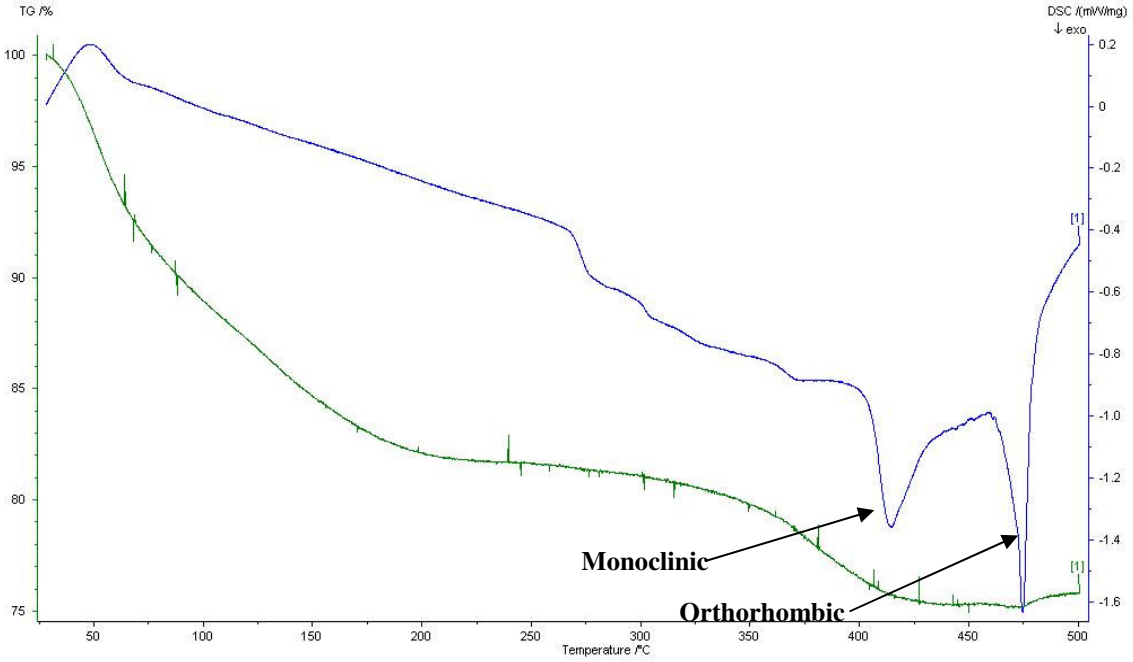

Figure 4.1: DSC data for the MoO_3 sol-gel precursor

Lower temperatures show the weight loss due to burning of alcohol in the sol-gel and later broad region shows a drop due to loss of water. As can be seen from the graph

two sharp peaks can be observed; one at 425°C and the other at 490°C, corresponding to the monoclinic and orthorhombic transformations of MoO_3 [1]. This serves as the basis for heating the sol-gel at 500°C for 8 hours, to get complete transformation of the amorphous sol-gel to the desired orthorhombic structure in the sensor.

4.1.2 Electron Microscopy

(a) Composite polymer mats: Figure 4.2 is a TEM micrograph of the as received electrospun polymer/oxide mat. Composite nanofiber diameters range from 20nm-100nm. During the electrospinning process oxide "splats" may be deposited on the surface of the polymer fibers. The occurrence of these defects in the electrospun matrix can be controlled by varying the processing conditions as well as the ratio of polymer to metal oxide in the pre-spinning solution. It has been demonstrated that the electrospinning technique drives the formation of elongated, amorphous, sol-gel based fibrous networks of the oxide resulting in core-shell morphology (an amorphous metal oxide core with well defined walls surrounded by a polymer shell). Further analysis of the as spun mat at a higher magnification in figure 4.3, reveals that the aligned "encapsulation" of the metal oxide sol-gel inside the polymeric (PVP) fiber has a diameter of the order of 10-50nm which reflects the diameter of the final nanowires obtained after calcination.

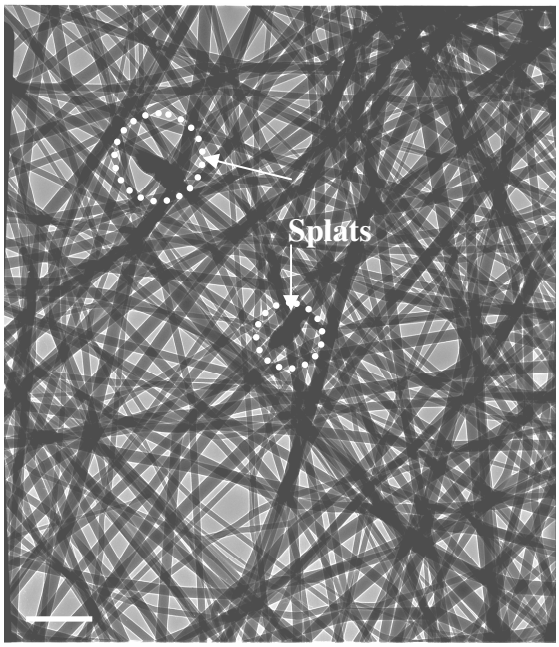

Figure 4.2: Low magnification TEM image of the PVP-MoO_3 mat before calcination

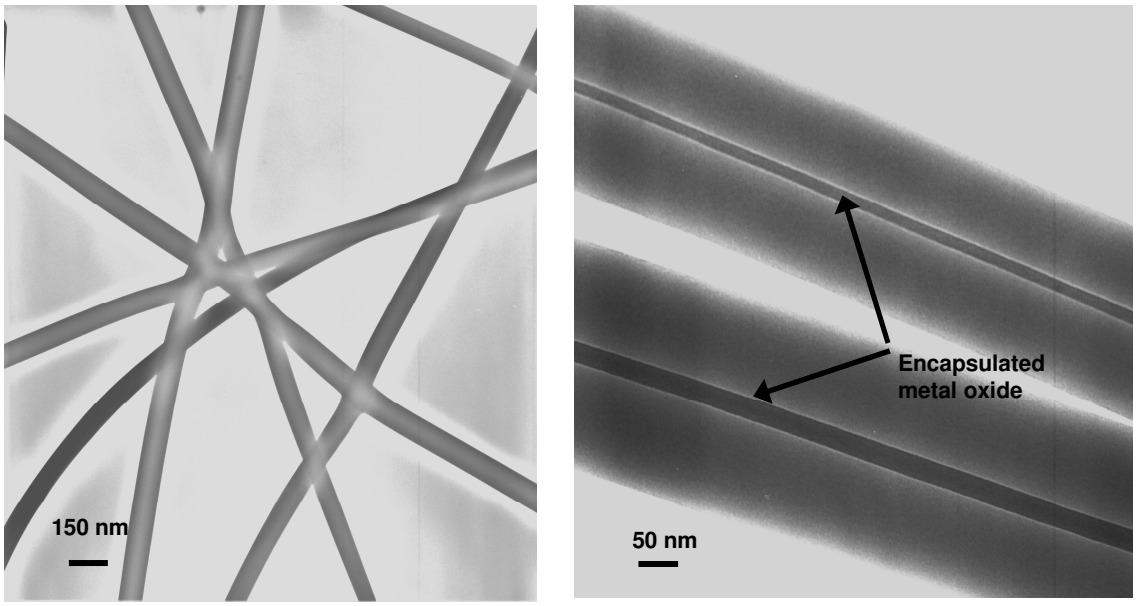

Figure 4.3: TEM micrograph of (a) the as spun PVP mat; and (b) the PVP-MoO_3 electrospun composite mat before calcination showing the aligned encapsulation of the sol-gel along the polymer fiber walls (indicated by arrows)

Figures 4.4 and 4.5 are HRTEM micrographs illustrating the morphology and structure of the nanowires after calcination, deposited on Si_3N_4 and carbon TEM grids respectively. The inset in figure 4.4 is a higher magnification image of the same nanowire revealing its lattice planes. As can be seen from these images, the nanowires are single crystals. Their dimensions are about 10-15nm in width and 1-2µm long. The measured d-spacings for the nanowires shown in these figures were 6.944 Å, 3.9Å and 1.822 Å corresponding to the (020), (100) and the (230) planes of the orthorhombic MoO_3 polymorph respectively. The standard JCPDS file corresponding to this structure is 05-0508; the unit cell parameters for the above crystals are a=3.9630Å, b=13.856 Å, c=3.6966 Å. The crystal belongs to the space-group Pbnm (62) [2].

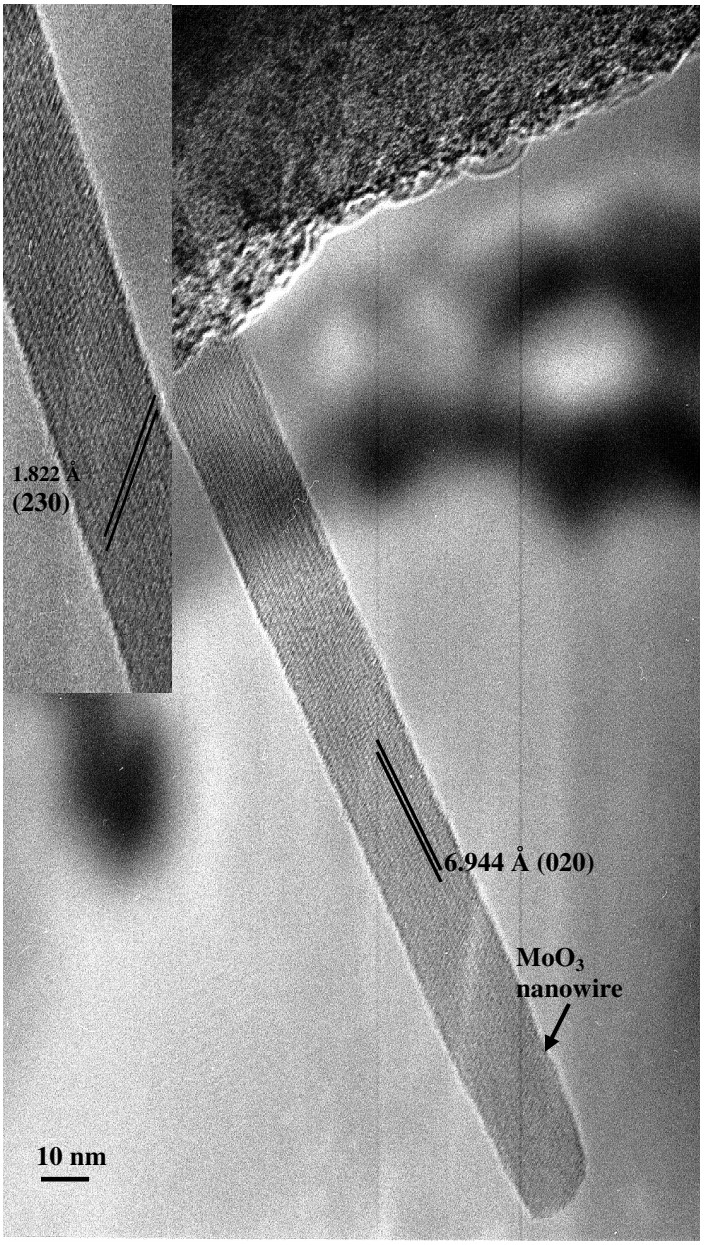

Figure 4.4: HRTEM image of a MoO_3 nanowire on a Si_3N_4 grid; (inset) higher magnification image of the same nanowire

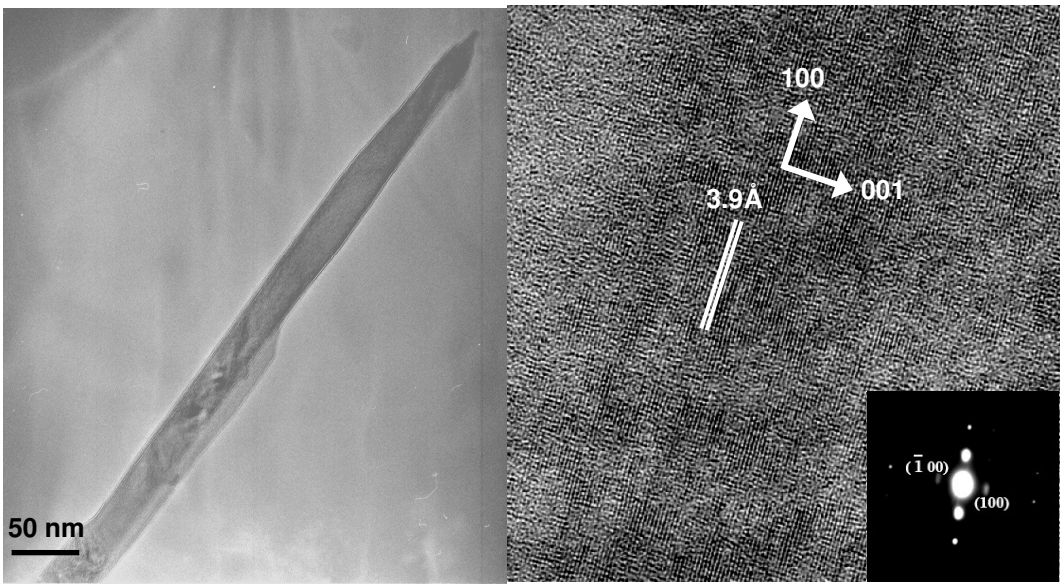

Figure 4.5: High resolution transmission electron microscopy of MoO_3 nanowire showing the growth direction of the nanowires

Two issues concerning the growth and crystallography of the nanowires need to be addressed. The first is why the metal oxide would grow in to such high aspect-ratio structures. The second is why the resultant nanowire would be a single crystal**.** The former can be answered by considering the basic crystallographic nature of molybdenum trioxide. The α-MoO_3 (orthorhombic) consists of distorted edge-sharing MoO_6 octahedra (distortion of the cubic ReO_3 structure). Octahedral layers share edges along the a-axis [100] and corners along the c-axis [001]. Along the b-axis the layers are bound by van der Waals forces. Moreover, MoO_3 is known for growing in to anisotropic morphologies [3]. Growth along the a-axis is energetically favorable owing to the fact that only one Mo—O bond has to created as opposed to the c-direction in which two such bonds will

have to be formed. Figure 4.5 illustrates the preferred growth orientation for MoO_3 nanowires.

In order to understand the mechanism behind the formation of single crystals, the polymorphic nature of the metal oxide has to be considered. Heat-treating the sol-gel at 500°C for 8 hours results in nanostructured polycrystalline grains of the orthorhombic phase. This is considered to be the "thermodynamically stable" phase of the MoO_3 system. Earlier work based on the titania system by Gouma et al [4-5] has shown that metastable to stable polymorphic reactions in oxides require the formation of critical size nuclei and involve the oriented attachment of nanocrystalline aggregates into large aspect ratio and abnormally large single crystals of preferred orientation that retain the morphology (contours) of the original aggregate [5]. In the case of electrospun composites, the morphology of these aggregates is determined by the presence of the polymeric fiber wall (before its decomposition temperature is reached). Thus, the single crystals of the stable polymorph may grow undisturbed until the sol-gel runs out along the fiber or until the fiber path is interrupted. In-situ experiments in the TEM are required to directly capture the process of single crystal nanowire formation. It is suggested that there is a particular heat-treatment condition for each metal oxide that should yield single crystal nanowires and which depend on the relative phase stabilities of the various polymorphs of the respective oxide system. Related work by the authors has produced WO_3 single crystal nanowires by this method [6].

4.2 Sensor Characterization

The protocol for the preparation of nanowire sensors is as follows. The calcined nanowire mat was dispersed in ethanol and ultrasonicated for 5-10 minutes. The solution was then drop-coated on to the sensor substrates.

The sensing response of the MoO_3 nanowire mats to NH_3 has been assessed and compared with that of sol-gel based films stabilized under the same conditions. NH_3 has been chosen as the analyte of interest since earlier studies by the authors have shown that the α-orthorhombic phase of MoO_3 selectively detects NH_3 in the presence of interfering gaseous compounds such as CO, NO, etc [7-8]. Thus, the single crystals of the metal oxide nanowires produced are of the particular polymorph, α-phase MoO_3, and are expected to respond to NH_3 with high sensitivity.

Figure 4.6 is the SEM image of the nanowire mat on the sensor substrate after exposure to the analyte. The inset is a high magnification image of a typical nanowire in the cycled mats.

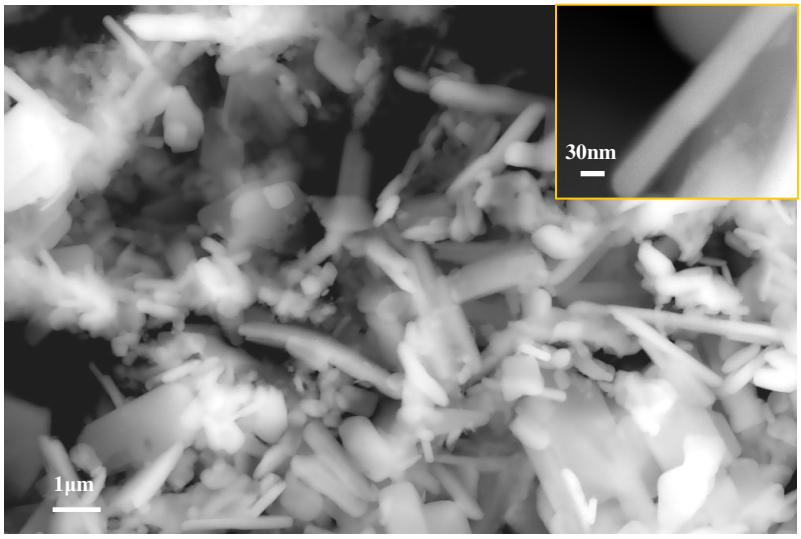

Figure 4.6: SEM images of the nanowire mat on an Al_2O_3 substrate after sensing; (inset) High magnification image of a single MoO_3 nanowire

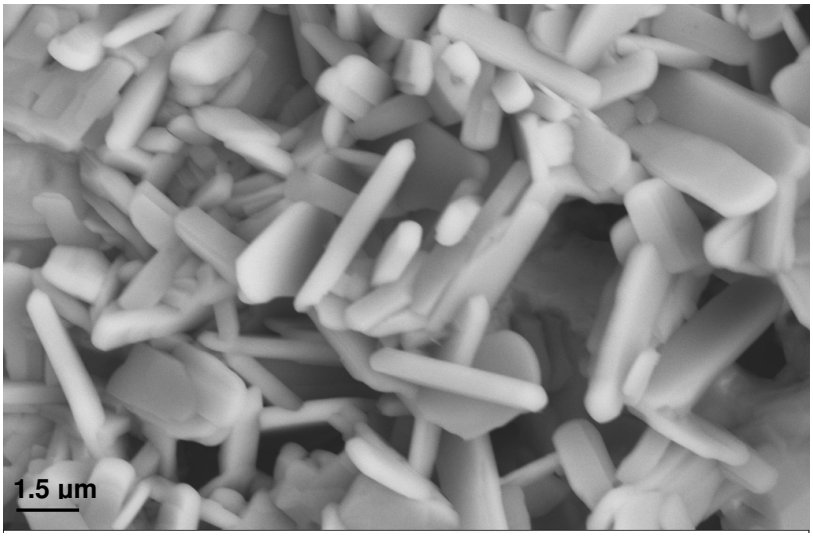

Figure 4.7: SEM images of the MoO_3 sol-gel on an Al_2O_3 substrate after sensing

Figure 4.7 shows a scanning electron microscopy image of a polycrystalline MoO_3 film for comparison. The sol-gel was prepared and deposited on the sensor substrate the same way as described in chapter 2.

Sensitivity of the sensing elements (nanowires vs. nanoparticles) to NH_3 was calculated using the ratio:

$$S = R_a/R_g \qquad (1)$$

where R_g is the resistance on exposure to the gas analyte and R_g is the initial resistance of the sensing element in air.

Both the nanowire mat and the sol-gel thin film were heat stabilized at 500°C for 8hrs in air prior to the sensing measurements to obtain the orthorhombic crystal structure. The sensing experiments were carried out at an operating temperature of 450°C in order to avoid any undesirable polymorphic transformations in the metal oxide. The NH_3 concentration was varied from 50ppm to 300ppm in a background mixture of 80%N_2 and 20%O_2. The gas pulses were 3-5 minutes long and were repeated to ensure reproducibility in the sensing response. Figure 4.8 depicts the sensitivity of the MoO_3 sol-gel sensor to NH_3. The response time and recovery time for this sensor varied from 1 – 2 minutes. The image in figure 4.9 details the sensing response of the nanowires. The response and recovery times for this sensor are comparable to that of the sol-gel sensor and range from 0.5 – 2 minutes.

Upon the exposure to NH_3 (a reducing gas), the resistance decreased in both the nanowire and the sol-gel sensors, confirming that both the sensors exhibit n-type semiconducting behavior. The results from the sensing tests reveal that the sensitivity of the nanowire mat is twice that of the sol-gel sensor for 50 ppm. It is triple the response of the sol-gel sensor for 100 ppm NH_3; quadruple the response of the sol-gel sensor for 200 ppm NH_3; and increases to one order of magnitude higher than that of the MoO_3 sol-gel sensor as the concentration of NH_3 increases to 300 ppm. The calculated sensitivity data for both sensors are outlined in Table 4.1. .

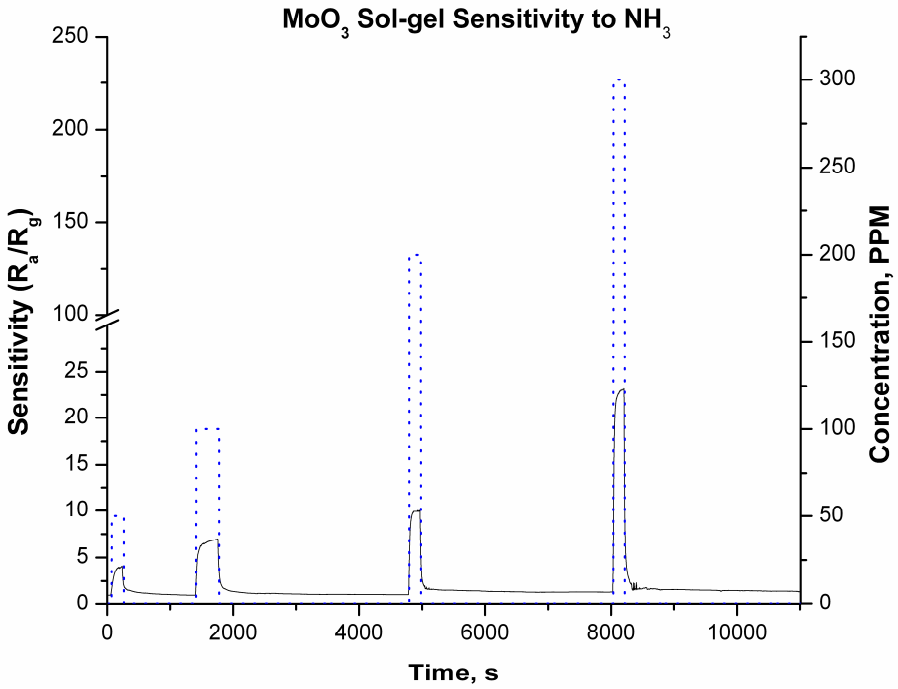

Figure 4.8: Sensitivity of nanocrystalline MoO_3 sol-gel films to various concentrations of NH_3

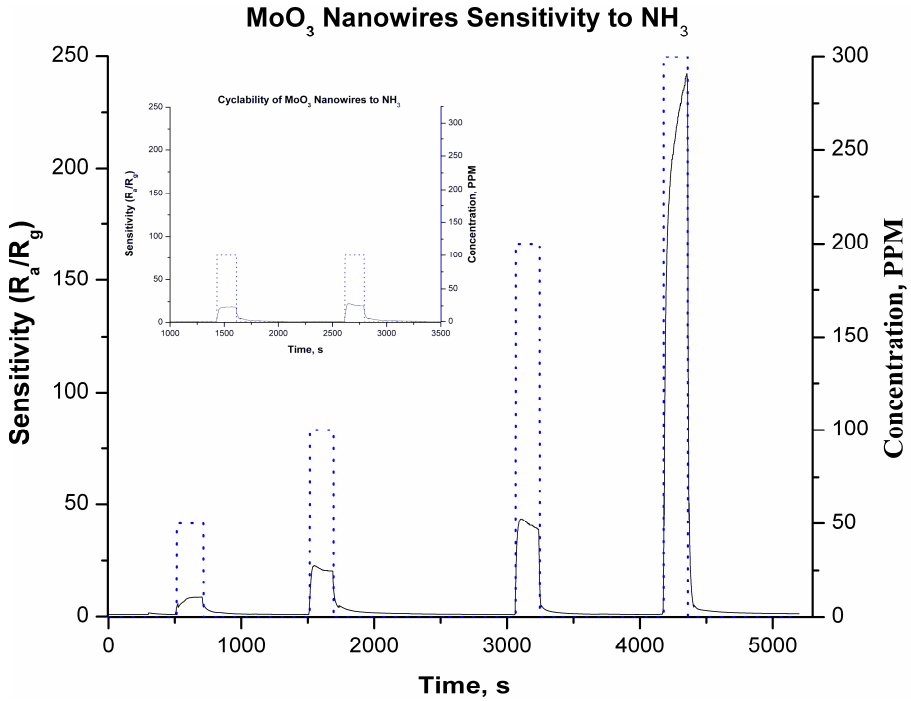

Figure 4.9: Sensitivity of nanocrystalline MoO_3 nanowires to different concentrations of NH_3; (inset) Reproducibility of MoO_3 to 100ppm NH_3

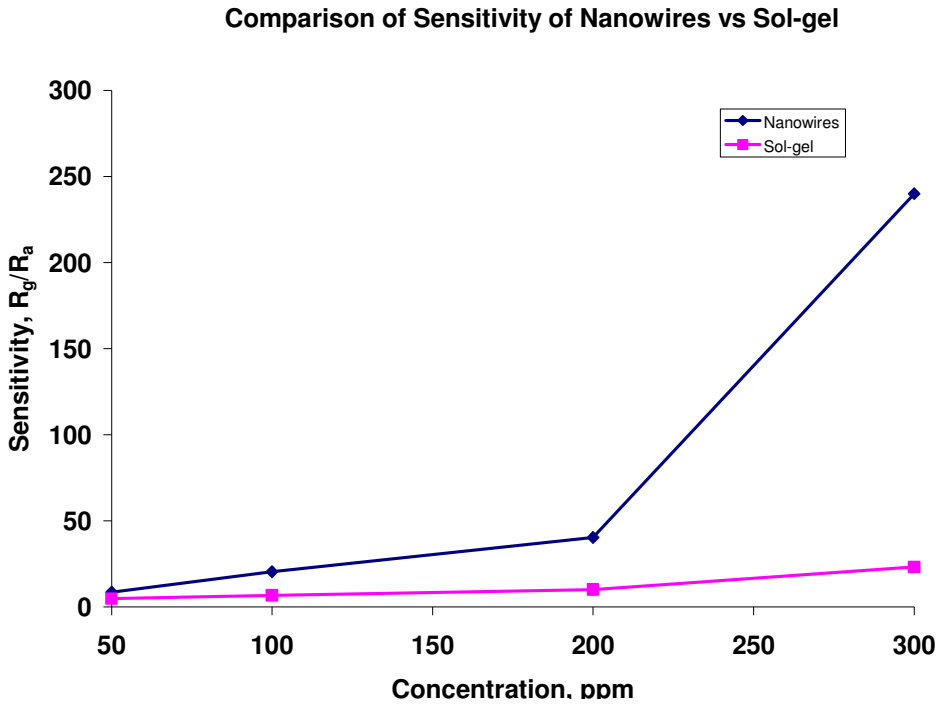

Figure 4.10: Comparison of Sensitivity of MoO_3 nanowires vs sol-gel sensors

Table 4.1: Calculated sensitivity data for the nanowire and sol-gel sensors

NH_3 Concentration (ppm)	Sensitivity	
	Nanowires	Sol-gel
50	8.6	4.7
100	20.5	6.8
200	40.3	10
300	240	23.1

References:

1. Arun Kapaleeswaran Prasad, "Study of gas specificity in MoO_3/WO_3 thin film sensors and their arrays", Ph.D. Thesis, SUNY Stony Brook, NY, (2005).
2. JCPDS CAS-No. 05-0508, 2000, *JCPDS-International Centre for Diffraction Data.* Ref: Swanson and Fuyat: *Natl. Bur. Stand. Circ.* **539**(3), 30 (1954).
3. X.L. Li, J.F. Liu, Y.D. Li, "Low-temperature synthesis of large-scale single-crystal molybdenum trioxide (MoO_3) nanobelts", *Appl. Phys. Lett.* 81, p. 4832-4834, (2002)
4. P. I. Gouma and M. J. Mills, "Anatase to Rutile Transformation in Titania Powders", *J. Am. Ceram. Soc.,* 84 [3], p. 619-622 (2001)
5. P. I. Gouma, P. K. Dutta, and M. J. Mills, "Structural Stability of Titania Thin Films", *Nanostructured Materials*, 11(8), p. 1231-1237 (1999)
6. K.M. Sawicka, A.K. Prasad and P.I. Gouma, "Metal Oxide Nanowires for Use in Chemical Sensing Applications", *Sensor Letters*, 3, p. 1-5 (2005)
7. P. Viswanathamurthi, N. Bhattarai, H.Y. Kim, D. I. Cha, and D.R Lee, "Preparation and morphology of palladium oxide fibers via electrospinning", *Materials Letters*, 58, p. 3368-3372 (2004)
8. N. Dharmaraj, H.C. Park, C.K. Kim, H.Y. Kim, and D.R. Lee, "Nickel titanate nanofibers by electrospinning", *Materials Chemistry and Physics*, 87: p.5-9 (2004)

CHAPTER 5

Sensor Arrays

Electronic olfactory systems ('artificial' noses) are designed to detect an 'odor' for applications ranging from the food and cosmetic industry to bio-medical applications [1]. They usually consist of an array of 'non-selective' sensors that have been precalibrated to identify a particular 'fingerprint' of a smell or odor. One major shortcoming of these types of arrays is that they are non-selective and hence need a pattern recognition algorithm and extensive signal processing to identify a target analyte. A typical value for the number of sensors in the array ranges anywhere from 10 to 30. An innovative yet simpler approach is to use an array of 2-3 highly selective sensors. Sensor selectivity as defined in chapter 1 is the selective response of a sensor to a particular gas (class of gases) in the presence of interfering gases.

This chapter focuses on the use of the materials and sensors discussed in the preceding chapters in an array configuration for selective sensing. The analytes of choice also can be classified in two categories, namely oxidizing gases (NO_x - includes both NO_2 and NO) and reducing gases (hydrocarbons, VOCs and also amines). The sensors that are expected to be selective to these particular gases are chosen from the gas-polymorph selection map also described in chapter 1.

5.1 Sensors:

The sensors used for this study belong to three distinct classes

1. Cubic ReO_3 based preovskite- WO_3
2. Cubic ReO_3 based layered perovskite- MoO_3
3. Rutile structure- a hybrid of MoO_3 and TiO_2

The sensors were prepared in the same way as described in experimental section and were tested in the EOS 835 (SACMI, IMOLA-Italy) prototype setup as described in chapter 2. The original non-selective sensors from the e-nose were replaced with selective ones.

5.2 Gases:

Ethanol, Isoprene and Acetone, NOx:

Ethanol is the major component in drinking alcohol. When consumed, alcohol is immediately absorbed into the blood capillary structure of each successive body tissue and organ it is directly exposed to. Alcohol is somewhat unique in that as it enters the blood stream, its chemical structure is not metabolized but remains unaltered and intact. Consequently, alcohol becomes a separate and definable component of blood flow. As blood flows into and through the alveoli (air sacs) in the membranes of the lungs, carbon dioxide molecules are exchanged for oxygen molecules. Because alcohol will readily evaporate from a solution and is highly volatile, alcohol molecules are released with the carbon dioxide molecules during this gas exchange. Therefore the concentration of alcohol molecules in the alveolar air of expelled breath is related to the concentration of

the alcohol in the blood. As the alcohol in the alveolar air is exhaled, it can be detected by a breath alcohol testing device [2-3].

Isoprene (2-methyl – 1,3-butadiene) is a reactive aliphatic hydrocarbon. It is a colorless liquid, B.P. 35°C (101.325 kPa). It is synthesized by nearly all animals and is present among the hydrocarbon metabolites in human breath. Isoprene originates from the decomposition of di-methylallyldiphosphate, a member of cholesterol and isoprenoids synthetic pathway [4-5]. In other words, the amount of isoprene in expired breath is an indirect measure of amount of cholesterol synthesized and its concentration corresponds to the activity of the enzyme producing cholesterol in our body. Cholesterol is synthesized mainly at night due to high demands on energy supply. Hence isoprene concentration measurement should aid in monitoring the patients suffering from hypercholesterolemia (disorder in cholesterol mechanism), which is a risk factor for atherosclerosis development. This necessitates the need for an isoprene detector which can be used to monitor breath isoprene concentrations.

Acetone on the other hand is a ketone that is naturally found in the human body. Normally more than 80% of the body's energy is derived from carbohydrate metabolism. But in patients with diabetes, there is not enough insulin in the body for glucose/carbohydrate metabolism. If carbohydrate metabolism is limited the cells oxidize the fat reserves for energy. The usual metabolic pathway associated with carbohydrate metabolism is affected and this leads to a build up of ketones and in particular acetone [6-7]. Acetone is passed in the urine and also manifests in the breath making it smell fruity.

NO_xes as described in chapter 1 are also important biomarkers for asthma, lung cancer, and oxidative stress [8-10].

5.2 Data Analysis:

In order to compare multiple sensor responses on the same scale we use what is called a 'radar plot'. An example is shown below. The solid line represents the baseline value and the dotted line represents the value that is varying and polygon apexes represent the corresponding sensors. While comparing multiple sensor responses we plot the variation in sensitivity for the different sensors and the sensitivity is calculated using the following formula

$$S = R_g/R_a$$

Where, S is the sensitivity of the sensor, R_g is the resistance of the sensor in the target gas and R_a is the sensor resistance in air. It thus becomes obvious that in the absence of any gas, the ratio would be equal to one and this is the value of the polygon apexes. In the case of an n-type semiconductor exposed to a reducing gas the ratio will be less than one and exposed to an oxidizing gas the ratio will be greater than one.

5.3 Sensor array responses:

5.3.1 Reducing Gases:

Figure 5.1 through 5.5 show the response of the sensor array to reducing gases hydrocarbons-ethanol, methanol, acetone, isoprene and a VOC namely, carbon monoxide. It is evident from the response graphs that the metal oxide hybrids with the rutile structure have the highest sensitivity towards reducing gases.

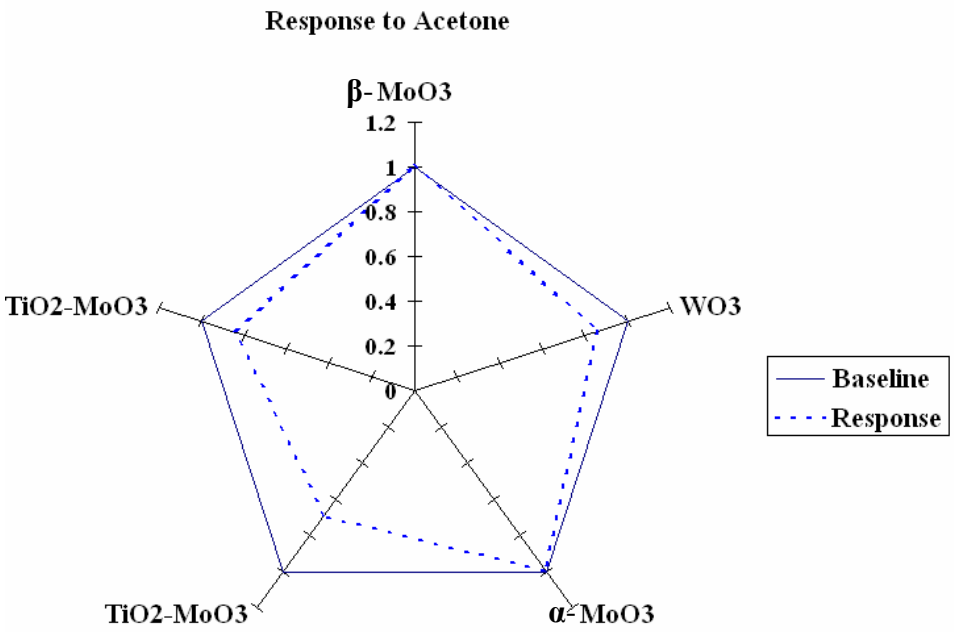

Figure 5.1: Sensing response of the five sensor array to 10 ppm acetone

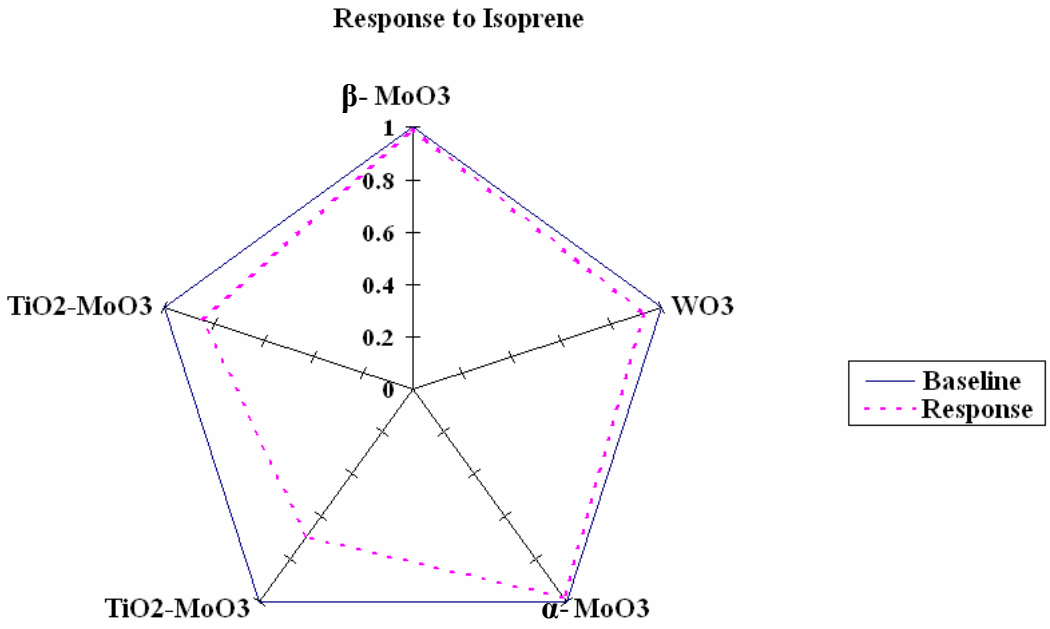

Figure 5.2: Response of the five sensor array to 10 ppm isoprene

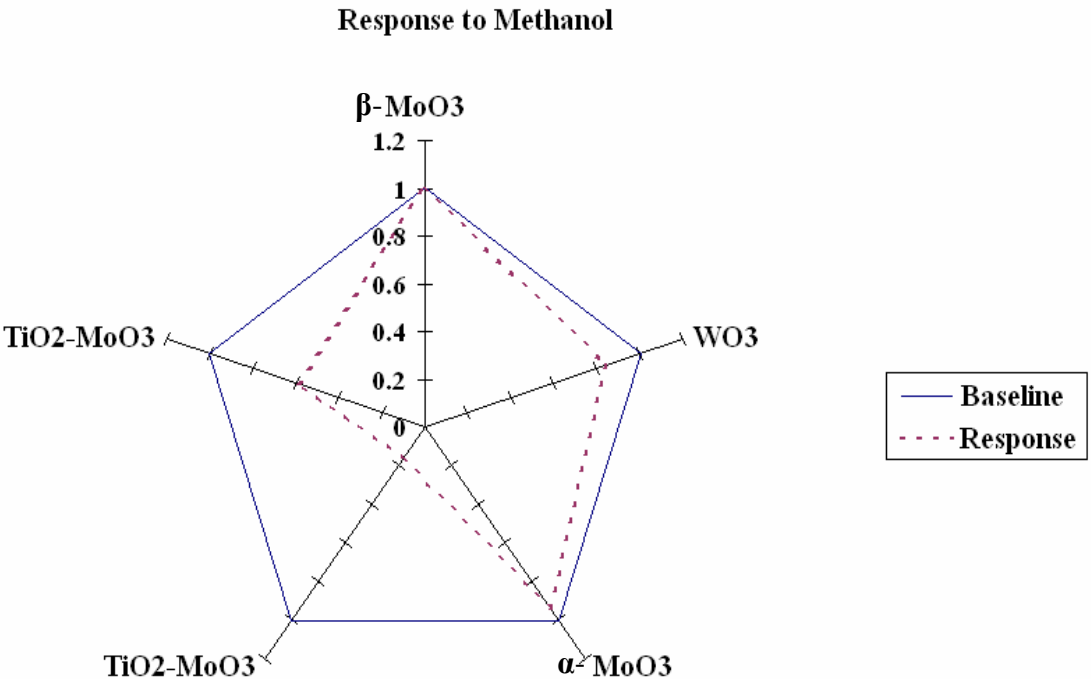

Figure 5.3: Response of the five sensor response 10 ppm methanol

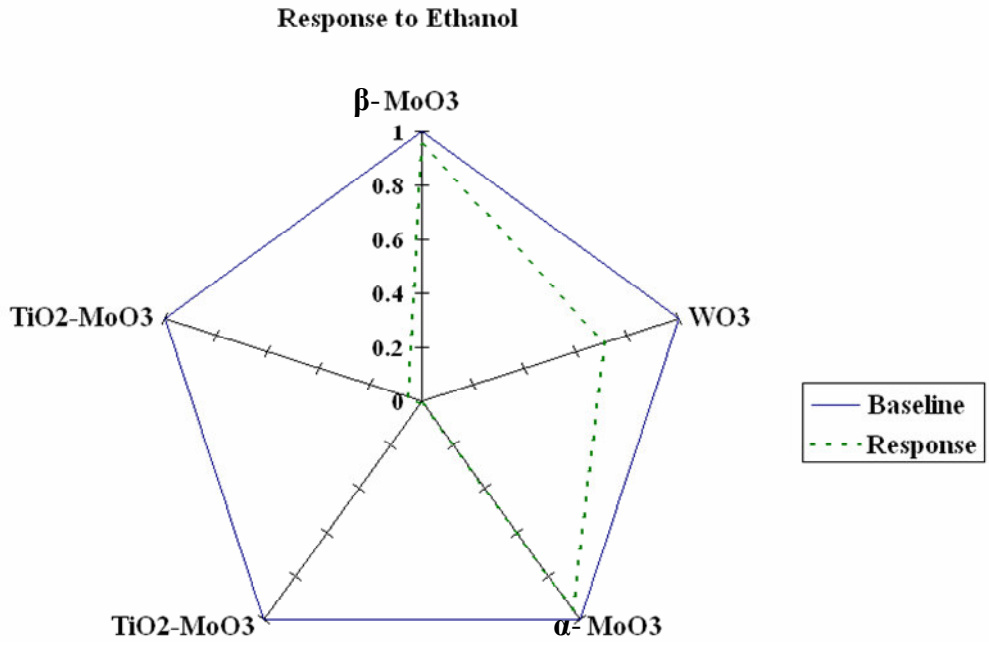

Figure 5.4: Response of the five sensor array to 10 ppm ethanol

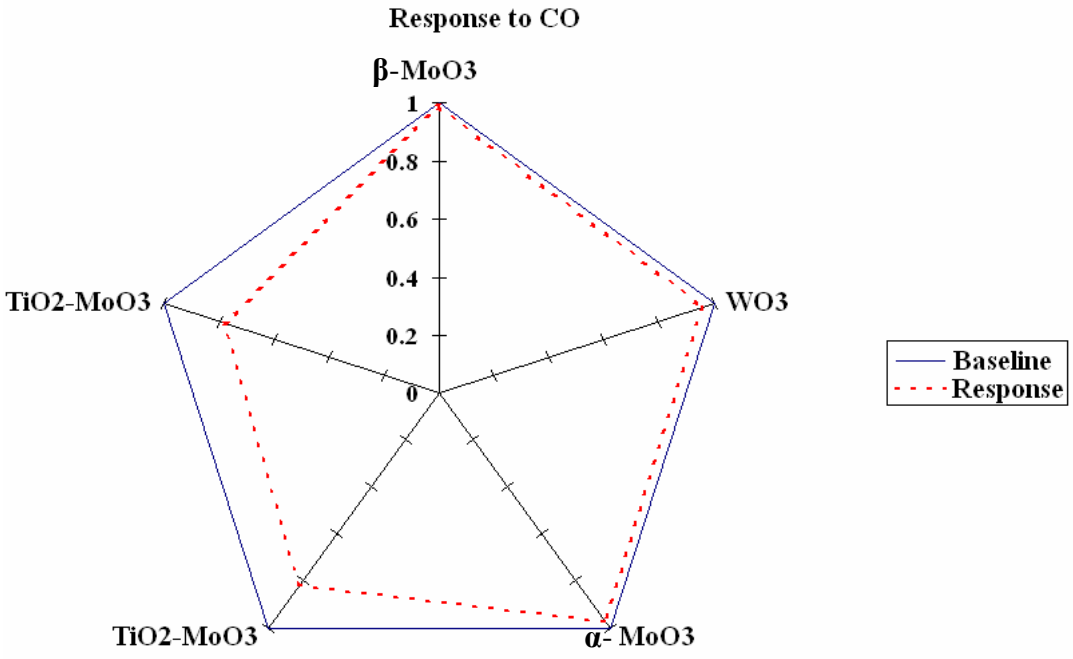

Figure 5.5: Response of the five sensor array to CO

5.3.2 Oxidizing gases:

Figures 5.6 and 5.7 show the response of the sensor arrays (the response of the hybrids is negligible and not shown here). WO_3 has a modified cubic ReO_3 based structure as described in chapter 1. The modified perovskite structure of WO_3 favors adsorption of oxidizing gases compared to reducing gases like CO, ethanol and other hydrocarbons.

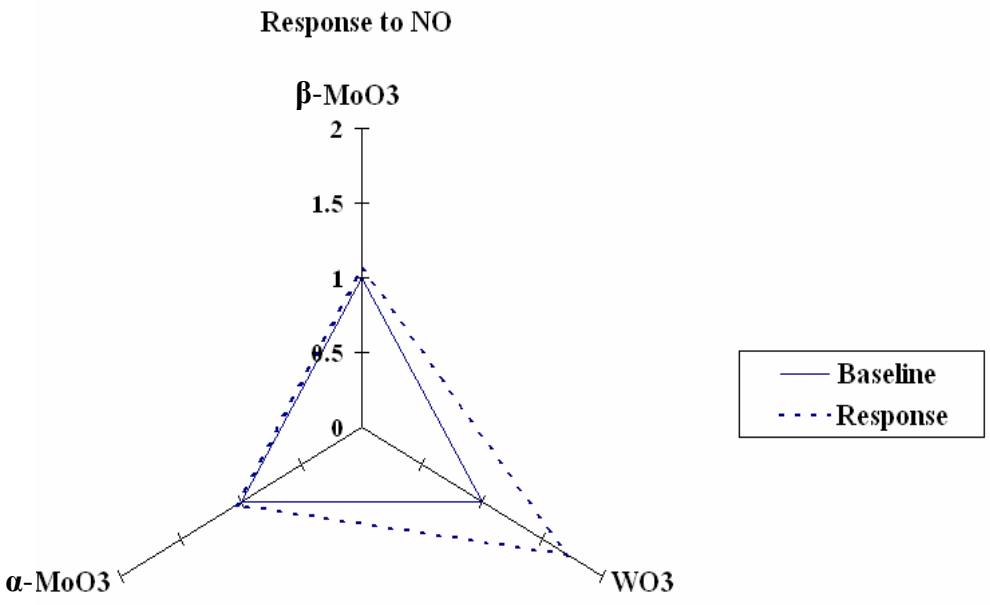

Figure 5.6: Response of the sensor array to 10 ppm NO

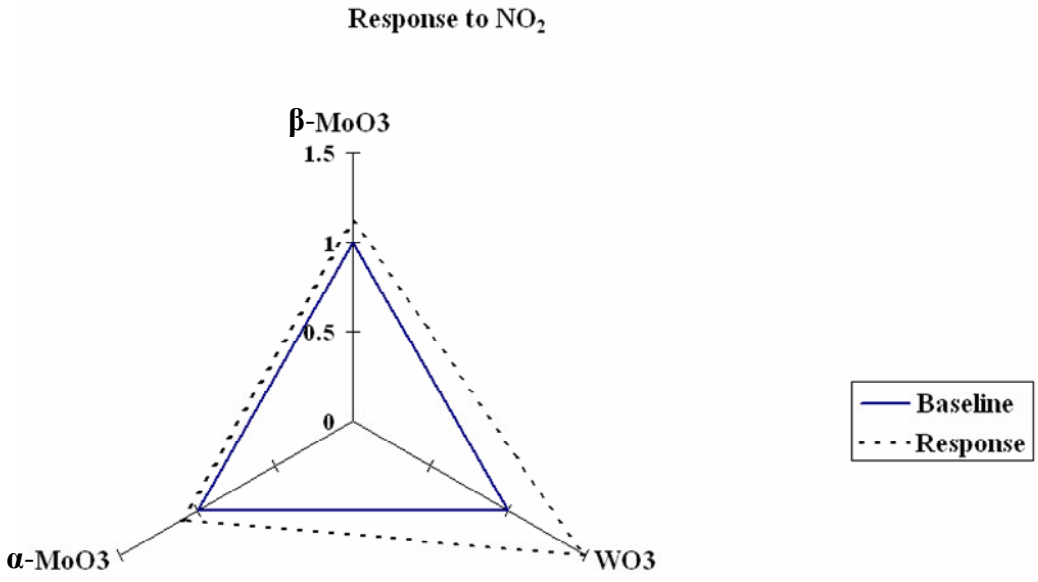

Figure 5.7: Response of the sensor array to 10 ppm NO_2

Figures 5.6 and 5.7 indicate that the perovskite based WO_3 sensor and the β-MoO_3 sensor are sensitive to NO_2 and NO as compared to the rutile based MoO_3-TiO_2 sensors. Thus by using an array of three sensors, each belonging to one class of oxides, most of the gaseous analytes can be distinguished.

References:

1. J.W. Gardner, E.L. Hines, "Pattern analysis techniques", *Handbook of Biosensors and Electronic Noses: Medicine, Food, and the Environment* ed E Kress-Rogers (Boca Raton, FL: CRC Press), 1997, 633–652.
2. D.A. Labianca, "Estimation of blood alcohol concentration", *J. Chem. Edu.* **69**, (1992), 628-632.
3. http://www.craigmedical.com/Breathalyzer_FAQ.htm
4. R. Hyspler, S. Crhova, J. Gasparic, Z. Zadak, M. Cizkova, and V. Balasova, "Determination of isoprene in human expired breath using solid-phase microextraction and gas chromatography-mass spectrometry", *Journal of Chromatography B-Analytical Technologies in the Biomedical and Life Science*s, 2000. **739**(1): p. 183-190.
5. T. Karl, P. Prazeller, D. Mayr, A. Jordan, J.R. Rieder Fall, W. Lindinger, "Human breath isoprene and its relation to blood cholesterol levels: new measurements and modeling", *J. Appl. Physiol.* **91,** (2001)**,** 762–770.
6. H.E. Lebovitz, "Diabetic Ketoacidosis", *The Lancet*, **25**, (1995), 767-772.
7. http://www.elmhurst.edu/~chm/vchembook/624diabetes.html
8. A.D. Smith, J.O. Cowan, S. Filsell, C. McLachlan, G. Monti-Sheehan, P. Jackson D.R. Taylor, "Diagnosing asthma: comparisons between exhaled nitric oxide measurements and conventional tests", *Am. J. Resp. Crit. Care Med.* **169,** (2004), 473–478.
9. T.H. Risby, S.S. Sehnert, "Clinical application of breath biomarkers of oxidative stress status", *Free Rad. Biol. Med.* **27,** (1999), 1182–1192.

10. S.M. Studer, J.B. Orens, I. Rosas, J.A. Krishman, K.A. Cope, S. Yang, J.V. Conte, P.B. Becker, T.H. Risby, “Patterns and significance of exhaled-breath biomarkers in lung transplant recipients with acute allograft rejection”, *J. Heart Lung Transplant.* **20**, (2001), 1158–1166.

CHAPTER 6

Discussion

6.1 WO_3 Polymorphic Sensors:

WO_3 stabilizes in various crystal structures as discussed in chapter 1 that are all modifications of the cubic ReO_3 structure. Of these the monoclinic and the orthorhombic polymorphs are isostructural in that their crystal structures share the same structural elements. The main aim of the study was to establish selectivity in gas sensors based on the crystal structure.

Table 6.1 lists a set of selected publications that discuss in detail the gas sensing properties of nanostructured WO_3 towards NO_2, the common fabrication mechanisms and the concentrations of NO_2 tested for.

Table 6.1: Existing literature on the gas sensing properties of WO_3 towards NO_x (A '*' next to an interfering gas means a positive interference while its absence indicates that there was no interference. 'NA' implies that no cross sensitivity studies have been made)

Form	Method	Concentration of NO_2	Interference from	Reference
Nanowires	Thermal Evaporation	0.01ppm-1ppm	H_2S (*)	1
	Electrospinning	10ppm-50ppm	N/A	2

Thin Films	Wet Chemistry & Sol-gel	0.5 ppm 3ppm 0.05-0.55ppm 0.2-2ppm 10-30ppm 0.1-1ppm	CO H_2 (*) NA H_2S NA CO	3 4 5 38 7 8
	Physical & Chemical Methods (Sputtering, Laser Ablation, PLD, Evaporation etc)	1-10 ppm 1-10ppm (V_2O_5) 3ppm (Au) 1-20ppm 200ppm(Au/Pd) 0.1-1ppm 0.1-0.7ppm 10-500ppm 0.07-0.3 ppm	CH_3COCH_3(*),C_2H_5OH(*), NH_3(*) NA NA CO, CH_4, C_2H_5OH (*) NA NH_3, CO NA NH_3 Isoprene	9 10 11 12 13 14 15 16 17
Thick Films	Screen Printing	10-500ppm (In)	CO(*), NH_3(*), C_2H_5OH(*)	18

As is evident from the literature, the primary development of nanostructured WO_3 gas sensors for NO_x sensing has happened in the past ten years, but still there is a lack of knowledge of the basic sensing mechanism behind NO_x sensing by WO_3.

Oxygen vacancies are found in all metal oxides and are one of the most important majority carrier donors. They also act as active sites for gas adsorption [19-20]. However in certain types of metal oxides, when a certain number of oxygen vacancies have been formed in the material, it is energetically favorable for the MO_6 octahedra to arrange themselves in to edge-sharing configuration than the usual corner sharing arrangement along certain specific crystallographic planes, known as the 'Magneli Phases' or crystallographic shear planes. The presence of CS planes leads to the formation of a series of homologous solutions indicated by the formula W_nO_{3n-1}.

These CS planes are found in high abundance in the orthorhombic polymorph though not in the monoclinic polymorph. Neither XRD nor XPS of the orthorhombic polymorph reveal the presence of any bulk non-stoichiometry. W is found in the 6+ oxidation state in both the polymorphs. Thus the CS planes are present as localized defects in the crystal and at the sensing temperature can be present on the surface of the crystal. XPS also shows that the orthorhombic polymorph has a higher density of states in the energy gap compared to the monoclinic polymorph. This is significant because of the fact that without any pretreatment or gas exposure orthorhombic WO_3 has a higher number of surface states in the energy gap.

The sensing results of the monoclinic and the orthorhombic polymorphs as discussed in chapter 3 indicate that both the polymorphs are sensitive to oxidizing gases such as O_2, NO, and NO_2 that is consistent with the hypothesis explained in chapter 1,

because they are isostructural. The sensing data also reveals that the sensing response for both NO_2 and NO is similar, although both the orthorhombic and the monoclinic polymorphs show a higher response to NO_2 than NO for same concentrations as shown in figure 6.1 and 6.2. Also the orthorhombic polymorph has higher sensitivity to both NO_2 and NO as compared to the monoclinic polymorph as shown in figure 6.3 for a given concentration.

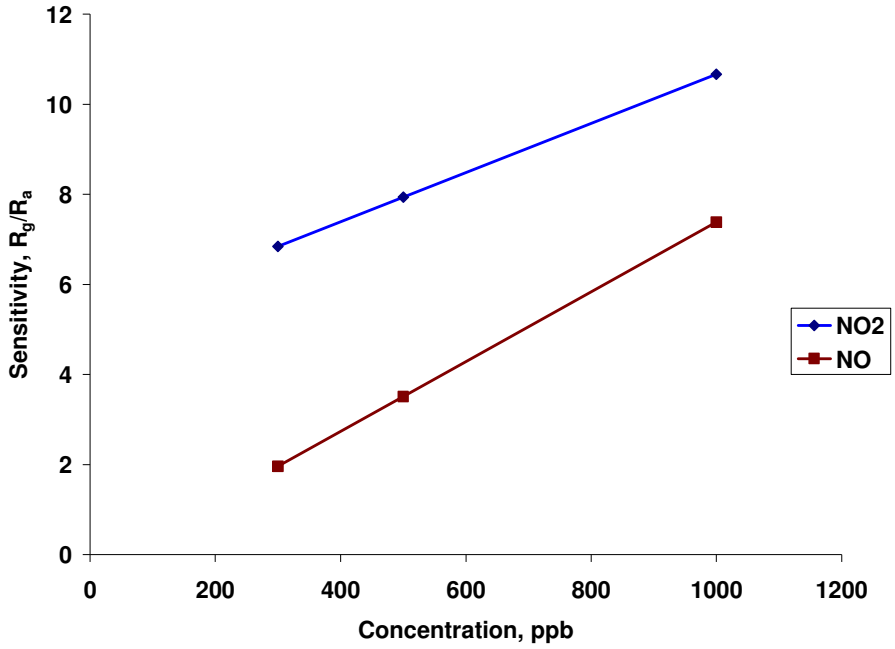

Figure 6.1: Comparison of sensitivity of the orthorhombic polymorph at 515°C to NO and NO_2

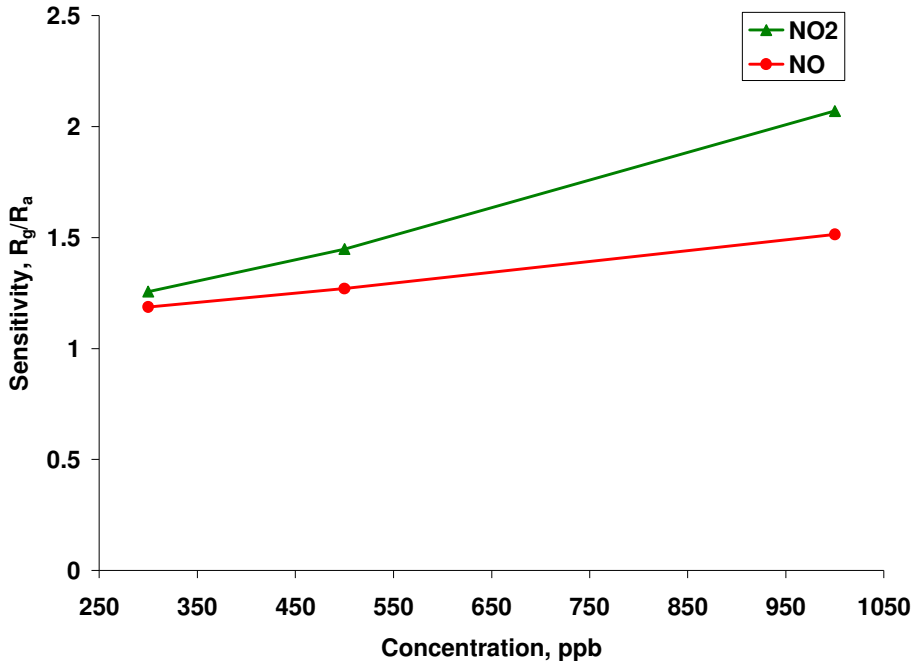

Figure 6.2: Comparison of sensitivity of the monoclinic polymorph at 400°C to NO and NO_2

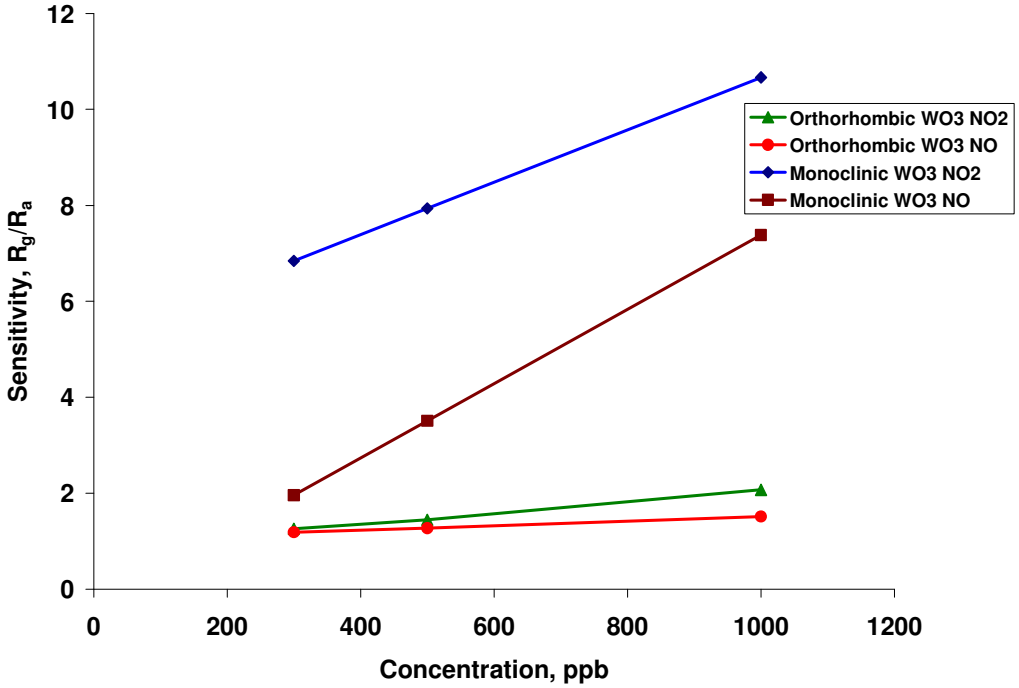

Figure 6.3: Comparison of sensitivity of the orthorhombic and monoclinic polymorphs to NO and NO_2

It is known from sensing literature that the mechanism behind the sensitivity towards oxidizing gases in WO_3, arises from the re-oxidation of oxygen vacancies and is dominated by adsorption based sensing mechanism that does not affect the bonds on the metal oxide surface. The formation of oxygen vacancies can be represented by the following quasi chemical reaction [21-22].

$$O_o^{*} \leftrightarrow \tfrac{1}{2} O_2 (g) + V_o^{2+} + 2 e^{-} \qquad (6.1)$$

Where O_o^{*} represents an unstable oxygen atom in an oxygen site, V_o^{2+} represents an oxygen vacancy with double positive charge.

When oxygen is incorporated into these vacancies, a reversible reaction (6.2) occurs as shown below

$$[V_o^{2+}] + \tfrac{1}{2} O_2 \leftrightarrow O_o^{*} + 2h^{+} \qquad (6.2)$$

Reaction as represented by Equation (6.1) occurs due to increased oxygen mobility at elevated temperatures [23] or the presence of reducing atmospheres. The slightly reduced metal oxides thus formed may either undergo reoxidation through reaction represented by Equation (6.2) by gaseous oxygen or other oxidizing gases such as NO_2 which is the mechanism for adsorption based sensing.

Since the orthorhombic and monoclinic polymorph are isostructural their response to oxidizing gases are similar which is to be expected. However their behavior towards reducing gases is different.

The monoclinic polymorph does not show any cross-sensitivity to reducing gases like ethanol, acetone, isoprene and CO while the orthorhombic sensor is sensitive to these analytes. Oxides are known to be good catalysts for selective oxidation of olefins due to their ability to form CS planes [24-25]. In an extensive study [26] conducted on WO_3

catalysts as catalysts for selective oxidation of hydrocarbons it was found that the shear planes played a critical role in inserting oxygen in to the hydrocarbon molecule and thus resulting in their oxidation.

The most interesting aspect is that completely stoichiometric WO_3 cannot form new crystallographic shear planes above a certain temperature-450°C even in vacuum [27]. However already existing CS planes can grow and thus lead to incorporation of oxygen in to the hydrocarbon molecule. Thus CS planes are a very important geometrical entity in the catalytic oxidation of hydrocarbons.

The terminations of CS planes are considered as dislocation loops and they are regions of very high elastic strain energy [28]. It is this high strain energy that accounts for the high reactivity of dislocations and probably also is the reason for the enhanced reduction/oxidation ability of the CS plane terminations. This is also one of the reasons why CS plane nucleation in WO_3 cannot occur below 450°C as CS plane nucleation will result in considerable lattice strain.

The mechanism of oxygen insertion as explained in [6] is illustrated in figure 6.4

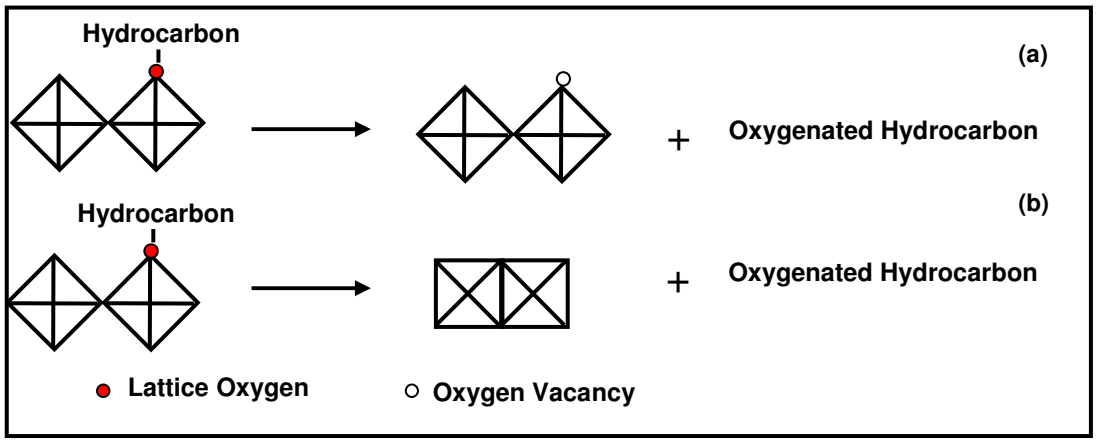

Figure 6.4: Role of CS planes in hydrocarbon oxidation; (a) an oxide that is unable to form CS planes has to oxidize the hydrocarbon by creating a new vacancy, while (b) an oxide that can form or has existing CS planes can oxidize the hydrocarbon at a much lower energy.

In an oxide where CS planes are energetically difficult to form or don't exist the oxygenation of the oncoming hydrocarbon must result in the formation of an oxygen vacancy. This process is energetically expensive. However, those oxides that have the ability to form CS planes, or grow the existing CS planes ensure that the nearest neighborhood co-ordination is maintained for the cation, while allowing oxygen abstraction from the lattice [26].

Thus the presence of CS planes plays a very important role in determining selectivity of the oxide. *The monoclinic polymorph with no CS planes and also its inability to nucleate CS planes is not sensitive to reducing gases. On the other hand the*

orthorhombic polymorph with CS planes that can grow and insert oxygen atoms in to the oncoming reducing gas, through a reaction based sensing mechanism loses its selectivity.

The same CS planes that destroy the selectivity of orthorhombic WO_3 also increase the sensitivity of the orthorhombic polymorph to NO and NO_2 as shown in figure 6.2. They act as active sites [29-30] that promote the adsorption of NO_x hence interrupting normal electrical pathways.

Two polymorphs that are isostructural thus exhibit two completely different sensing mechanisms. The monoclinic polymorph shows adsorption based sensing, while the orthorhombic polymorph exhibits reaction based sensing.

6.2 MoO_3 Nanowires:

Previous work in our laboratory shows the MoO_3 is a very selective sensor for amines. The sensing mechanism is reaction based, in the sense that upon exposure to NH_3, MoO_3 surface is reduced to form shear structures, resulting in oxygen loss from the material [31]. Thus NH_3 is particularly well-sensed by those oxides that have the ability to lose lattice oxygen easily. Following our earlier work on MoO_3 sol-gel sensors, this work explores the use of metal oxides with reduced dimensionality. One dimensional nanomaterials have a higher surface area to volume ratio when compared to equiaxed, polycrystalline grains and hence gas sensors using metal oxide nanowires or nanobelts are expected to have higher sensitivities.

It was observed in chapter 4, that the nanowire mats exhibit increased sensitivity to NH_3 as compared to the MoO_3 sol-gel thin film sensors. The ratio of total surface

areas of a nanowire mat to an equiaxed grain film of the same materials is calculated as follows [32]:

For the same volume '*V*' of the material (nanowires and nanoparticles) deposited, the individual number of nanowires (NW) and nanoparticles (NP) may be calculated as,

$$N_{NW} = V / V_{NW} \qquad (1)$$

$$N_{NP} = V / V_{NP} \qquad (2)$$

where, N_{NW} is the number of nanowires, N_{NP} is the number of nanoparticles, V is the total volume, V_{NW} is the volume of the individual nanowire (given by, $\pi r^2 l$, where '*r*' is the radius of the nanowire, '*l*' is the length of the nanowire, assumed to be rod-like), V_{NP} is the volume of the individual nanoparticle (given by $\left(4/3\right)\pi r^3$, where '*r*' is the radius of the equiaxed nanoparticle, that is assumed to be spherical).

Thus the ratio of number of nanowires to number of nanoparticles in the same volume is given by,

$$N_{NW} / N_{NP} = \left(V / V_{NW}\right) \Big/ \left(V / V_{NP}\right)$$

Therefore, $N_{NW} / N_{NP} = V_{NP} / V_{NW} = \left(4/3\right) * 10^{-3}$

(For these nanoarchitectures, '*l*' is assumed to be of the order of microns, '*r*' is assumed to be of the order of nanometers)

Now, the total surface area (SA) of the nanowires is given by the product of the surface area of an individual nanowire (SA_{NW}, given by, $2\pi r(r+l)$) and N_{NW}. Similarly for the nanoparticles the total surface area is equal to the product of the surface area of the individual nanoparticles (SA_{NP}, given by $4\pi r^2$) and N_{NP}.

Therefore the ratio of total surface areas of the nanowire to the nanoparticle is given by

$$\left(SA_{NW} * N_{NW} \Big/ SA_{NP} * N_{NP} \right) = \left(l \Big/ 2r \right) * 10^{-3} \qquad (3)$$

where '*l*' represents the length of the nanowire and '*r*' represents the radius of the nanostructure (in the case of the nanowire the assumed shape is a rod, and in the case of the equiaxed nanoparticle the assumed shape is a sphere). The radius of both structures is assumed to be identical for calculation purposes.

In comparing the two structures it is evident that for a given volume the number of nanoparticles is higher than the number of nanowires produced. However, the total surface area of a fixed volume of nanowires is considerably higher than the total surface area of the same volume of nanoparticles. The surface area to volume ratio has a direct dependence on the length '*l*' of the nanowires. As '*l*' in (2) increases the ratio of the total surface areas of the nanowires to the nanoparticles increases linearly.

The length '*l*' for the MoO_3 nanowires produced is of the order of 1-2 μm. Thus the surface area to volume ratio is only 1-10 times higher than that of the sol-gel

precursor. Secondly, the pre-spinning solution used to prepare the nanowire mats consists of maximum 20% metal oxide. While the molarity of both solutions remains the same, the dilute hybrid (sol-gel – polymer) precursor is only a quarter of the concentration of the metal oxide sol-gel used to produce the nanocrystalline thin films. Thus the yield of nanowires obtained in the calcined mat available for NH_3 sensing is significantly less than the number of nanoparticles used in the MoO_3 sol-gel sensor. Still, the results obtained are impressive considering the type of applications envisioned for these sensors

6.3 Sensor Arrays:

The highest sensitivity of the rutile based sensors is towards ethanol and methanol with sensitivities of 0.04 and 0.5 respectively. For the same concentration of ethanol and methanol, ethanol produces an order of magnitude higher response than methanol. Thus low molecular weight alcohols can be sensed with very high sensitivities using the rutile based sensors.

The main sensing mechanism behind the hydrocarbon sensing is explained as follows. As explained in chapter 1 the surfaces of metal oxides are covered with adsorbed oxygen from the atmosphere and the resulting electron transfer results in the formation of ionized oxygen species O^- or O_2^-. The dominating species of the oxygen ion is dependent on temperature. O_2^- is usually present on the surface at lower temperatures while the more dissociated O^- species is found at elevated temperatures [33]. The reaction kinetics can be explained by the following series of reactions.

$$O_2 \text{ (gas)} \rightarrow O_2 \text{ (adsorbed)}$$

$$O_2 \text{ (adsorbed)} + e^- \rightarrow O_2^-$$

$$O_2^- + e^- \rightarrow 2O^-$$

The method of dissociation and hence the ease with which electrons will be released is intricately linked to temperature, the crystal structure of the metal oxide and the nature of the gas itself. In the case of hydrocarbons the reducing hydrogen molecules are bound to the carbon atoms and thus the dissociation is more complicated compared to other reducing gases like carbon monoxide [34]. The sensing temperature has to be carefully controlled in order not to burn the hydrocarbons completely at higher temperatures, but also not too low that will not let the dissociation products desorb from the metal oxide surface. Thus an optimum temperature of 400°C was chose for the rutile based MoO_3-TiO_2 based hybrid sensors.

It can be seen that the response of the hybrid sensors to acetone and isoprene is almost identical. Isoprene also known as 1,3-butadiene reacts with rutile surfaces by forming a $OH^{\cdots}\pi$ electron complex [35]. Similarly acetone also reacts with the rutile surface by forming a hydrogen hydroxyl bond. This might explain the sensor similarity of the two gases.

For the alcohols the sensing mechanism can be expressed as follows.

$$C_2H_5OH + O^- \rightarrow CH_3CHO + H_2O + e^-$$

In the case of ethanol and methanol the reducing hydrogen atom is more readily available as compared to acetone in which the following kinematic reactions have to occur in order to release the electrons bound to the ionized oxygen.

$$CH_3COCH_3 \text{ (gas)} + O^- \rightarrow CH_3^+CO + CH_3O^- + e^-$$

$$CH_3CO^+ \rightarrow CH_3^+ + CO$$

$$CO + O^- \rightarrow CO_2 + e^-$$

These complicated dissociation of acetone and isoprene somewhat reduces the sensitivity of the rutile hybrid sensors towards acetone and isoprene.

The sensing mechanism behind CO is one of the most straight forward. CO gets oxidized to CO_2 on the surfaces of metal oxides and in the process releases the electron bound to the oxygen atom in to the conduction band of the metal oxide as shown below.

$$CO + O^- \Leftrightarrow CO_2 + e^-$$

The rutile surfaces thus provide active sites for easy oxidation of the reducing gases and are thus very selective towards reducing gases such as volatile organic compounds and hydrocarbons. Thus a sensor array with only three elements, each belonging to one class of metal oxides can distinguish three different types of gases.

References:

1. A. Ponzoni, E. Comini, G. Sberveglieri, J. Zhou, S.Z. Deng, N.S. Xu, Y. Ding and Z.L. Wang, "Ultrasensitive and highly selective gas sensors using three-dimensional tungsten oxide nanowire networks", *Appl. Phys. Lett*. **88**, (2006), p. 203101-1-203101-3.
2. K.M. Sawicka, A.K. Prasad and P.I. Gouma, "Metal oxide nanowires for use in chemical sensing applications", *Sens. Lett.* **3**, (2005), p. 31-35.
3. M. Blo, M.C. Carotta, S. Galliera, S. Gherardi, A. Giberti, V. Guidi, C. Malagu, G. Martinelli, M. Sacerdoti, B. Vendemiati and A. Zanni, "Synthesis of pure and loaded powders of WO_3 for NO_2 detection through thick film technology", *Sens. Actuator B-Chem.* **103**, (2004), p. 213-218.
4. L.G. Teoh, Y.M Hon, J. Shieh, W.H. Lai and M.H. Hon, "Sensitivity properties of a novel NO_2 gas sensor based on mesoporous WO_3 thin film", *Sens. Actuator B-Chem*. **96**, (2003), p. 219-225.
5. S.H. Wang, T.C. Chou and C.C. Liu, "Nano-crystalline tungsten oxide NO_2 sensor", *Sens. Actuator B-Chem*. **94**, (2003), p. 343-351.
6. I. Jimenez, J. Arbiol, G. Dezanneau, A. Cornet, and J.R. Morante, "Crystalline structure, defects and gas sensor response to NO_2 and H_2S of tungsten trioxide nanopowders", *Sens. Actuator B-Chem.* **93**, (2003), p. 475-485.
7. D.S. Lee, S.D. Han, J.S. Huh and D.D. Lee, "Nitrogen oxides-sensing characteristics of WO_3-based nanocrystalline thick film gas sensor", *Sens. Actuator B-Chem.* **60**, (1999), p. 57-63.

8. V. Guidi, M. Blo, M.A. Butturi, M.C. Carotta, S. Galliera, A. Giberti, C. Malagu, G. Martinelli, M. Piga, M. Sacerdoti and B. Vendemiati, "Aqueous and alcoholic syntheses of tungsten trioxide powders for NO_2 detection", *Sens. Actuator B-Chem*. **100**, (2004), p. 277-282.

9. P. Ivanov, M. Stankova, E. Llobet, X. Vilanova, J. Brezmes, I. Gracia, C. Cane, J. Calderer and X. Correig, "Nanoparticle metal-oxide films for micro-hotplate-based gas sensor systems", *IEEE Sens.* J. **5**, (2005), p. 798-809.

10. X. He, J. Li, X. Gao, "Effect of V_2O_5 coating on NO_2 sensing properties of WO_3 thin films", *Sens. Actuator B-Chem*. **108**, (2005), p. 207-210

11. C.J. Jin, T. Yamazaki, Y. Shirai, T. Yoshizawa, T. Kikuta, N. Nakatami and H. Takeda, "Dependence of NO_2 gas sensitivity of WO_3 sputtered films on film density", *Thin Solid Films* **474**, (2005), p. 255-260.

12. P. Nelli, L.E. Depero, M. Ferroni, S. Groppelli, V. Guidi, F. Ronconi, L. Sangaletti and G. Sberveglieri, "Sub-ppm NO_2 sensors based on nanosized thin films of titanium-tungsten oxides", *Sens. Actuator B-Chem.* **31**, (1996), p. 89-92.

13. H. Kawasaki, T. Ueda, Y. Suda and T. Ohshima, "Properties of metal doped tungsten oxide thin films for NO_x gas sensors grown by PLD method combined with sputtering process", *Sens. Actuator B-Chem.* **100**, (2004), p. 266-269.

14. A. Ponzoni, E. Comini, M. Ferroni and G. Sberveglieri, "Nanostructured WO_3 deposited by modified thermal evaporation for gas-sensing applications", *Thin Solid Films* **490**, (2005), p. 81-85.

15. C. Cantalini, "Cr_2O_3, WO_3 single and Cr/W binary oxide prepared by physical methods for gas sensing applications", *J. European Ceram.* Soc. **24**, (2004), p. 1421-1424.

16. A.K. Prasad and P.I. Gouma, "MoO_3 and WO_3 based thin film conductimetric sensors for automotive applications", *J. Mater. Sci.* **38**, (2003), p. 4347-4352.

17. B. Fruhberger, N. Stirling, F.G. Grillo, S. Ma, D. Ruthven, R.J. Lad and B.G. Frederick, "Detection and quantification of nitric oxide in human breath using a semiconducting based chemiresistive microsensor", Sens. Actuator B-Chem. **76**, (2001), p. 226-234.

18. V. Khatko, E. Llobet, X. Vilanova, J. Brezmes, J. Hubalek, K. Malysz, X. Correig, "Gas sensing properties of nanoparticle indium-doped WO3 thick films", Sens. Actuator B-Chem. **111**, (2005), p. 45-51.

19. M. Ivanovskaya, P. Bogdanov, G. Fagila, G. Sberveglieri, "The features of thin film and ceramic sensors at the detection of CO and NO_2", *Sens. Actuators B* **68**, (2000), 344-350.

20. L. Francioso, A. Forleo, S. Capone, M. Epifani, A.M. Taurino, P. Siciliano, "Nanostructured In_2O_3-SnO_2 thin film as material for NO_2 detection", *Sens. Actuators B* **114**, (2006), 646-655.

21. A.K. Prasad, D. Kubinski, and P.I. Gouma, "Comparison of sol–gel and ion beam deposited MoO_3 thin film gas sensors for selective ammonia detection", *Sens. and Actuators B-Chem.* **93,** (2003), 25-30.

22. H. Yamada and G.R. Miller, "Point-Defects in Reduced Strontium-Titanate*", J. Solid State Chem.* **6,** (1973), 169-177.

23. M.A. Khilla, Z.M. Hanafi, B.S. Farag, and A. Abuelsaud, "Transport-Properties of Molybdenum Trioxide and Its Suboxides" *Thermochim. Acta*, **54**, (1982), 35-45.

24. B. Grzybowska, J. Haber, J. Janas, "Interaction of allyl iodide with molybdate catalysts for selective oxidation of hydrocarbons", *J. Catal.*, **49**, (1977), 150-163.

25. J. Haber, W. Marczewski, J. Stoch, L. Ungier, "Electron spectroscopic studies of reduction of MoO_3", *Ber. Bunsenges. Phys. Chem.* **79**, (1975), 970-974.

26. J. Haber, J. Janas, M. Schiavello, R.J.D. Tilley, "Tungsten oxides as catalysts in Selective Oxidation", *J. Catal*. **82**, (1983), 395-403.

27. J. Booth, T. Ekström, E. Iguchi, R.J.D. Tilley, "Notes on phases occurring in the binary tungsten-oxygen system", *J. Solid. State. Chem.* **41**, (1982), 293-307.

28. J.S. Anderson, B.G. Hyde, "On possible role of dislocations in generation ordered and disordered shear structure", *J. Phys. Chem. Solids* **28**, (1967), 1393.

29. L. Chen, S. C. Tsang, "Ag-doped WO_3-based powder sensor for the detection of NO gas in air", *Sens. Actuators. B Chem.* **89**, (2003), 68-75.

30. C.S. Rout, K. Ganesh, A. Govindaraj, C.N.R. Rao, "Sensors for the nitrogen oxides, NO_2, NO and N_2O based on In_2O_3 and WO_3 nanowires", *Appl. Phys. A.* **85**, (2006), 241-246.

31. Arun Kapaleeswaran Prasad, "Study of gas specificity in MoO_3/WO_3 thin film sensors and their arrays", Ph.D. Thesis, SUNY Stony Brook, NY, (2005).

32. P.I. Gouma, K. Kalyanasundaram, A. Bishop, “Electrospun single crystal MoO_3 nanowires for biochem sensing probes”, *J. Mater. Res.* **21**, (2006), 2904-2910.

33. N. Barsan, U. Weimar, “Conduction model of metal oxide gas sensors”, *J. Electrocerm.* **7**, (2001), 143-167.

34. R.S. Khadayate, J.V. Sali, P.P. Patil, ”Acetone vapor sensing properties of screen printed WO_3 thick films”, *Talanta,* **72**, (2007), 1077-1081.

35. A. Teleki, S.E. Pratsinis, K. Kalyanasundaram, P.I. Gouma, ”Sensing of organic vapors by flame made TiO_2 nanoparticles”, *Sens. Actuators. B-Chem.* **119**, (2006), 683-690.

CHAPTER 7

Conclusions and Future Work

In this thesis, it has been demonstrated that the crystallographic configuration of a given metal oxide determines its specificity towards a particular gas or class of gases. In particular, 3 key points have been made:

1. The effect of crystallographic shear/localized non-stoichiometry in ReO_3 type structures of WO_3 for selective detection of oxidizing gases
2. Role of reduced dimensionality and the use of nanowires in increasing sensor sensitivity in MoO_3 structures specific to ammonia detection.
3. Use of sensor arrays utilizing rutile based sensing elements for selective detection of hydrocarbons

This is the first effort to correlate gas sensing to oxide crystallography and it is similar to studies of metal/ gas interaction that have been useful in catalysis.

7.1 Summary of Conclusions:

WO_3 polymorphs:

Tungsten oxide which is modified ReO_3 based perovskite exists in multiple modifications. Two of them namely monoclinic and orthorhombic which are isostructural were examined for their sensitivity towards oxidizing gases like nitrogen oxides. Tungsten oxide films were synthesized using the sol-gel method. By carefully choosing the heat treatment temperatures (400°C for monoclinic and 515°C for orthorhombic),

specific crystal structures in the sensing matrix were achieved. XRD and TEM revealed that both the polymorphs were nanostructured. High resolution transmission electron microscopy revealed the presence of bulk lattice defects called the "Crystallographic shear (CS) planes" or "Magneli phases" in the orthorhombic polymorph, whereas the monoclinic polymorph did not exhibit these features. The presence of these defects was also confirmed by XPS that showed a higher density of states in the forbidden energy gap of the orthorhombic polymorph as compared to the monoclinic polymorph. The presence of these defects did not affect the bulk stoichiomtery of the crystal which was also confirmed by XPS, as W atoms were found in their highest oxidation state in both the polymorphs. Thus these defects exist as localized regions in the crystal.

Gas sensing experiments carried out on both polymorphs revealed that the monoclinic polymorph is selective to oxidizing gases such as O_2, NO_2 and NO, while the selectivity of the orthorhombic polymorph is destroyed. It shows cross-sensitivity to reducing gases such as ethanol, acetone, isoprene and CO. Both the polymorphs show excellent sensitivity towards NO and NO_2 for concentrations as low as 300 ppb.

A detailed analysis revealed that the presence of CS planes plays a very significant role in destroying the selectivity of the orthorhombic sensor. The presence of CS planes changes the sensing mechanism of the orthorhombic polymorph from *adsorption based to reaction based.* Adsorption based sensing mechanism is responsible for the sensitivity of the WO_3 sensors towards NO_x and oxygen, while the reaction based mechanism comes in to play for the reducing gases.

Thus although both the polymorphs were isostructural, presence of unique structural features altered the sensing behavior of one of the polymorphs.

MoO_3 Nanowires:

MoO_3 has a unique crystal structure, with layered MO_6 octahedra, which makes it selective to amines such as ammonia, due to its ability to easily lose lattice oxygen. The primary aim of this work was to analyze the effect of the metal oxide nanocrystal morphology and dimensions, on the gas sensitivity.

Electrospinning, a unique method to fabricate nanostructures in a single step process was employed to synthesize MoO_3 nanowires. Based on thermal analysis of the metal oxide, the metal oxide/polymer nanofiber composite mat was calcined at 500°C in order to achieve orthorhombic crystal structure in the nanowires. It was found that a careful control of the electrospinning processing parameter and the amorphous nature of the starting metal oxide played a very important role in the evolution of the crystal structure of the nanowires. TEM analysis of the calcined nanowires revealed that they were single crystals with specific crystal structure orientations, unique to MoO_3.

Gas sensing experiments were carried out to compare the sensing behavior of the nanowires to a sol-gel sensor. It was found that for the same concentration of NH_3 the nanowire sensor exhibited an order of magnitude higher sensitivity than a MoO_3 sensor composed of equiaxed, polycrystalline grains.

Empirical calculations revealed that the ratio of the surface areas of the nanowires to nanocrystalline grains scales by a ratio as shown below

$$\left(SA_{NW} * N_{NW} \Big/ SA_{NP} * N_{NP} \right) = \left(l \Big/ 2r \right) * 10^{-3}$$

where '*l*' is the length of the nanowires, '*r*' is both the radius of the nanowire and the equiaxed grain diameter. Thus the surface area of the nanowires scales directly as the

length of the nanowires. For a 100μm long nanowire the sensitivity will be 100 times compared to that of a similar sensor composed of equiaxed, polycrystalline grains.

Sensor Arrays and Prototype device:

The sensor array built of sensing elements based on three different types of pure nanostructured metals oxides namely, rutile based MoO_3-TiO_2, modified perovskite based WO_3 and monoclinic MoO_3, was used to selectively detect hydrocarbons and NO_x es. The rutile based elements are selective towards hydrocarbons while the modified perovskite based elements are selective towards nitrogen oxides.

Commonly used electronic noses use non-selective sensors which require the use of a pattern recognition algorithm to recognize the odor. By using a smaller number of selective sensors, the need for pattern recognition and excessive calibration can be eliminated. This sensor array composed of three classes of metal oxides can distinguish three different types of gases.

An important aim of this thesis was to develop a portable breath analyzer device, based on the selective gas sensors developed, for detection of specific metabolites in breath like NO, NH_3 and isoprene.

In collaboration with electrical engineering department and the University's Medical School we have been able to develop a prototype of the final breath analyzing device. The components of the device, shown in the figure 7.1, are a) the mouthpiece, b) *the NaOH filter (which can contain a desiccant, if removal of humidity is necessary)* c) the Sensor, d) the Acquisition Module, which converts the sensor signal into digital

value, e) the Memory/Computation Module, which contains a predetermined threshold value for the binary response, and f) the Display Unit

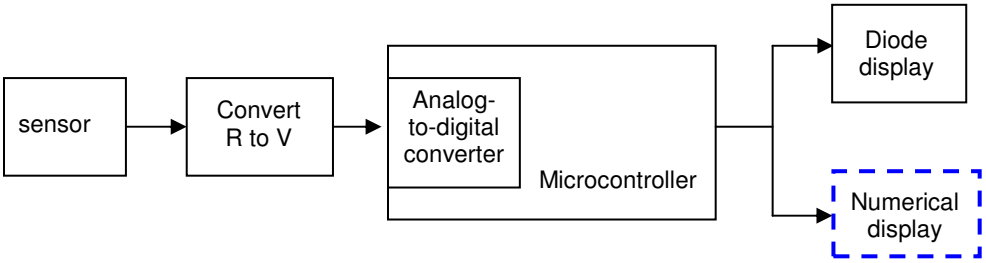

Figure 7.1: Flow-chart of the prototype schematic

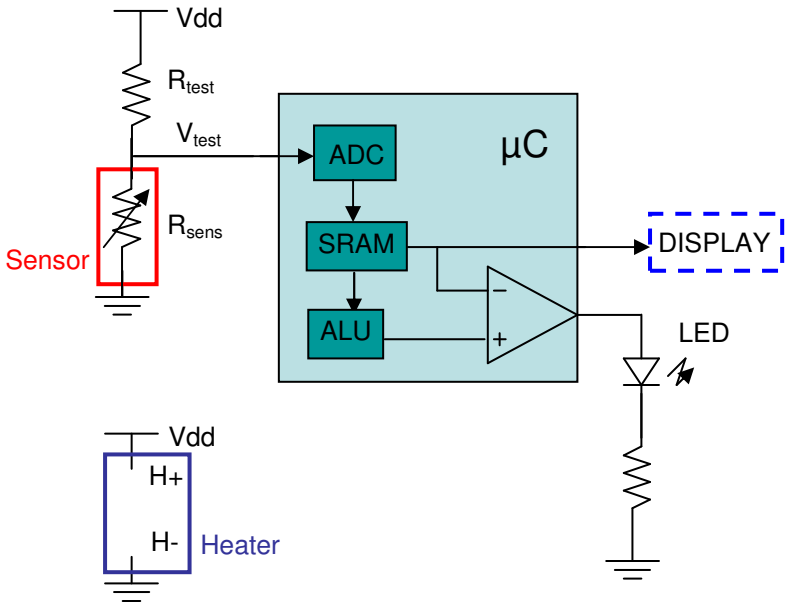

Figure 7.2: The electronic circuitry of the device. The sensor and interface circuitry and display are depicted. The microcontroller (µC) contains the Analog-to-Digital Converter (ADC), memory (SRAM), and an Arithmetic Logic Unit (ALU). V_{test}: Voltage proportional to the resistance of the sensor.

The conductance of the sensor is proportional to gas concentration. Thus to sense the concentration of any analyte, the resistance of the sensor is first converted to a voltage signal. After the first (baseline) breath test, the voltage signal is converted through an analog-to-digital converter to a digital value, which will then be compared to a predefined threshold value. The threshold voltage value would be set through calibration measurements and stored as a digital value in the microcontroller. This gives rise to a binary 'YES/NO' response. Depending on the analyte the specific LED goes off indicating that the concentration of the analyte has exceeded the threshold value. This can serve as a 'cut-off' sensor for pre-screening of patients with specific diseases.

7.2 Future research directions:

- Spectroscopic evaluation of the sensing mechanism: Preliminary in-situ FTIR experiments have been carried out on both the polymorphs for NO and ethanol at the sensing temperature. Initial evaluation of the spectroscopic data reveals fundamental differences in the positions of the vibrational frequencies and intensities for both the gases. There is a lack of sufficient data for WO_3 surface in the catalysis literature for NO and ethanol. Detailed analysis of the evolution of the surface reactions with respect to temperature and the polymorph needs to be carried out, in order to exactly understand the reaction products from the surface interaction.
- Temperature Programmed Desorption (TPD) experiments give valuable information on the formation and desorption of reaction products on the surface. Controlled TPD experiments, at the sensing temperatures need to carried out for both the

polymorphs for understanding the surface chemistry. This in addition to In-situ FTIR experiments can help build a useful database for establishing the exact reaction paths for specific analytes, and also help understand the difference between the polymorphs better.

- The presence of crystallographic defects such the CS planes affects the sensing mechanism of the WO_3 based sensors. A quantitative study that links the presence of these defects and the density of states in the energy gap with the sensitivity of the sensors has to be done. A detailed XPS study before and after sensing of all gas analytes would confirm the reaction mechanism with those gases. An in-situ XPS with gas atmosphere control would give better idea as to what happens to the electronic structure of the metal oxide during high temperature gas interaction and also an idea of how the shear planes grow and whether this leads to an increase in the density of states in the gap. This in turn can be correlated to the Fermi level movement (pinning/unpinning) in the polymorphs.
- The prototype device has to be improved in terms of its adaptability for using a numerical display (outlined in blue in the figure 7.1 and 7.2), for displaying the exact concentration of the analyte, in addition to the binary response. This can then be compared to standard concentrations of analytes commonly found in human breath to give a clinical diagnosis.
- A recent call for proposals from the Department of Homeland Security, wants chemical, biological and radiological detectors to be installed in cell-phones. The sensors developed in this work, would be ideal candidates for such a portable

system. These could be built with an inherent GPS system to transmit the location of the hazard, and also a RF transmitter that is connected with the DHS's database.

- Appendix I explains the work carried out at NIMS, Japan. It involves the development of a metastable form of WO_3, with a radically different crystal structure that is similar to the layered MoO_3 structure. This structural similarity makes it a very interesting candidate for selective amine sensing and also the possibility of using it as an intercalation host for Li^+ ion batteries.

APPENDIX I

Hexagonal-WO_3

This appendix discusses the synthesis and characterization of a new form of WO_3 namely, hexagonal WO_3 from a substoichiometric metal alkoxide precursor-tungsten (V) isopropoxide, by a novel colloidal synthesis. Three different nanostructures were observed in the resulting material- nanowires, hexagonal nanoplatelets/nanosheets and nanoparticles. X-ray diffraction, Scanning electron microscopy and Transmission electron microscopy have been carried out to characterize the crystal structure and also to assess the growth mechanism. It has been found that the non-stoichiometry of the precursor results in the formation of a metal hydrogen oxide that transforms to h-WO_3 on annealing. Hexagonal WO_3 (h-WO_3) differs from related tungsten oxides (based on a modified cubic ReO_3 crystal structure), in that it possesses unique structural features such as long, hexagonal prism channels parallel to the *c*-axis and layered oxygen octahedra making it a very attractive host matrix for metal ion intercalation for rechargeable batteries and also a selective gas sensor.

Tungsten trioxide is a well-known metal oxide that finds widespread use in gas sensing, eletrochromic and catalytic applications [1-4]. WO_3 has a very interesting set of electronic properties where it can range from being a metallic conductor (in its highly reduced state) to an insulator. Polymorphic transformations of the pseudo-cubic lattice result in this wide variation in its electronic properties. WO_3 usually crystallizes in one of

the following crystal structure modifications- triclinic, monoclinic, orthorhombic, and tetragonal. All of these polymorphs are distorted forms of a cubic ReO_3 lattice, with increasing order of crystallographic symmetry from the triclinic to tetragonal lattice. The crystal lattice is composed of a framework of metal-oxygen octahedra as depicted in Figure A1.1, where the metal atoms are located at the center of the oxygen octahedra with varying amounts of metal-oxygen bond lengths and thus varying amounts of octahedral distortion. This distortion in turn serves to stabilize the different polymorphs.

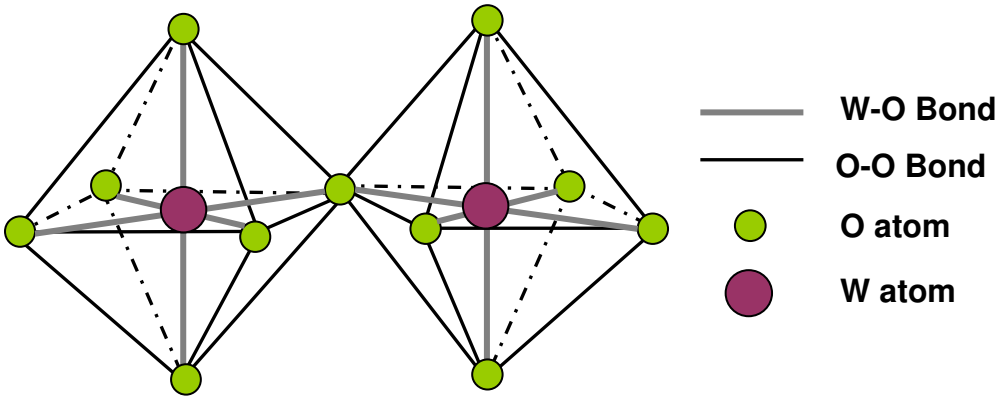

Figure A1.1: WO_6 octahedra in WO_3

Cubic WO_3 with the ideal ReO_3 lattice is difficult to obtain as a stable polymorph. The other thermodynamically metastable form of WO_3 that has been synthesized and reported [5] has a hexagonal structure. The crystal structure is unique in that the lattice is made up of rings of corner- sharing oxygen octahedra as depicted in Figure A1.2. The layered oxygen octahedra provide both triangular and hexagonal prism channels that allow for easy movement of ions or gas molecules to travel through the lattice. Tungsten bronzes frequently crystallize in a hexagonal lattice, when the hexagonal tunnels are

interpolated with specific cations [6]. But recently there have been reports of synthesis of pure h-WO_3 obtained by dehydration of an orthorhombic WO_3.1/3 H_2O precursor. Since then, there has been a lot of interest in synthesizing h-WO_3 as a matrix for intercalating metal ions for rechargeable batteries (Li^+ [7]) and electrodes. Lithium ion batteries are vital for advancing the field of portable electronics. They operate by reversibly inserting Li^+ ions from the electrolyte into the electrodes and in the process generating electricity. Reversible intercalation of Li^+ ions in to the host matrix is crucial for battery operation and can be accomplished by having electrode materials that have relatively open crystal structures [8]. Thermodynamically stable crystal structures are typically close-packed, whereas metastable oxide phases have open lattices that promote very high diffusion rates for intercalating ions.

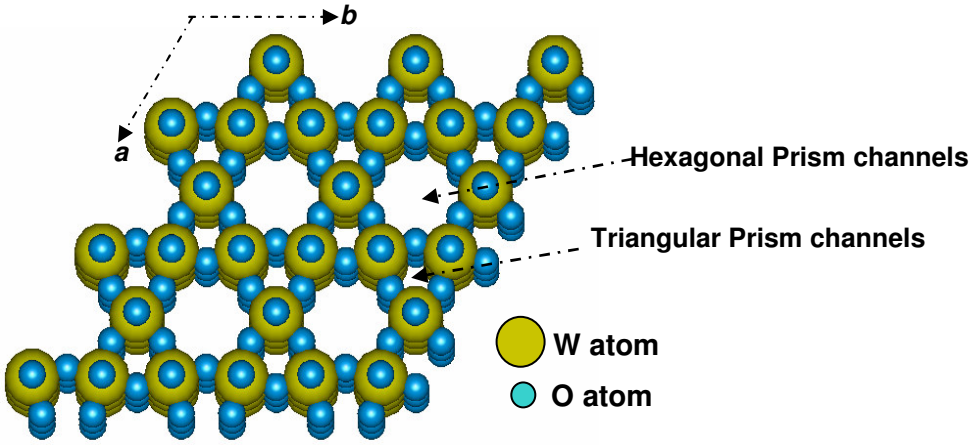

Figure A1.2: Arrangement of WO_6 octahedra in hexagonal WO_3

In the area of resistive gas sensing, the attraction of hexagonal WO_3 lies in the structural similarity it shares with the orthorhombic form of MoO_3. Both these crystal structures have layered oxygen octahedra, in other words an open lattice structure, that provides long paths for small, diffusing gas molecules and facilitates easy removal of oxygen ions from the lattice. It is evident from our earlier research that the crystal structure plays a key role in determining selectivity of the sensing matrix [9]. Orthorhombic MoO_3 has been shown to be selective to ammonia in the presence of other gases. MoO_3 with its low sublimation temperature is not a suitable candidate for prolonged use at elevated temperatures. WO_3 on the other hand has higher structural integrity than MoO_3 and hence ideal for high temperature sensor applications. Also the high aspect ratio of the nanowires will serve to improve the energy density of the batteries without increasing the effective volume of the battery.

Also, metal oxides with lower dimensionalities have been the focus of intense research activity for applications requiring high surface-area to volume ratio such as gas sensing, catalysis [10-11]. Nanotubes, nanowires, nanobelts and other one-dimensional nanostructures have most of their atoms as surface atoms, and hence provide more reaction sites for surface reactions. In particular, in the area of gas sensing the absence of a bulk can tremendously increase sensor response and recovery times.

A review of the synthetic methods for obtaining hexagonal tungsten oxide was published recently [12]. In the past couple of yeas there have been a lot of research efforts to synthesize h-WO_3 through different routes- vapor deposition [13], thermal

evaporation [14], soft chemistry [15-17] to mention a few. In this paper we report the synthesis of nanosheets, nanowires and nanoparticles of hexagonal WO_3 by simple hydrolysis and subsequent annealing of a sub-stoichiometric metal alkoxide precursor in air at a maximum temperature limit of 515°C. There has been no previous report of h-WO_3 being stable above 500°C. Above 500°C, there is an irreversible transformation to the thermodynamically stable monoclinic structure. The influence of the annealing temperature on the film morphology has also been discussed.

EXPERIMENTAL

Tungsten (V) isopropoxide was drop coated on glass substrates inside a glove box. The glass slides were ultrasonically cleaned in acetone for half-hour prior to film deposition. The films as deposited inside the glove box were translucent yellow in color and upon contact with atmospheric moisture turned a deep blue. The films, once taken out of the glove box were immediately transferred to a furnace. The films were heat treated in air at 400°C and 515°C for 6 hours and 8 hours respectively. All the films were gray-white in color after the annealing treatment.

X-Ray Diffraction (XRD) on the thin films was carried out using a Philips PW1729 X-ray diffractometer with a Cu Kα radiation (λ=1.54184Å). Scanning Electron Microscopy (SEM) on the heat treated films was carried out using a LEO GEMINI 1550 with a Schottky Field Emission Gun. The films were sputter coated with gold for 20s before SEM observation. Transmission Electron Microscopy (TEM) was performed using a Philips CM12 STEM with a LaB_6 cathode at an accelerating voltage of 120 keV. The samples for transmission electron microscopy were prepared by scraping the film off the

substrates and suspending them in ethanol. The solution was then ultrasonically agitated to achieve uniform dispersion. The solution was then drop coated on to the TEM grids. Only the sample heat treated at 515°C has been used for TEM observation since it possessed higher crystallinity than the 400°C annealed film.

RESULTS AND DISCUSSION

Figure A1.3 corresponds to the XRD pattern of the film heat treated at 400°C 515°C. The film heat treated at 400°C has not fully crystallized which can be inferred from the broad XRD peaks. All the main peaks can be indexed to match the hexagonal WO_3 corresponding to the JCPDS card number 33-1387 with unit cell dimensions of a=7.298, c=3.899.

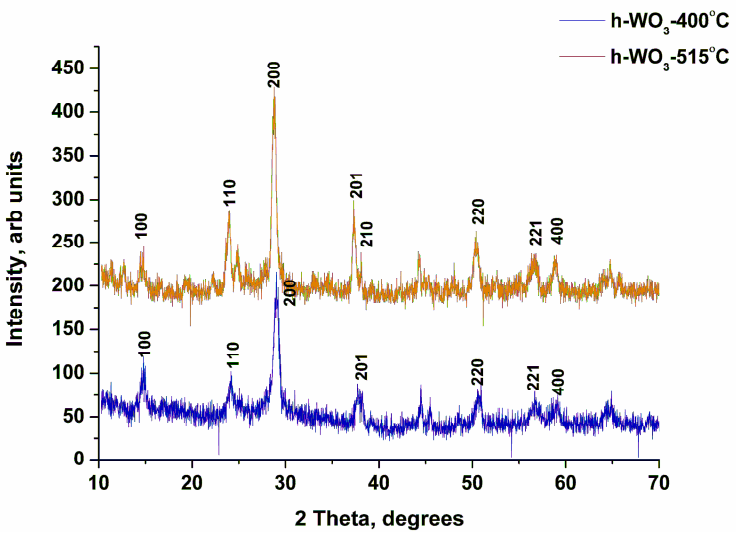

Figure A1.3: XRD spectra of the h-WO_3 samples heat treated at (a) 400°C and (b) 515°C

Neither tungsten oxide hydrate nor hydrogen tungsten oxide peaks were observed in the XRD patterns.

Figures A1.4-A1.5 show the SEM images of the films annealed at 400°C and 515°C. Both films exhibit cracking, typical of films deposited by the sol-gel method.

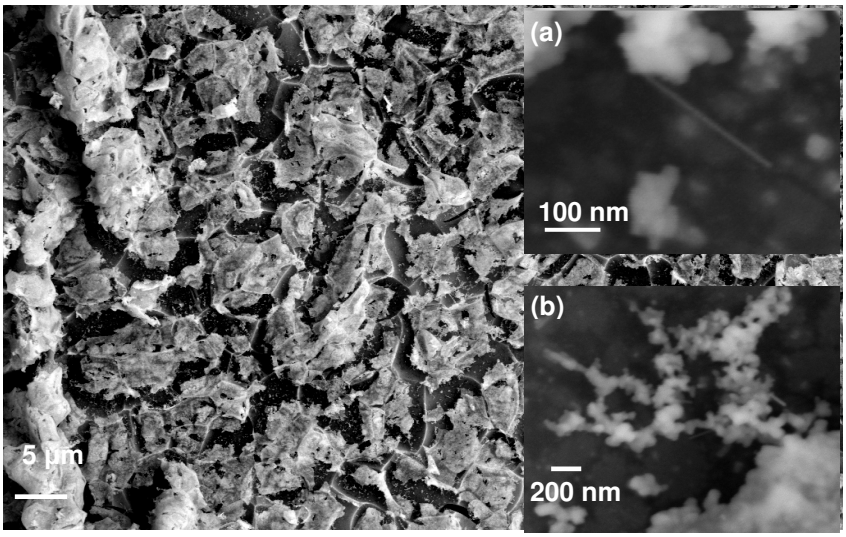

Figure A1.4: Low magnification SEM image of the sol-gel film heat treated at 400°C; (inset a) a single nanowire growing from a grain cluster; (inset b) a grain cluster on the film

The film heat treated at 400°C has not crystallized completely and is still amorphous in appearance. Some nanowires can be seen in the film annealed at 400°C also. The film heat treated at 515°C on the glass substrate possesses three distinct and different structural features – nanowires, nanosheets and nanoparticles. The nanoparticles which compose about 40% of the film area are aggregated in to bundles at some places (Figure A1.5a) and at some other places (Figure A1.5c) are present as discrete particles. The nanowires are seen growing out of the nanoparticle bundles (Figure A1.5a and A1.5b). They are about 150nm in width/diameter and are 2-5µm in length.

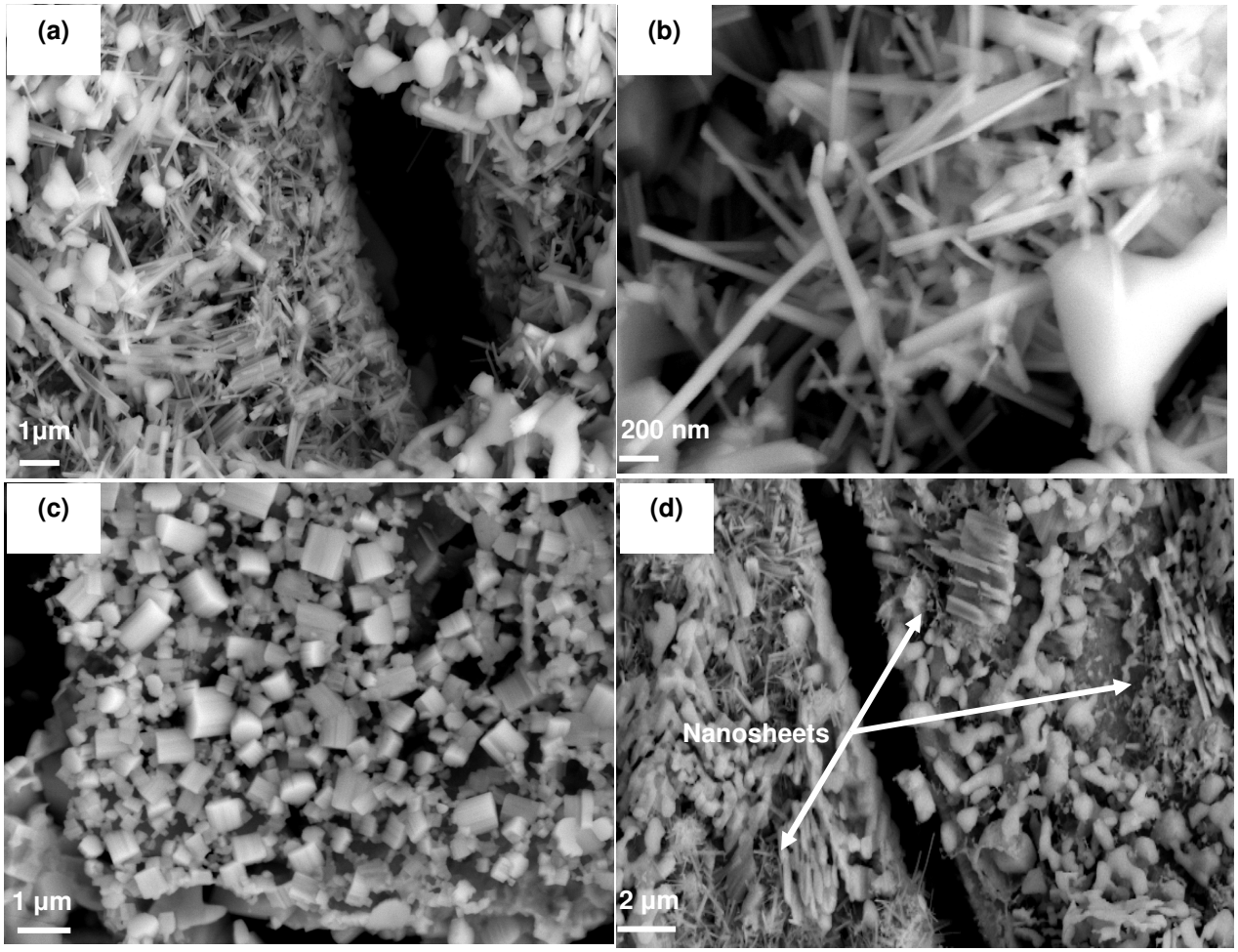

Figure A1.5: SEM image of heat treated films, (a) and (b) nanowires (c) nanoparticles and (d) nanosheet bundles

The nanosheets are also aggregated in to bundles but can be distinctly distinguished by their flat morphology as shown in Figure A1.5d. Their sheet thickness is of the order of 50-100nm. All the nanosheet bundles are oriented perpendicular to the substrate.

Figures A1.6 (a)-(c) illustrate the morphology and crystal structure of the products obtained, as observed under the TEM.

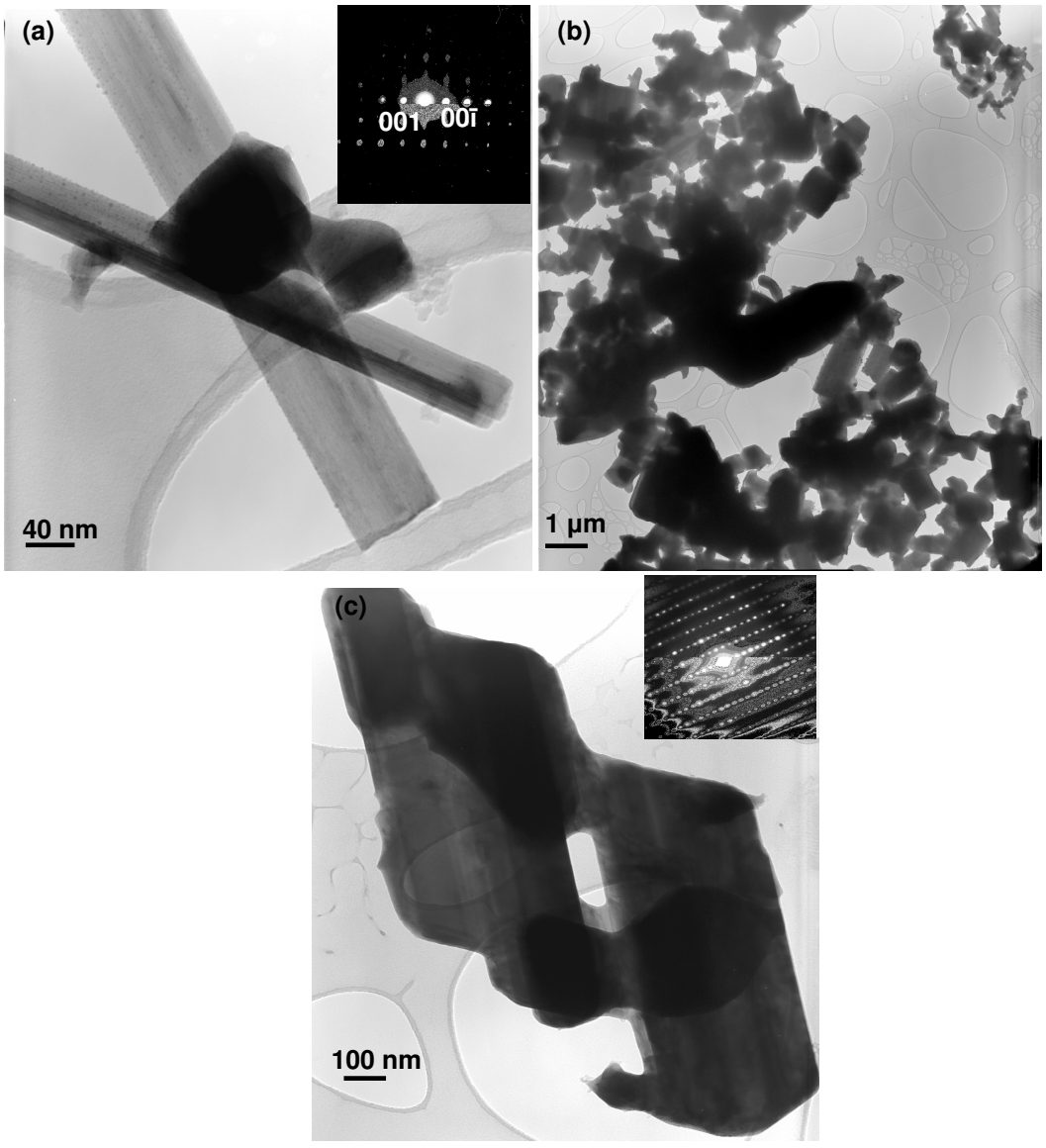

Figure A1.6: TEM images of (a) Nanowires (b) Nanoparticles and (c) Nanosheets

The nanowires are about 100-150nm in diameter/width and measure several micrometers in length. As can be observed from the selected area diffraction (SAD) pattern (Figure A1.6a inset), the main spots can be indexed to the (001) family of planes of the h-WO_3 crystal structure, thus indicating that the nanowires grow along the [001] direction. Also the absence of extra spots in the SAD pattern indicates that the nanowires are single crystals. Figure A1.6(b) corresponds to the nanoparticles that are seen aggregated in to clusters in typical polycrystalline morphology. The individual nanoparticles are too thick to provide a SAD pattern. The nanosheets as depicted in Figure A1.6(c) have a hexagonal morphology and exhibit clear facets. The inset shows the SAD pattern as obtained from the nanosheets. The pattern is indicative of the presence of crystallographic shear planes, which is clear from the presence of extra spots in the diffraction pattern. From earlier literature it is known that the shear planes are not restricted only to the pseudo-cubic crystal structures of WO_3, but they can also be accommodated in the hexagonal lattice without resulting in nonstoichiometry [16].

The schematic of the sol-gel reaction expected to occur when tungsten (V) isopropoxide ($W(^{i}\mathrm{Pr})_5$) comes in contact with moisture is shown below.

$$W(^{i}\mathrm{Pr})_5 + H - OH \rightarrow W(OH)_5 + R - OH$$

The hydrolysis and subsequent condensation in this case occurs by alocoxolation-by removal of water. The isopropoxide functional group is removed as isopropanol which then dries out. The blue color of the precursor on hydrolysis can be explained by the

electron excess on the W^{5+} ion and the electron excess can be accommodated by oxygen vacancies. Though detailed spectroscopic studies on the intermediate precursor are needed, a general mechanism for the formation of hexagonal tungsten trioxide may be devised. The precursor for the hexagonal lattice requires an additive for stabilizing the framework. Previous reports suggest that either a hydrate or hydrogen substituted metal oxide is essential in the formation of hexagonal tungsten oxide to serve as the intermediate step [17-18]. The water molecule in the hydrate or the hydrogen atom in the case of the metal hydrogen oxide serves to stabilize the hexagonal lattice which is otherwise thermodynamically unstable. The substoichiometric isopropoxide precursor on reaction with the moisture in the atmosphere results in the formation of $H_{0.24}WO_3$ that is known to transform to hexagonal WO_3 on oxidation in air. A hydrogen substituted metal oxide is more viable as a precursor in this case as compared to the hydrate. This is because of the fact that the metal alkoxide is sub-stoichiometric and removal of two molecules of water from the $W(OH)_5$ in eq. (1) results in a lone hydrogen atom that can be easily accommodated in the hexagonal framework of WO_3 as shown in Figure A1.7(a) which then transforms to h-WO_3 (Figure A1.7(b)).

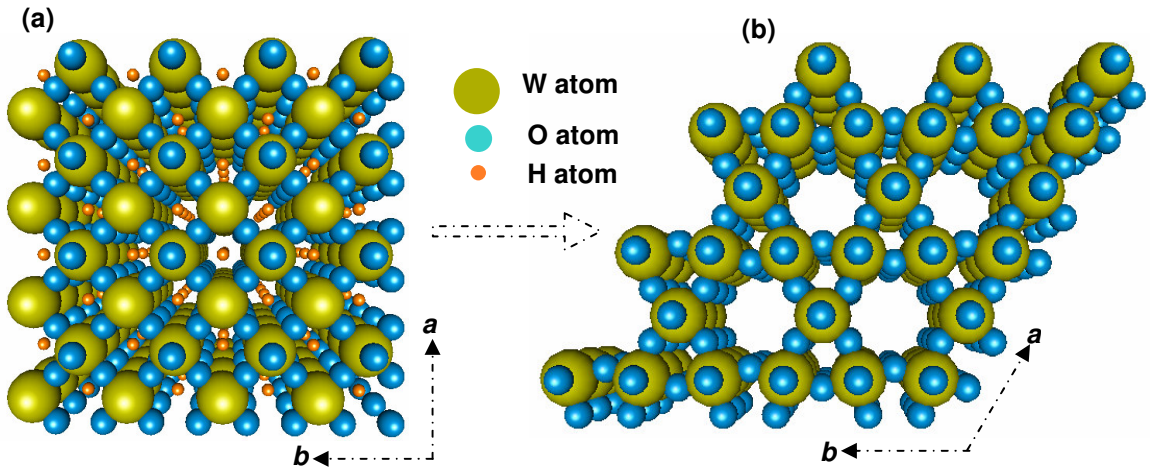

Figure A1.7: (a) Perspective view illustrating $H_{0.24}WO_3$ with the H atoms in the interstitial spaces, precursor to, (b) h-WO_3

There is still not a clear explanation as to what drives the growth of hexagonal tungsten oxide in to three different morphologies in the film. Earlier work on self assembled h-WO_3 nanowire bundles suggests that the presence of a catalyst ion such as a sulfate, on the faces parallel to the c-axis leads to preferential growth along the c-axis [19]. This seed crystal serves as the precursor for the growth of long one dimensional structures. In the absence of the catalyst it was also observed normal aggregates of nanoparticles were obtained. But in this case there is no catalyst ion addition in to the precursor. It is known that for a growth of any single crystal a continuous supply of the precursor phase has to be available and under optimal conditions, the crystal can grow to large lengths. Also polymoprhic transformations are unique in that, if the precursor is amorphous they can grow to abnormally large lengths and in a single crystal configuration. In the case of titania, transformation of anatase to rutile occurs with the

formation of long single crystals of rutile [20]. Similarly, in our earlier work with molybdenum oxide we found that the polymorphic transformation from amorphous to orthorhombic MoO_3 occurs with the formation of long single crystal nanowires [11]. The colloidal precursor solution, which is amorphous to start with, supplies the building blocks for the nanowire growth. Nanosheets and nanoparticles must form where there is no continuous supply of the metal alkoxide precursor.

In conclusion, we report the synthesis of nano h-WO_3 without any catalyst or impurity additions by a simple annealing treatment from a metal alkoxide precursor. The most critical step in the formation of this thermodynamically metastable polymorphic modification is the presence of a sub-stoichiometic precursor that leads to a hydrogen-substituted intermediate lattice, which eventually transforms to h-WO_3. Three specific and unique morphologies are observed in the annealed sample. The nanowires and the nanosheets with their reduced dimensionality provide a high surface area to bulk volume ratio and hence extremely amenable for applications that require high surface areas such as gas sensing, catalysis and power applications. The presence of unique crystallographic features such as the long prism tunnels and unique layered morphology in h-WO_3 is expected to provide the new level of selectivity for discriminative gas sensing and also serve as an intercalation host for rechargeable Li^+ batteries.

References

1. L. Lietti, J.L. Alemany, P. Forzatti, G.Busca, G. Ramis, E. Giamello, F. Bregani, "Reactivity of V_2O_5-WO_3/TiO_2 catalysts in the selective catalytic reduction of nitric oxide by ammonia", *Catal. Today*. **29**, (1996), 143-148.
2. C.G. Granqvist, "Handbook of Inorganic Electrochromic materials"; Elsevier: Amsterdam, (1995).
3. J. Livage, G. Guzman, "Aqueous precursors for electrochromic tungsten oxide hydrates", *Solid State Ionics* **84**, (1996), 205-211.
4. E.P.S Barrett, G.C. Georgiades, P.A. Sermon, "The mechanism of operation of WO_3 based H_2S sensors" *Sens. Actuators B.* **1**, (1990)**,** 116-120.
5. B. Gerand, G. Nowogrocki, J. Guenot, M. Figlarz, "Structural study of a new hexagonal form of tungsten oxide", *J. Solid State Chem.* **29**, (1979), 429-434.
6. R.J.D Tilley, "The crystal chemistry of the higher tungsten oxides", *Int. J. of Refractory Metals & Hard Materials*. **13**, (1995), 93-109.
7. R.C.T. Slade, B.C. West, G.P. Hall, "Chemical and electrochemical mixed alkali metal insertion chemistry of the hexagonal tungsten trioxide framework", *Solid State Ionics* **32-33**, (1989), 154-161.
8. M.S. Whittingham, J.D. Guo, R. Chen, T. Chirayil, G. Janauer, P. Zavalij, "Hydrothermal synthesis of new oxide materials", *Solid State Ionics*, **75**, (1995), 257-268.
9. P.I. Gouma, A.K. Prasad, K.K Iyer, "Selective nanoprobes for 'signaling gases'", *Nanotechnology* **17**, (2006), S48-S53.

10. E. Comini, V. Guidi, C. Malagù, G. Martinelli, Z. Pan., G. Sberveglieri, Z.L. Wang, "Electrical properties of two dimensional tin oxide nanostructres", *J. Phys. Chem. B* **108**, (2004), 1882-1887.
11. P.I. Gouma, K. Kalyanasundaram, A. Bishop, "Electrospun single-crystal MoO_3 nanowires for biochemistry sensing probes", *J. Mater. Res.* **21**, (2006), 2904-2910.
12. W. Han, M. Hibino, T. Kudo, "Synthesis of the hexagonal form of tungsten trioxide from peroxopolytungstate via ammonium paratungstate decahyrate", *Bull. Chem. Soc. Jpn.*, **71**, (1998), 933-937.
13. M. Gillet, R. Delamare, E. Gillet, "Growth of epitaxial tungsten oxide nanorods", *J. Cryst. Growth*, **279**, (2005), 93-99.
14. Y. Wu, Z. Xi, G. Zhang, J. Yu, D. Guo, "Growth of hexagonal tungsten trioxide tubes", *J. Cryst. Growth,* **292**, (2006), 143-148.
15. Z.Gu, H. Li, T. Zhai, W. Yang, Y. Xia, Y. Ma, J. Yao, "Large-scale synthesis of single-crystal hexagonal tungsten trioxide nanowires and electrochemical lithium intercalation in to the nanocrystals", *J. Solid State Chem.*, **180**, (2007), 98-105.
16. H.G. Choi, Y.H. Jung, D.K. Kim, "Solvothermal synthesis of tungsten oxide nanorod/nanowire/nanosheet", *J. Am. Ceram. Soc.*, **88**, (2005), 1684-1686.
17. Cs. Balászi, A.K. Prasad, J. Pfeifer, A.L. Tóth, P.I. Gouma, "Wet Chemical synthesis of nanosize tungsten oxide for sensing applications" Proceedings of the First International Workshop on Semiconductor Nanocrystals

SEMINANO2005, ed. B. Pődör, Zs. Horváth and P. Basa (September 2005, Budapest, Hungary), 79-82.

18. Y.M. Solonin, O.Y. Khyzhun, E.A. Graivoronskaya, "Nonstoichiometric tungsten oxide based on hexagonal WO_3", *Cryst Growth Des*. **1**, (2001), 473-477.
19. Z. Gu, Y. Ma, W. Yang, G. Zhang, J. Yao, "Self-assembly of highly oriented one-dimensional h-WO_3 nanostructures", *Chem. Commun.* **28**, (2005), 3597-3599.
20. P.I. Gouma, M.J. Mills, "Anatase-to-rutile transformation in titania powders", *J. Am. Ceram. Soc.* **84**, (2001), 619-622.